UNIVERSITY OF OKLAHOMA

GRADUATE COLLEGE

Searching for Supersymmetric Particles at the Large Hadron Collider using the ATLAS Detector

A DISSERTATION

SUBMITTED TO THE GRADUATE FACULTY

in partial fulfillment of the requirements for the

Degree of

DOCTOR OF PHILOSOPHY

By

OTHMANE RIFKI
Norman, Oklahoma
2016

Searching for Supersymmetric Particles at the Large Hadron Collider using the ATLAS Detector

A DISSERTATION APPROVED FOR THE
HOMER L. DODGE DEPARTMENT OF PHYSICS AND ASTRONOMY

BY

Dr. Brad Abbott, Chair

Dr. Peter Parker, Outside Member

Dr. Mike Strauss

Dr. Chung Kao

Dr. Eric Abraham

To my loving parents and sister.

Table of Contents

Acknowledgements

I would like to acknowledge...

Abstract

Well now this is my abstract.

Preface

Chapter 1

Introduction

Chapter 2

Theoretical Background

2.1 The Standard Model of Particle Physics

2.2 Supersymmetry

2.3 Phenomenology at the LHC

Chapter 3

Experimental Apparatus

3.1 The Large Hadron Collider

3.2 A Toroidal LHC Apparatus (ATLAS)

3.3 ATLAS Detector

3.4 ATLAS Trigger and Data Acquisition System

3.5 Event Simulation

3.6 Reconstruction and Identification Techniques

Chapter 4

The Region of Interest Builder

4.1 Overview

4.2 VMEbus based RoIB

4.3 PC based RoIB

4.4 Prototype Tests

4.5 Online Performance in Run-2

4.6 Conclusion

Chapter 5

Analysis Strategy

5.1 Overview

5.2 Phenomenology (Benchmarking Models)

Final states with two same-sign leptons or three leptons and multiple jets can probe a variety of supersymmetric models represented by decays of heavy superpartners involving massive gauge bosons, sleptons or top quarks. The decays of the superpartners can lead to many experimental signatures that may lead to different lepton, jet, and b-tagged jet multiplicities. To exploit this wide range of possible signatures, the analysis uses six R-parity-conserving SUSY scenarios featuring gluino, bottom squark or top squark pair production. These scenarios were used as benchmarks to identify regions of the phase space where the analysis can bring particularly useful complementarity to other SUSY searches, and subsequently define signal regions with a particular focus on these regions. In this section, the scenarios considered are presetend with details about the assumed superpartner masses and decay modes. Exclusion limits obtained prior to the work of the author will also be shown to highlight the improvement in reach that this analysis brings.

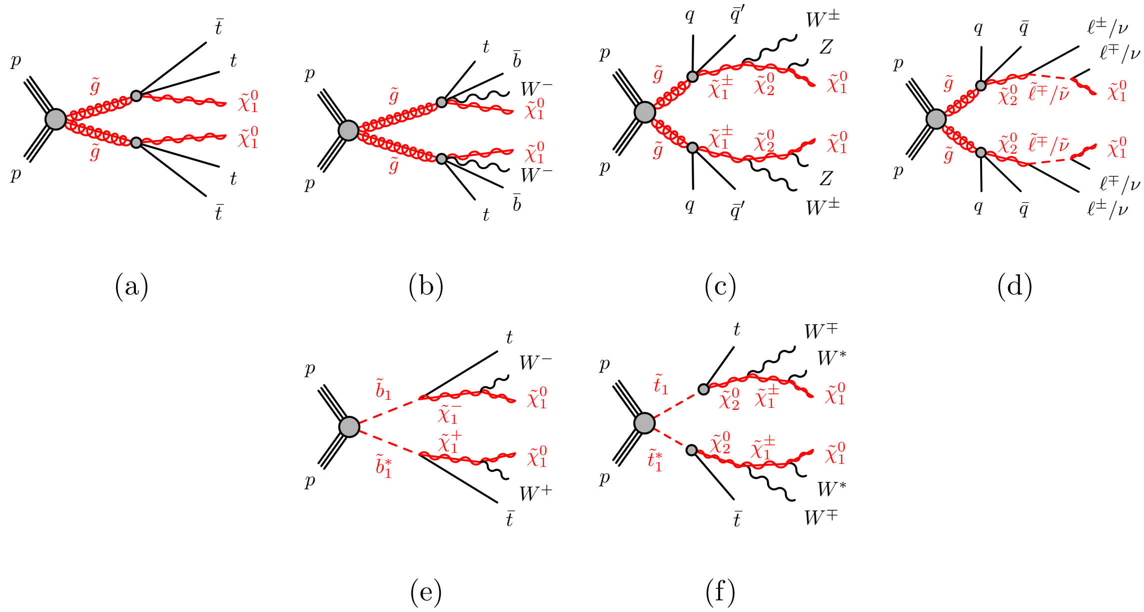

Figure 5.1: SUSY processes featuring gluino ((a), (b), (c), (d)) or third-generation squark ((e), (f)) pair production studied in this analysis. In Figure 5.1d, $\tilde{\ell} \equiv \tilde{e}, \tilde{\mu}, \tilde{\tau}$ and $\tilde{\nu} \equiv \tilde{\nu}_e, \tilde{\nu}_\mu, \tilde{\nu}_\tau$. In Figure 5.1f, the W^* labels indicate largely off-shell W bosons – the mass difference between $\tilde{\chi}_1^\pm$ and $\tilde{\chi}_1^0$ is around 1 GeV.

Gluino pair production with slepton-mediated two-step decay $\tilde{g} \rightarrow q\bar{q}\ell\bar{\ell}\tilde{\chi}_1^0$

This scenario (Fig. 5.1d) features gluino pair-production with two-step decays via neutralinos $\tilde{\chi}_2^0$ and sleptons, $\tilde{g} \rightarrow q\bar{q}'\tilde{\chi}_2^0 \rightarrow q\bar{q}'(\tilde{\ell}\ell/\tilde{\nu}\nu) \rightarrow q\bar{q}'(\ell\ell/\nu\nu)\tilde{\chi}_1^0$. The decays are mediated by generic heavy squarks, therefore the b-jet multiplicity in this scenario is low. The final state is made of charged leptons, four additional jets and invisible particles (neutrinos and neutralinos). The average jet multiplicity per event is the smallest among the four scenarios; another characteristic is the large fraction of events with several leptons, unlike the other scenarios that have

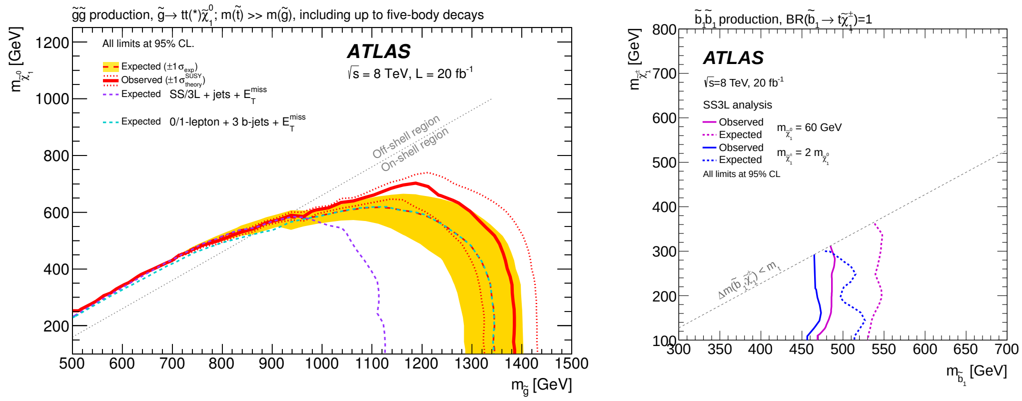

(a) (b)

Figure 5.2: Exclusion limits on the gluino-stop offshell [1] (left) and direct sbottom [2] (right) scenarios set by ATLAS with the 2012 dataset prior to the author's work.

a rather low acceptance due to the branching ratios of $W \to \ell\nu$ or $Z \to \ell\ell$. The exclusion limits obtained in run-1 (Fig. 5.3b) show again that the SS/3L+jets final state is very competitive to probe those models. This scenario is used as as benchmark to define the signal regions with ≥ 3 leptons and no b-jet.

The signal grid is built with variable gluino and $\tilde{\chi}_1^0$ masses; the $\tilde{\chi}_2^0$ mass is chosen half-way between the gluino and LSP masses, and the sleptons masses are also set equal and half-way between the $\tilde{\chi}_2^0$ and LSP masses. The $\tilde{\chi}_2^0$ may decay to any of the six "left-handed" sleptons ($\tilde{\ell}$, $\tilde{\nu}$) with equal probability. "Right-handed" sleptons are assumed heavy and do not participate to the decay.

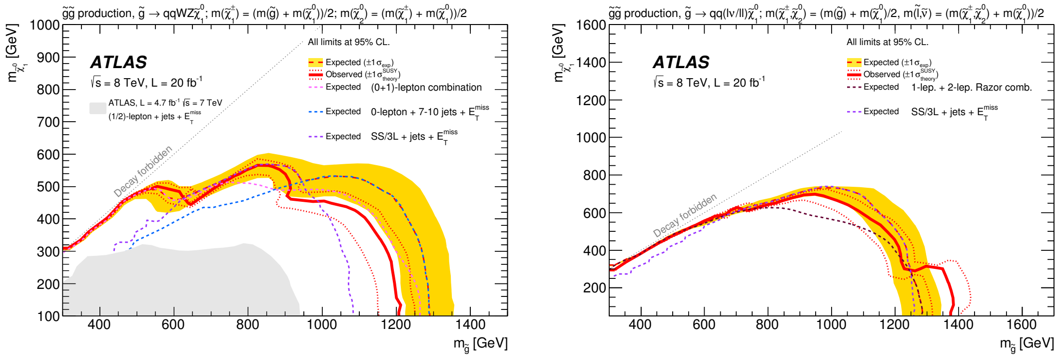

(a) (b)

Figure 5.3: Exclusion limits on scenarios featuring gluino pair production followed by two-step decays via heavy gauge bosons or sleptons, set by ATLAS with the 2012 dataset prior to the author's work [1].

Gluino pair production with gaugino-mediated two-step decay $\tilde{g} \rightarrow q\bar{q}'WZ\tilde{\chi}_1^0$

This scenario (Fig. 5.1c) features gluino pair-production with two-step decays via gauginos and W and Z bosons, $\tilde{g} \rightarrow q\bar{q}'\tilde{\chi}_1^\pm \rightarrow q\bar{q}'W\tilde{\chi}_2^0 \rightarrow q\bar{q}'WZ\tilde{\chi}_1^0$, mediated by generic heavy squarks of the first and second generations. The final state is made of two W and two Z bosons (possibly offshell), four additional jets and invisible particles (neutrinos and neutralinos). This generally leads to events with large jet multiplicities and a fair branching ratio for dileptonic final states. The exclusion limits obtained in run-1 indeed illustrate the competitiveness of the SS/3L+jets search (Fig. 5.3a) particularly the heavy-$\tilde{\chi}_1^0$ region of the phase space. This scenario is used as as benchmark to define the signal regions with many jets but none tagged as a b-jet.

The signal grid is built with variable gluino and $\tilde{\chi}_1^0$ masses, and the $\tilde{\chi}_1^\pm$ and $\tilde{\chi}_2^0$ masses are set such that the former lies half-way between the gluino and $\tilde{\chi}_1^0$ masses, and the latter half-way between $\tilde{\chi}_1^\pm$ and $\tilde{\chi}_1^0$ masses.

Sbottom pair production with one-step decay $\tilde{b}_1 \to t\tilde{\chi}_1^\pm$

In this scenario (Fig. 5.1e), bottom squarks are rather light and assumed to decay in a top quark and a chargino $\tilde{\chi}_1^\pm$, with a subsequent $\tilde{\chi}_1^\pm \to W^\pm\tilde{\chi}_1^0$ decay, providing complementarity to the mainstream search [3] which focuses on the channel $\tilde{b}_1 \to b\tilde{\chi}_1^0$. The final state resulting from the production of a $\tilde{b}_1\tilde{b}_1^*$ pair contains two top quarks, two W bosons and two neutralinos. While this final state may lead to various experimental signatures, the model was considered in Run-1 [1] only by the same-sign leptons and jets search, leading to the exclusion limits presented in Fig. 5.2. Signal events typically contain one or two b-tagged jets, therefore this scenario is used as benchmark to define the signal regions with ≥ 1 b-jet.

The model adopts a fixed chargino-neutralino mass difference of 100 GeV, therefore always allowing on-shell W bosons in the $\tilde{\chi}_1^\pm \to W\tilde{\chi}_1^0$ decay [1] Only pair production of the lightest sbottom is considered, followed by an exclusive decay in the aforementioned channel.

[1] A different chargino mass assumption is adopted in the current work compared to the Run-1 paper [1]. Fig. 5.2 is shown for illustration only. The reduced chargino-neutralino mass gap in the current analysis allows to study signal scenarios with heavy neutralinos, which were not considered previously.

Gluino pair production with stop-mediated decay $\tilde{g} \rightarrow t\bar{t}\tilde{\chi}_1^0$

In this scenario inspired by naturalness arguments, gluinos are coupling preferentially to stops which are lighter than the other squarks. Gluinos are however considered lighter than stops, and decay directly into a $t\bar{t}\tilde{\chi}_1^0$ triplet via a virtual stop (Fig. 5.1a). The pair production of gluinos leads to a final state containing four top quarks and two neutralinos. This characteristic final state is accessible through various experimental signatures, which is why this model is commonly used as a benchmark to compare analyses sensitivities. The searches performed with Run-1 data [1], summarized in Fig. 5.2a, showed that the same-sign leptons final state is competitive only at large neutralino mass. This region of the phase space is consequently given a particular attention in the choice of signal regions described further on. For instance, the region of phase-space with $\Delta m(\tilde{g}, \tilde{\chi}_1^0) < 2m_t$, where gluinos decay via one or two offshell top quarks, is only accessible for this analysis. In the signal samples referenced in this document, the mass of the lightest stop is fixed to 10 TeV and is mostly a $\widetilde{t}_R$ state. Only gluino pair production is considered, followed by an exclusive decay in the aforementioned channel. Signal events typically contain many b-tagged jets, therefore this scenario is used as benchmark to define the signal regions with ≥ 2 b-jets.

$\tilde{t}_1\tilde{t}_1^*$ with "three-same-sign leptons" signature

Inspired by Ref. [4], a simplified model featuring a stop pair-production with two-step decays via a neutralino $\tilde{\chi}_2^0$ and a chargino $\tilde{\chi}_1^{\pm}$ is added in this version of the analysis, according to the decay illustrated on Fig. 5.1f:

$\tilde{t}_1 \to t\tilde{\chi}_2^0 \to t\tilde{\chi}_1^{\pm}W^{\mp} \to tW^{\pm}W^{\mp}\tilde{\chi}_1^0$.

This simplified model is a well-motivated representation of a pMSSM model. The lightest stop ($\tilde{t}_1$) is right-handed and $\tilde{\chi}_2^0$ is bino-like which leads to a large branching ratio in the decay $\tilde{t}_1 \to t\tilde{\chi}_2^0$. Furthermore, the decay $\tilde{\chi}_2^0 \to \tilde{\chi}_1^{\pm}W^{\mp}$ is also enhanced since $\tilde{\chi}_1^{\pm}$ is wino-like, as long as $\tilde{\chi}_1^{\pm}$ and $\tilde{\chi}_1^0$ are nearly mass degenerate and $m_{\tilde{\chi}_2^0} - m_{\tilde{\chi}_1^0} < m_H = 125$ GeV to suppress the decay $\tilde{\chi}_2^0 \to \tilde{\chi}_1^0 + H$ (the decay $\tilde{\chi}_2^0 \to \tilde{\chi}_1^0 + Z$ is suppressed). By respecting these conditions and evading the bottom squark limit shown in Fig. 5.2b, we consider a one-dimensional grid with a $\tilde{t}_1$ mass varying between 550 GeV and 800 GeV with a 50 GeV gap[2], a two body decay to an on-shell top quark and a $\tilde{\chi}_2^0$ which has a 100 GeV mass difference from $\tilde{\chi}_1^0$. The mass difference between the $\tilde{\chi}_1^{\pm}$ and $\tilde{\chi}_1^0$ is taken to be 500 MeV which is not excluded by the disappearing track analysis. In fact, this mass gap could easily be increased by introducing a small amount of higgsino mixing [5].

While the stop pair production is similar to the sbottom pair production in terms of kinematics, the stop pair production offers a unique topology that leads to three leptons of the same electric charge. This final state benefits from an extreme reduction of the SM background while maintaining a good signal acceptance which helps loosen the kinematic cuts to access a more compressed SUSY phase space. As a result, this scenario is complementary to the search for bottom squarks.

[2]Only the points at $\tilde{t}_1$ mass of 550 GeV are available at the moment.

Non-Universal Higgs Models

In references [6, 7, 8], theorists studied a complete two-extra-parameter non-universal Higgs model (NUHM2) that can have low fine tuning (natural) and predicts final state signatures that allow large background rejection while retaining high signal efficiency. The NUHM2 model allows the soft SUSY breaking masses of the Higgs multiplets, m_{H_u} and m_{H_d}, to be different from matter scalar masses (m_0) at the grand unification scale. The NUHM2 model is expected to form the effective theory for energies lower than m_{GUT} resulting from SU(5) or general SU(10) grand unified theories. The scalar mass m_0, the soft SUSY breaking gaugino mass $m_{1/2}$, the pseudoscalar Higgs boson mass m_A, the trilinear SUSY breaking parameter A_0, the weak scale ratio of Higgs field vacuum expectation values $\tan\beta$, and the superpotential Higgs mass μ are the free parameters. Both $m_{1/2}$ and μ are varied while the other parameters are fixed to $m_0 = 5$ TeV, $A_0 = -1.6m_0$, $\tan\beta = 15$, $m_A = 1$ TeV, and sign(μ)>0. These parameter choices lead directly to a Higgs mass of 125 GeV in accord with experiment. In this "radiatively-driven natural" SUSY approach, the higgsino is required to have mass below 200-300 GeV, the stop to have a mass below ∼3 TeV, and the gluino below ∼4 TeV. The model mainly involves gluino pair production with gluinos decaying predominantly to $t\bar{t}\tilde{\chi}_1^0$ and $tb\tilde{\chi}_1^{\pm}$, giving rise to final states with two same-sign leptons and $E_{\mathrm{T}}^{\mathrm{miss}}$. Table 5.1 shows the branching ratios of the dominant gluino decay modes for $m_{1/2} = 400$ GeV. Simulated NUHM2 signal samples with mass ($m_{1/2}$) values from 300-800 GeV and $\mu = 150$ GeV were generated where the

Decay	BR	Decay	BR
$t\bar{t}\chi_1^0$	0.13	$tb\chi_1^\pm$	0.45
$t\bar{t}\chi_2^0$	0.21	$tb\chi_2^\pm$	0.04
$t\bar{t}\chi_3^0$	0.13	-	-
$t\bar{t}\chi_4^0$	0.02	-	-
$t\bar{t}\chi_i^0$	0.49	$tb\chi_i^\pm$	0.49

Table 5.1: The dominant gluino decay modes for $m_{1/2} = 400$ GeV for the NUHM2 model.

gluino mass in this model is approximately $2.5 \times m_{1/2}$.

5.3 Dataset and Simulated Event Samples

5.3.1 Collision Data

The analysis uses pp–collisions data at $\sqrt{s} = 13$ TeV collected by the ATLAS detector during 2015 and 2016 with a peak instantaneous luminosity of $L = 1.4\times\ 10^{34}\ \mathrm{cm}^{-2}\mathrm{s}^{-1}$. The total integrated luminosity considered corresponds to 36.1 fb^{-1} (3.2 fb^{-1} in 2015 and 32.9 fb^{-1} in 2016) recorded after applying beam, detector, and data-quality requirements. The combined luminosity uncertainty for 2015 and 2016 is 3.2%, assuming partially correlated uncertainties in 2015 and 2016. The integrated luminosity was established following the same methodology as that detailed in Ref. [9], from a preliminary calibration of the luminosity scale using a pair of x-y beam separation scans.

5.3.2 Simulated Event Samples

Monte Carlo (MC) simulated event samples are used to model the SUSY signal and SM backgrounds. The irreducible SM backgrounds refer to processes that lead to two same-sign and/or three "prompt" leptons where the prompt leptons are produced directly in the hard-scattering process, or in the subsequent decays of W, Z, H bosons or prompt τ leptons. The reducible backgrounds, mainly arising from $t\bar{t}$ and V+jets production , are estimated either from data or from MC simulation as described in Section 6.

Table 5.2 presents the event generator, parton shower, cross-section normalization, PDF set and the set of tuned parameters for the modelling of the parton shower, hadronization and underlying event. Apart from the MC samples produced by the SHERPA generator, all MC samples used the EVTGEN v1.2.0 program [10] to model the properties of bottom and charm hadron decays.

The MC samples were processed through either a full ATLAS detector simulation [23] based on GEANT4 [24] or a fast simulation using a parameterization of the calorimeter response and GEANT4 for the ID and MS [25], and are reconstructed in the same manner as the data. All simulated samples are generated with a range of minimum-bias interactions using PYTHIA 8 [12] with the MSTW2008LO PDF set [26] and the A2 tune overlaid on the hard-scattering event to account for the multiple pp interactions in the same bunch crossing (in-time pileup) and neighbouring bunch crossing (out-of-time pileup). The distribution of the average

Physics process	Event generator	Parton shower	Cross-section order	Cross-section value (fb)	PDF set	Set of tuned parameters
Signal	aMC@NLO 2.2.3 [11]	Pythia 8.186 [12]	NLO+NLL	See Table 5.4	NNPDF2.3LO [13]	A14 [14]
$t\bar{t}+X$						
$t\bar{t}W$,$t\bar{t}Z/\gamma^*$	aMC@NLO 2.2.2	Pythia 8.186	NLO [15]	600.8, 123.7	NNPDF2.3LO	A14
$t\bar{t}H$	aMC@NLO 2.3.2	Pythia 8.186	NLO [15]	507.1	NNPDF2.3LO	A14
$4t$	aMC@NLO 2.2.2	Pythia 8.186	NLO [11]	9.2	NNPDF2.3LO	A14
Diboson						
ZZ, WZ	Sherpa 2.2.1 [16]	Sherpa 2.2.1	NLO [17]	$1.3 \cdot 10^3$,$4.5 \cdot 10^3$	NNPDF2.3LO	Sherpa default
inc. $W^{\pm}W^{\pm}$	Sherpa 2.1.1	Sherpa 2.1.1	NLO [17]	86	CT10 [18]	Sherpa default
Rare						
$t\bar{t}WW$, $t\bar{t}WZ$	aMC@NLO 2.2.2	Pythia 8.186	NLO [11]	9.9, 0.36	NNPDF2.3LO	A14
tZ, tWZ, $tt\bar{t}$	aMC@NLO 2.2.2	Pythia 8.186	LO	240, 16, 1.6	NNPDF2.3LO	A14
WH, ZH	aMC@NLO 2.2.2	Pythia 8.186	NLO [19]	$1.4 \cdot 10^3$, 868	NNPDF2.3LO	A14
Triboson	Sherpa 2.1.1	Sherpa 2.1.1	NLO [17]	14.9	CT10	Sherpa default
Irreducible (Incl.)						
W+Jets	Powheg-Box	Pythia 8.186	NNLO	2.0 $\cdot 10^7$	CT10	AZNLO[20]
Z+Jets	Powheg-Box	Pythia 8.186	NNLO	1.9 $\cdot 10^7$	CT10	AZNLO[20]
$t\bar{t}$	Powheg-Box	Pythia 6.428	NNLO+NNLL [21]	8.3 $\cdot 10^5$	CT10	PERUGIA2012 (P2012) [22]

Table 5.2: Simulated signal and background event samples: the corresponding event generator, parton shower, cross-section normalization, PDF set and set of tuned parameters are shown for each sample. Because of their very small contribution to the signal-region background estimate, $t\bar{t}WW$, $t\bar{t}WZ$, tZ, tWZ, $tt\bar{t}$, WH, ZH and triboson are summed and labelled "rare" in the following.

number of interactions per bunch crossing $\langle\mu\rangle$ ranges from 0.5 to 39.5, with a profile set as an estimate of the combined 2015+2016 data $\langle\mu\rangle$ profile. With larger luminosity collected during this year and the μ distribution in data being closer to that in the MC profile, the simulated samples are reweighted to reproduce the observed distribution of the average number of collisions per bunch crossing $\langle\mu\rangle$.

Background process simulation

The two dominant irreducible background processes are $t\bar{t}V$ (with V being a W or Z/γ^* boson) and diboson production with final states of four charged leptons ℓ,[3] three charged leptons and one neutrino, or two same-sign charged leptons and two neutrinos.

The production of a $t\bar{t}V$ constitutes the main source of background with prompt same-sign leptons for event selections including b-jets. Simulated events for these processes were generated at NLO with aMC@NLO v2.2.2 [11] interfaced to Pythia 8, with up to two (ttW) or one ($ttZ^{(*)}$) extra parton included in the matrix elements [27]. The samples are normalised to the inclusive process NLO cross-section using appropriate k-factors [11].

The production of multiple W, Z bosons decaying leptonically constitutes the main source of background with prompt same-sign leptons for event selections vetoing b-jets. Diboson processes with four charged leptons, three charged leptons and one neutrino, or two charged leptons and two neutrinos were simulated at NLO using the Sherpa 2.2.1 generator [16], as described in detail in Ref. [17]. The main samples simulate $qq \to VV \to$ leptons production including the doubly resonant WZ and ZZ processes, non-resonant contributions as well as Higgs-mediated contributions, and their interferences; up to three extra partons were included (at LO) in the matrix elements. Simulated events for the $W^\pm W^\pm jj$ process (including non-resonant contributions) were produced at LO with up

[3] All lepton flavours are included here and τ leptons subsequently decay leptonically or hadronically.

to one extra parton, separately for QCD-induced ($\mathcal{O}(\alpha_{\text{em}}^4)$) and VBS-induced ($\mathcal{O}(\alpha_{\text{em}}^6)$) production – the interferences being neglected. Additional samples for VBS-induced $qq \to 3\ell\nu jj$ and $qq \to 4\ell$ and loop-induced $gg \to WZ^{(*)}/ZZ^{(*)}$ processes were also produced with the same configuration. The samples generated at NLO are directly normalized to the cross-sections provided by the generator.

Production of a Higgs boson in association with a $t\bar{t}$ pair is simulated using aMC@NLO [11] (in MadGraph v2.2.2) interfaced to Herwig 2.7.1 [28]. The UEEE5 underlying-event tune is used together with the CTEQ6L1 [29] (matrix element) and CT10 [18] (parton shower) PDF sets. Simulated samples of SM Higgs boson production in association with a W or Z boson are produced with Pythia 8.186, using the A14 tune and the NNPDF23LO PDF set. Events are normalised with cross-sections calculated at NLO [19].

MadGraph v2.2.2 [30] is used to simulate the $t\bar{t}WW$, tZ, $t\bar{t}t\bar{t}$ and $t\bar{t}t$ processes, and the generator cross-section is used for tZ and $t\bar{t}t$. MadGraph interfaced to Pythia 8 is used to generate $t\bar{t}WZ$ processes, and appropriate k-factors are taken from [11]. aMC@NLO interfaced to Pythia 8 is used for the generation of the tWZ process, with an alternative sample generated with aMC@NLO interfaced to Herwig used to evaluate the parton shower uncertainty. Fully leptonic triboson processes (WWW, WWZ, WZZ and ZZZ) with up to six charged leptons are simulated using Sherpa v2.1.1 and described in Ref. [17]. The 4ℓ and $2\ell + 2\nu$ processes are calculated at next-to-leading order (NLO) for up to one additional parton; final states with two and three additional partons are calculated at leading order (LO). The $WWZ \to 4\ell + 2\nu$ or $2\ell + 4\nu$ processes are calculated at LO with up to two additional partons. The $WWW/WZZ \to 3\ell + 3\nu$, $WZZ \to 5\ell + 1\nu$, $ZZZ \to 6\ell + 0\nu$, $4\ell + 2\nu$ or $2\ell + 4\nu$ processes are calculated is calculated at NLO with up to two extra partons at LO. The CT10 [18] parton distribution function (PDF) set is used for all SHERPA samples in conjunction with a dedicated tuning of the parton shower parameters developed by the SHERPA authors. The generator cross-sections (at NLO for most of the processes) are used when normalising these backgrounds.

Double parton scattering (DPS) occurs when two partons interact simultaneously in a proton-proton collision leading to two hard scattering processes overlapping in a detector event. Accordingly, two single W production processes can lead to a $W^{\pm} + W^{\pm}$ final state via DPS. This background is expected to have a negligeable contribution to signal regions with high jet multiplicities. To estimate a conservative upper bound on cross-section for WW events which might arise from DPS, a standard ansatz is adopted: in this, for a collision in which a hard process (X) occurs, the probability that an additional (distinguishable) process (Y) occurs is parametrized as:

$$\sigma_{XY}^{DPS} = \sigma_X \sigma_Y / \sigma_{eff} \tag{5.1}$$

where σ_X is the production cross section of the hard process X and σ_{eff} (effective area parameter) parameterizes the double-parton interaction part of the production cross section for the composite system (X+Y). A value of σ_{eff} is 10-20 mb is assumed in this study (as obtained from 7 TeV measurements, and with no observed dependence on $\sqrt{s}$), and it is independent on the processes involved. For the case of $W^\pm + W^\pm$ production:

$$\sigma^{DPS}_{W^\pm W^\pm} = \frac{\sigma_{W^+}\sigma_{W^+} + \sigma_{W^-}\sigma_{W^-} + 2\sigma_{W^+}\sigma_{W^-}}{\sigma_{eff}} \simeq 0.19 - 0.38 \text{ pb.} \tag{5.2}$$

After the application of the SR criteria, only 4 raw MC events in the DPS $WW \to \ell\nu\ell\nu$ remain. Table 5.3 shows the expected contribution in the SRs where some MC event survives all the cuts. The ranges quoted in the tables reflect the range in the predicted $\sigma^{DPS}_{W^\pm W^\pm}$ cross-section above, as well as the combinatorics for scaling the jet multiplicity[4]. Due to the large uncertainties involved in these estimates, some of them difficult to quantify (such as the modelling of DPS by Pythia at LO), the contribution from this background is not included in the final SR background estimates. Note that the estimated DPS contribution is typically much smaller than the uncertainty on the total background for the SRs.

Table 5.3: Number of raw MC events and its equivalent for 36.1 fb^{-1}with and without the correction as a function of the jet multiplicity. Only the SRs where at least one MC event passes all the cuts are shown.

SR	Raw MC evts	Without N_{jet} correction	With N_{jet} correction
Rpc2L0bS	2	0.016-0.033	0.09-0.38
Rpc2L0bH	1	0.006-0.012	0.05-0.17

Table 5.4: Signal cross-sections [pb] and related uncertainties [%] for scenarios featuring $\tilde{g}\tilde{g}$ (top table) or $\tilde{b}_1\tilde{b}_1^*$ (bottom table) production, as a function of the pair-produced superpartner mass, reproduced from Ref. [31].

Gluino mass (GeV)	500	550	600	650	700
Cross section (pb)	$27.4 \pm 14\%$	$15.6 \pm 14\%$	$9.20 \pm 14\%$	$5.60 \pm 14\%$	$3.53 \pm 14\%$
750	800	850	900	950	1000
$2.27 \pm 14\%$	$1.49 \pm 15\%$	$0.996 \pm 15\%$	$0.677 \pm 16\%$	$0.466 \pm 16\%$	$0.325 \pm 17\%$
1050	1100	1150	1200	1250	1300
$0.229 \pm 17\%$	$0.163 \pm 18\%$	$0.118 \pm 18\%$	$0.0856 \pm 18\%$	$0.0627 \pm 19\%$	$0.0461 \pm 20\%$
1350	1400	1450	1500	1550	1600
$0.0340 \pm 20\%$	$0.0253 \pm 21\%$	$0.0189 \pm 22\%$	$0.0142 \pm 23\%$	$0.0107 \pm 23\%$	$0.00810 \pm 24\%$

Sbottom mass (GeV)	400	450	500	550
Cross section (pb)	$1.84 \pm 14\%$	$0.948 \pm 13\%$	$0.518 \pm 13\%$	$0.296 \pm 13\%$
600	650	700	750	800
$0.175 \pm 13\%$	$0.107 \pm 13\%$	$0.0670 \pm 13\%$	$0.0431 \pm 14\%$	$0.0283 \pm 14\%$

Signal cross-sections and simulations

The signal processes are generated from leading order (LO) matrix elements with up to two extra partons (only one for the grid featuring slepton-mediated gluino decays), using the MADGRAPH v5.2.2.3 generator [11] interfaced to PYTHIA 8.186 [12] with the *ATLAS 14* tune [14] for the modelling of the SUSY decay chain, parton showering, hadronisation and the description of the underlying event. Parton luminosities are provided by the NNPDF23LO [32] set of parton

[4] For instance, a DPS event with 6 jets can be due to the overlap of two events with 6+0 jets, or 5+1, 4+2 or 3+3 jets. All possible combinations are considered and the range quoted in the table shows the combinations leading to the smallest and largest correction factors.

distribution functions. Jet-parton matching is realized following the CKKW-L prescription [33], with a matching scale set to one quarter of the pair-produced superpartner mass.

The signal samples are normalised to the next-to-next-to-leading order cross-section from Ref. [31] including the resummation of soft gluon emission at next-to-next-to-leading-logarithmic accuracy (NLO+NLL), as detailed in Ref. [34]; some of these cross-sections are shown for illustration in Table 5.4.

Cross-section uncertainties are also taken from Ref. [31] as well, and include contributions from varied normalization and factorization scales, as well as PDF uncertainties. They typically vary between 15 and 25%. Uncertainties on the signal acceptance are not considered since these are generally smaller than the uncertainties on the inclusive production cross-section.

5.4 Event Selection

5.4.1 Pre-selection and event cleaning

A sample of two same-sign or three leptons is selected applying the following criteria:

- **Jet Cleaning**: Events are required to pass a set of cleaning requirements. An event is rejected if any pre-selected jets ($|\eta| < 4.9$, after jet-electron overlap removal) fails the jet quality criteria. The cleaning requirements are intended to remove events where significant energy was deposited in the calorimeters due to instrumental effects such as cosmic rays, beam-induced (non-collision) particles, and noise. Around 0.5% of data events are lost after applying this cut.

- **Primary Vertex**: Events are required to have a reconstructed vertex [35] with at least two associated tracks with $p_{\mathrm{T}} > 400$ MeV. The vertex with the largest Σp_{T}^2 of the associated tracks is chosen as the primary vertex of the event. This cut is found to be 100% efficient.

- **Bad Muon Veto**: Events containing at least one pre-selected muon satisfying $\sigma(q/p)/|q/p| > 0.2$ before the overlap removal are rejected. Around 0.1% of data events are removed by this cut.

- **Cosmic Muon Veto**: Events containing a cosmic muon candidate are rejected. Cosmic muon candidates are looked for among pre-selected muons, if they fail the requirements $|z_0| < 1.0$ mm and $|d_0| < 0.2$ mm, where the longitudinal and transverse impact paramaters z_0 and d_0 are calculated with respect to the primary vertex. Up to 6% of data events are lost at this cleaning cut.

- **At least two leptons**: Events are required to contain at least two signal leptons with $p_{\mathrm{T}} > 20$GeV for the two leading leptons. If the event contains a third signal lepton with $p_{\mathrm{T}} > 10$GeV the event is regarded as a three-lepton event, otherwise as a two-lepton event. The data sample obtained is then divided into three channels depending on the flavor of the two leptons forming a same-sign pair (ee, $\mu\mu$, $e\mu$). If more than one same-sign pairs can be built, the one involving the leading lepton will be considered for the channel selection.

- **Same-sign**: if the event has exactly two leptons, then these two leptons have to be of identical electric charge ("same-sign").

The following event variables are also used in the definition of the signal and validation regions in the analysis:

- The inclusive effective mass m_{eff} defined as the scalar sum of all the signal leptons p_{T}, all signal jets p_{T} and $E_{\mathrm{T}}^{\mathrm{miss}}$.

5.4.2 Trigger strategy

Events are selected using a combination of dilepton and $E_{\mathrm{T}}^{\mathrm{miss}}$ triggers, the latter being used only for events with $E_{\mathrm{T}}^{\mathrm{miss}} > 250$GeV. Since the trigger thresholds have been raised between 2015 and 2016 due to the continuous increase of the instantaneous luminosity, the dilepton triggers used for:

- 2015 data: logical `or` of a trigger with two electrons of 12 GeV, with an electron of 17 GeVand a muon of 14 GeV, with two muons of 18 GeVand 8 GeV.

- 2016 data: logical `or` of a trigger with two electrons of 17 GeV, with an electron of 17 GeVand a muon of 14 GeV, with two muons of 22 GeVand 8 GeV.

The $E_{\mathrm{T}}^{\mathrm{miss}}$ trigger was also raised from 70GeVto a 100 GeVand 110 GeV. The trigger-level requirements on $E_{\mathrm{T}}^{\mathrm{miss}}$ and the leading and subleading lepton p_{T} are looser than those applied offline to ensure that trigger efficiencies are constant in the relevant phase space.

Trigger matching

For events exclusively selected via one or several of the dilepton triggers, we require a matching between the online and offline leptons with $p_{\mathrm{T}} > 20$GeV. with the exception of the dimuon trigger for which muons with $p_{\mathrm{T}} > 10$GeV are also considered. In addition, for the dimuon trigger in the 2016 configuration, the p_{T} requirement of the leading matched muon is raised to 23 GeVto remain on the trigger efficiency plateau.

Trigger scale factors

The simulated events are corrected for any potential differences in the trigger efficiency between data and MC simulation. Assuming uncorrelation between the $E_{\mathrm{T}}^{\mathrm{miss}}$ and dilepton triggers, trigger scale factors are applied to MC events which were not selected by the $E_{\mathrm{T}}^{\mathrm{miss}}$ trigger. These scale factors are computed for each event, considering the combination of fired triggers, the number and flavours of the leptons,

5.4.3 Object definition

This section presents the definitions of the objects used in the analysis: jets, electrons, muons and $E_{\mathrm{T}}^{\mathrm{miss}}$ (the taus are not considered).

Jets

Jets are reconstructed using the anti-k_t jet algorithm [36] with the distance parameter R set to 0.4 and a three dimensional input of topological energy clusters in the calorimeter [37]. The jets are kept only if they have $p_{\mathrm{T}} > 20$ GeV and lie within $|\eta| < 2.8$. To mitigate the effects of pileup, the pile-up contribution is subtracted from the expected average energy contribution according to the jet area [38, 39]. In order to reduce the effects of pile-up, a significant fraction of the tracks in jets with $p_{\mathrm{T}} < 60$GeV and $|\eta| < 2.4$ must originate from the primary vertex, as defined by the jet vertex tagger (JVT) [40]. The jet calibration follows the prescription in Ref. [39].

Jets containing b-hadrons (commonly referred to as b-tagging) is performed with the MV2c10 algorithm, a multivariate discriminant making use of track impact parameters and reconstructed secondary vertices [41, 42]. The 70% efficiency operating point was chosen which corresponds to the average efficiency for tagging b-jets in simulated $t\bar{t}$ events. This efficiency working point was favored by optimisation studies performed in simulated signal and background samples. The rejection factors for light-quark/gluon jets, c-quark jets and hadronically decaying τ leptons in simulated $t\bar{t}$ events are approximately 380, 12 and 54, respectively [42, 43]. Jets with $|\eta| < 2.5$ which satisfy the b-tagging and JVT requirements are identified as b-jets. Correction factors and uncertainties determined from data for the b-tagging efficiencies and mis-tag rates are applied to the simulated samples [42].

For the data-driven background estimations, two categories of electrons and muons are used: "candidate" and "signal" with the latter being a subset of the "candidate" leptons satisfying tighter selection criteria.

Electrons

Electron candidates are reconstructed from energy depositions in the electromagnetic calorimeter amd required to be matched to an inner detector track, to have $p_{\mathrm{T}} > 10$GeV and $|\eta| < 2.47$, and to pass the "Loose" likelihood-based electron identification requirement [44]. Electrons in the transition region between the barrel and endcap electromagnetic calorimeters ($1.37 < |\eta| < 1.52$) are rejected to reduce the contribution from fake/non-prompt electrons. The transverse impact parameter d_0 with respect to the reconstructed primary vertex must satisfy $|d_0/\sigma(d_0)| < 5$. This last requirement helps reduce the contribution from charge mis-identification.

Signal electrons are additionally required to pass the "Medium" likelihood-based identification requirement [44]. Only signal electrons with $|\eta| < 2.0$ are considered, to reduce the level of charge-flip background. In addition, signal electrons that are likely to be reconstructed with an incorrect charge assignment are rejected using a few electron cluster and track properties: the track impact parameter, the track curvature significance, the cluster width and the quality of the matching between the cluster and its associated track, both in terms of energy and position. These variables, as well as the electron p_{T} and η, are combined into a single classifier using a boosted decision tree (BDT). A selection requirement on the BDT output is chosen such as to achieve a rejection factor between 7 and 8 for electrons with a wrong charge assignment while selecting properly measured electrons with an efficiency of 97% (in $Z \to ee$ MC).

A multiplicative event weight is applied for each signal electron in MC to the overall event weight in order to correct for differences in efficiency between data and MC.

Muons

Muons candidates are reconstructed from muon spectrometer tracks matched to the inner detector tracks in the region $|\eta| < 2.5$. Muon candidates must pass the "Medium" identification requirements [45] and have $p_{\mathrm{T}} > 10\mathrm{GeV}$ and $|\eta| < 2.4$. Signal muons are required to pass $|d_0|/\sigma(d_0) < 3$ and $|z_0 \cdot \sin(\theta)| < 0.5mm$.

A multiplicative event weight is applied for each selected muon in MC to the overall event weight in order to correct for differences in efficiency between data and MC.

Overlap removal

According to the above definitions, one single final state object may fall in more than one category, being therefore effectively double-counted. For example, one isolated electron is typically reconstructed both as an electron and as a jet. A procedure to remove overlaps between final state objects was therefore put in place, and applied on pre-selected objects. Any jet within a distance $\Delta R_y \equiv \sqrt{(\Delta y)^2 + (\Delta\phi)^2} = 0.2$ of a lepton candidate is discarded, unless the jet is

b-tagged,[5] in which case the lepton is discarded since it probably originated from a semileptonic b-hadron decay. Any remaining lepton within $\Delta R_y \equiv \min\{0.4, 0.1 + 9.6\text{GeV}/p_{\mathrm{T}}(\ell)\}$ of a jet is discarded. In the case of muons, the muon is retained and the jet is discarded if the jet has fewer than three associated tracks. This reduces inefficiencies for high-energy muons undergoing significant energy loss in the calorimeter.

Missing transverse energy

The missing transverse energy ($E_{\mathrm{T}}^{\mathrm{miss}}$) is computed as a negative vector sum of the transverse momenta of all identified candidate objects (electrons, photons [46], muons and jets) and an additional soft term. The soft term is constructed from all tracks associated with the primary vertex but not with any physics object. In this way, the $E_{\mathrm{T}}^{\mathrm{miss}}$ is adjusted for the best calibration of the jets and the other identified physics objects listed above, while maintaining approximate pile-up independence in the soft term [47, 48].

5.5 Signal Regions

In order to maximize the sensitivity to the signal models of Figure 5.1, 13 non-exclusive signal regions are defined in Table 5.6. The SRs are named in the form $RPCN\mathrm{L}M\mathrm{b}X$, where N indicates the number of leptons required, M the number of b-jets required, and X indicates the severity of the $E_{\mathrm{T}}^{\mathrm{miss}}$ or m_{eff} requirements (Soft, Medium or Hard). All signal regions allow any number of additional leptons

[5] In this case the b-tagging operating point corresponding to an efficiency of 85% is used.

in addition to a $e^{\pm}e^{\pm}$, $e^{\pm}\mu^{\pm}$ or $\mu^{\pm}\mu^{\pm}$ pair. Signal regions with 3 leptons can be either any charge combination or all three with the same charge (Rpc3LSS1b). For each lepton/b-jet multiplicity, two signal regions are defined targeting either compressed spectra or large mass splittings.

The optimization of the definitions of signal regions relied on a brute-force scan of several discriminating variables in a loose classification of events in terms of number of b-jets and/or leptons in the final state, each being associated to the signal scenario favouring this final state. The other main discriminant variables (e.g number of jets above a certain p_{T} threshold, m_{eff}, $E_{\mathrm{T}}^{\mathrm{miss}}$, $E_{\mathrm{T}}^{\mathrm{miss}}/m_{\mathrm{eff}}$ ratio) were then allowed to vary, to determine for each point of the parameter space the best configuration. The figure of merit used to rank configurations is the discovery significance (Z_0) defined in Eq. 5.3 which represents a a statistical test based on a ratio of two Poisson means [49]:

$$Z_0 = \sqrt{2\left((s+b)\ln\left(1+\frac{s}{b}\right)-s\right)} \tag{5.3}$$

where s and b represent the expected number of signal and background events[6]. A realistic systematic uncertainty of $\Delta b = 30\%$ on the expected background yield was included in the statistical test by replacing b with $b + \Delta b$ in Eq. 5.3. To preserve the discovery potential, only configurations leading to at least two signal events were considered for a given signal point. The total number of background events should not be smaller than 1; to model in a more realistic way the effect of non-prompt and fake leptons and electron charge mis-identification

[6] Note that Eq.5.3 simplifies to the commonly used figure of merit $\frac{s}{\sqrt{b}} + \mathcal{O}\left(\frac{s}{b}\right)$ if $\frac{s}{b} \ll 1$.

backgrounds, which are determined from data in the analysis, the MC predictions for those processes in $t\bar{t}$ and Z+jets MC were scaled using the factors obtained from the MC template method (Section 6.3.1), as shown in Table 5.5. Note that different corrections are applied depending on the showering (Pythia or Sherpa) used for each sample, and for the fake and non-prompt leptons originated from heavy-flavour (HF) and light-flavour (LF).

Table 5.5: Scaling factors applied to the electron charge-flip and non-prompt/fake lepton background in the SR optimization procedure.

	Charge mis-id	HF e	HF μ	LF e	LF μ
Pythia	0.96 $\pm$ 0.08	1.80 $\pm$ 0.45	2.10 $\pm$ 0.58	1.55 $\pm$ 0.14	0.74 $\pm$ 0.81
Sherpa	1.02 $\pm$ 0.09	2.72 $\pm$ 0.57	1.81 $\pm$ 0.75	1.16 $\pm$ 0.18	1.84 $\pm$ 1.16

Since the signal regions defined out of the scanning procedure may not be mutually exclusive, the results expressed in terms of exclusion limits will be obtained by using for each signal point the SR giving the best expected sensitivity. For the latter, only the signal regions that were defined aiming for that particular signal model are considered, though.

Figures 5.4 and 5.5 show the performance of the SRs in the four RPC benchmark models with top quarks considered. The discovery significance for each signal point is shown, together with the contours corresponding to a 3σ discovery sensitivity, 1.64σ discovery sensitivity and 95% confidence level limits.

Dedicated new SRs have been optimized for the gluino pair production with

(a) Rpc2L1bS

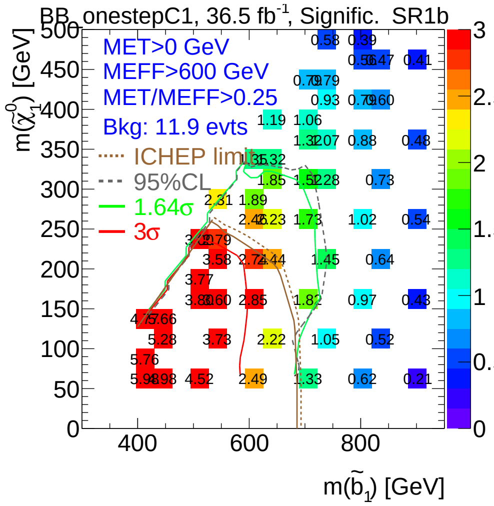

(b) Rpc2L1bH

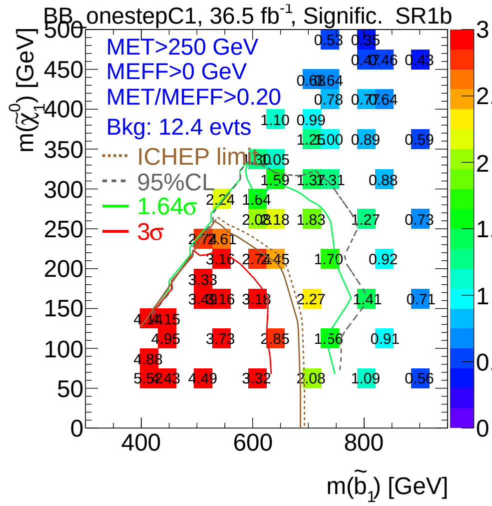

(c) Rpc2L2bS

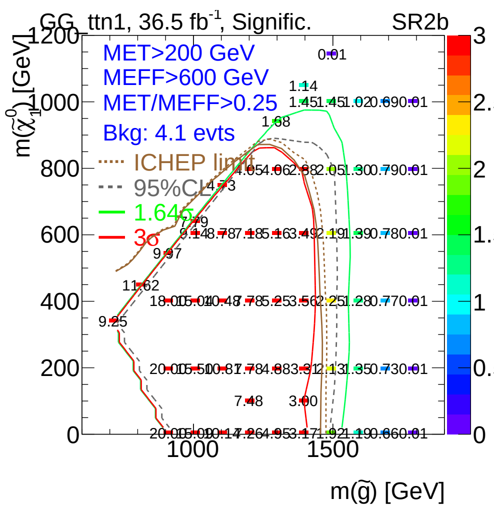

(d) Rpc2L2bH

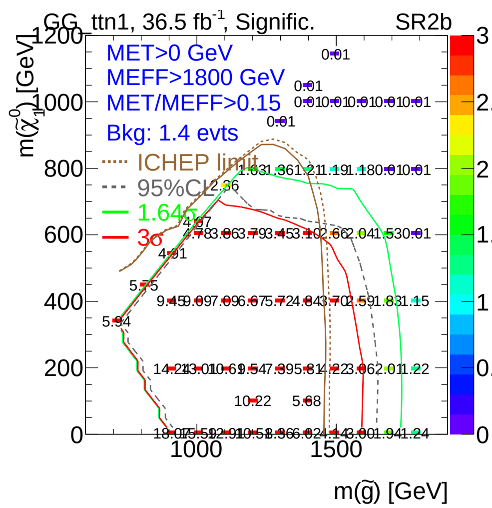

Figure 5.4: Discovery significance for the SRs with b-jets defined in Table 5.6 for 36.5 fb^{-1}: Rpc2L1bS and Rpc2L1bH in the $\tilde{b}_1\tilde{b}_1^* \to t\bar{t}\tilde{\chi}_1^+\tilde{\chi}_1^-$ grid (top), Rpc2L2bS and Rpc2L2bH in the $\tilde{g}\tilde{g} \to t\bar{t}t\bar{t}\tilde{\chi}_1^0\tilde{\chi}_1^0$ grid (bottom). The 95% CL, 1.64σ, and 3σ discovery contours from the proposed signal regions are shown in grey, green, and red, respectively.

(a) Rpc3L0bS

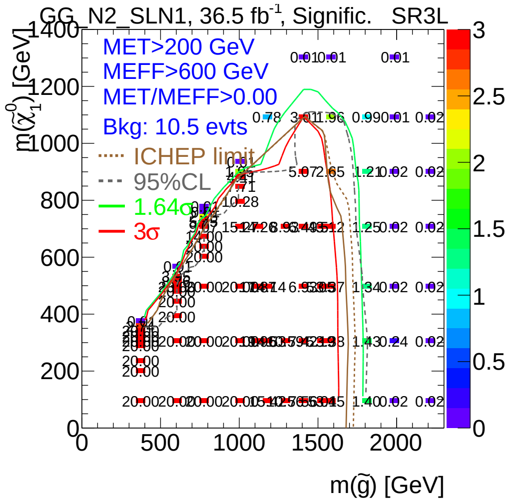

(b) Rpc3L0bH

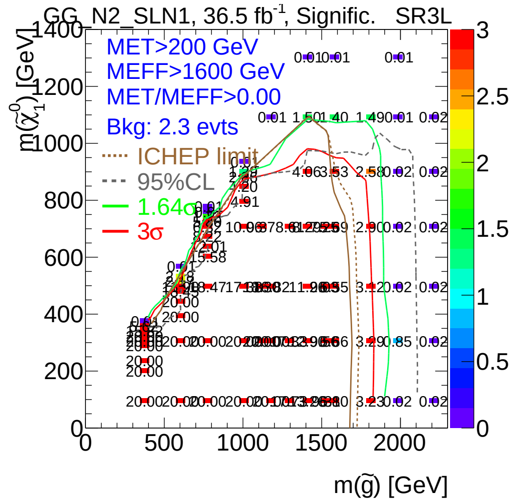

(c) Rpc2L0bS

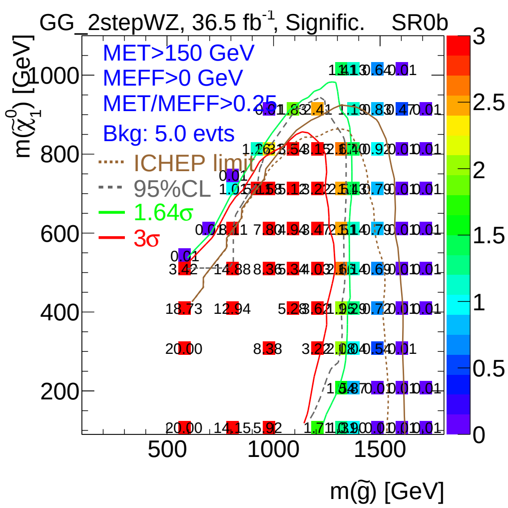

(d) Rpc2L0bH

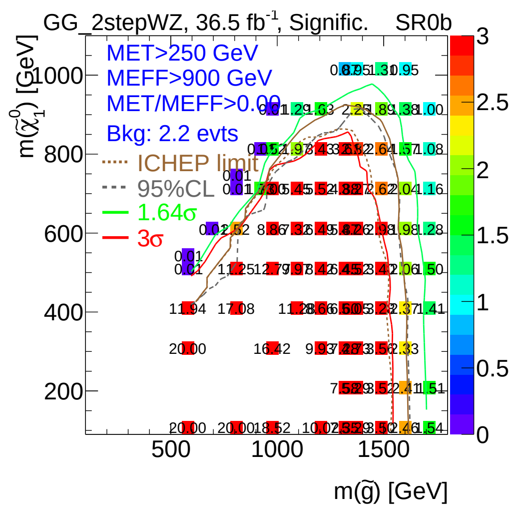

Figure 5.5: Discovery significance for the SRs without b-jets defined in Table 5.6 for 36.5 fb^{-1}: Rpc2L0bS and Rpc2L0bH in the $\tilde{g}\tilde{g}$ with $\tilde{g} \to q\bar{q}'WZ\tilde{\chi}_1^0$ grid (top) and Rpc3L0bS and Rpc3L0bH in the $\tilde{g}\tilde{g}$ with $\tilde{g} \to q\bar{q}(\ell\ell/\ell\nu)\tilde{\chi}_1^0$ grid (bottom). The 95% CL, 1.64σ, and 3σ discovery contours from the proposed signal regions are shown in grey, green, and red, respectively.

Signal region	$N_{\text{leptons}}^{\text{signal}}$	$N_{b\text{-jets}}$	N_{jets}	$p_{\text{T}}^{\text{jet}}$ [GeV]	$E_{\text{T}}^{\text{miss}}$ [GeV]	m_{eff} [GeV]	$E_{\text{T}}^{\text{miss}}/m_{\text{eff}}$	Other	Targeted Signal
Rpc2L2bS	≥ 2SS	≥ 2	≥ 6	> 25	> 200	> 600	> 0.25	–	Fig. 5.1a
Rpc2L2bH	≥ 2SS	≥ 2	≥ 6	> 25	–	> 1800	> 0.15	–	Fig. 5.1a, NUHM2
Rpc2Lsoft1b	≥ 2SS	≥ 1	≥ 6	> 25	> 100	–	> 0.3	20,10 $< p_{\text{T}}^{\ell_1}, p_{\text{T}}^{\ell_2} <$ 100 GeV	Fig. 5.1b
Rpc2Lsoft2b	≥ 2SS	≥ 2	≥ 6	> 25	> 200	> 600	> 0.25	20,10 $< p_{\text{T}}^{\ell_1}, p_{\text{T}}^{\ell_2} <$ 100 GeV	Fig. 5.1b
Rpc2L0bS	≥ 2SS	$= 0$	≥ 6	> 25	> 150	–	> 0.25	–	Fig. 5.1c
Rpc2L0bH	≥ 2SS	$= 0$	≥ 6	> 40	> 250	> 900	–	–	Fig. 5.1c
Rpc3L0bS	≥ 3	$= 0$	≥ 4	> 40	> 200	> 600	–	–	Fig. 5.1d
Rpc3L0bH	≥ 3	$= 0$	≥ 4	> 40	> 200	> 1600	–	–	Fig. 5.1d
Rpc3L1bS	≥ 3	≥ 1	≥ 4	> 40	> 200	> 600	–	–	Other
Rpc3L1bH	≥ 3	≥ 1	≥ 4	> 40	> 200	> 1600	–	–	Other
Rpc2L1bS	≥ 2SS	≥ 1	≥ 6	> 25	> 150	> 600	> 0.25	–	Fig. 5.1e
Rpc2L1bH	≥ 2SS	≥ 1	≥ 6	> 25	> 250	–	> 0.2	–	Fig. 5.1e
Rpc3LSS1b	$\geq \ell^{\pm}\ell^{\pm}\ell^{\pm}$	≥ 1	–	–	–	–	–	veto 81$< m_{e^{\pm}e^{\pm}} <$101 GeV	Fig. 5.1f

Table 5.6: Summary of the signal region definitions. Unless explicitly stated in the table, at least two signal leptons with $p_{\text{T}} >$20 GeV and same charge (SS) are required in each signal region. Requirements are placed on the number of signal leptons ($N_{\text{leptons}}^{\text{signal}}$), the number of b-jets with $p_{\text{T}} >$ 20GeV ($N_{b\text{-jets}}$), the number of jets (N_{jets}) above a certain p_{T} threshold ($p_{\text{T}}^{\text{jet}}$), $E_{\text{T}}^{\text{miss}}$, m_{eff} and/or $E_{\text{T}}^{\text{miss}}/m_{\text{eff}}$. The last column indicates the targeted signal model. The Rpc3L1b and Rpc3L1bH SRs are not motivated by a particular signal model and can be seen as a natural extension of the Rpc3L0b SRs with the same kinematic selections but requiring at least one b-jet.

stop-mediated decay $\tilde{g} \rightarrow t\bar{t}\tilde{\chi}_1^0$ with off-shell tops.

The $\tilde{g}\tilde{g}$ production with $\tilde{g} \rightarrow t\bar{t}\tilde{\chi}_1^0$ scenario at low LSP masses (where the

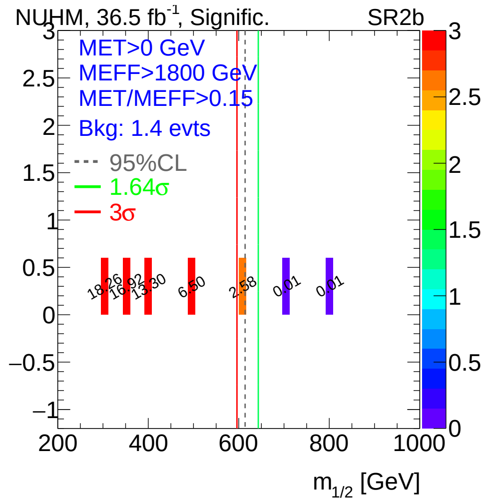

Figure 5.6: Discovery significance for Rpc2L2bH signal region for 36.5 fb^{-1}, NUHM2 model. The 95% CL, 1.64σ, and 3σ discovery contours from the proposed signal regions are shown in grey, green, and red, respectively.

multi-b analysis has a much better sensitivity [50]) is not the only motivation for Rpc2L2bH signal region, but also the NUHM2 model, which features large branching ratios for the $\tilde{g} \to t\bar{t}\tilde{\chi}^0_{1,2,3}$ and $\tilde{g} \to t\bar{b}\tilde{\chi}^{\pm}_{1,2}$ decays. As shown in Figure 5.6, with the Rpc2L2bH signal region $m_{1/2}$ values of 600 GeV can be excluded at 95% CL or observed with a 3σ significance. This SR will be then used for the first interpretation in this model.

In addition, the SS/3L analysis has the unique potential to explore the region of phase space at high LSP masses with a more compressed spectra. This scenario leads to softer decay products, in particular softer b-jets as seen in Figure 5.7, which makes the multi-b analysis less sensitive. For this reason, two additional signal regions were introduced with at least 1 b-jet (Rpc2Lsoft1b) or 2 b-jets (Rpc2Lsoft2b) defined in Table 5.6. In addition, these signal regions are defined

(a) $m_{\tilde{g}}$-$m_{\tilde{\chi}_1^0}$ mass plane

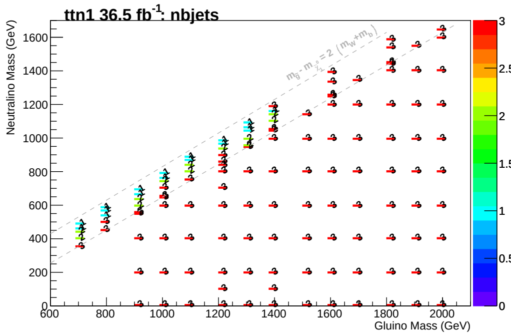

(b) Above the diagonal

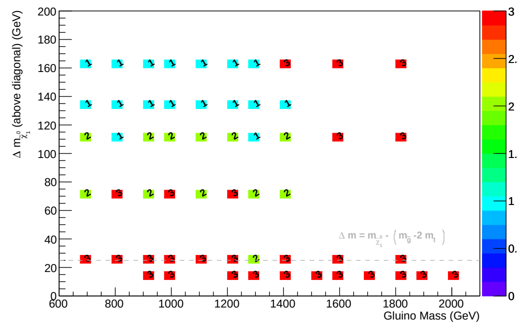

Figure 5.7: Optimal cut on the number of b-jets leading to the best discovery significance.

(a) Without $p_{\mathrm{T}}^{\ell_1}$ uppercut

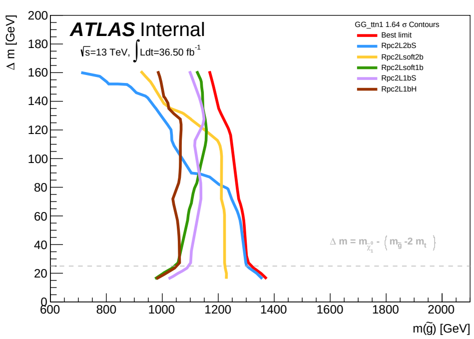

(b) With $p_{\mathrm{T}}^{\ell_1}$ uppercut

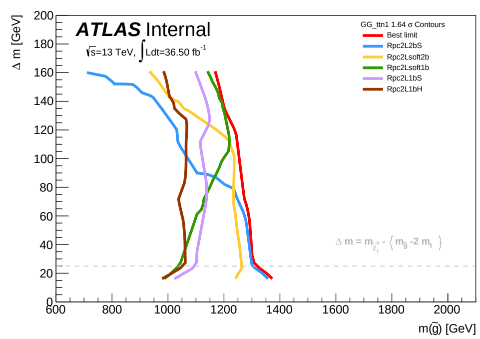

Figure 5.8: Comparison of significance contours at 1.64σ for 36.5 fb^{-1} between Rpc2Lsoft2b and Rpc2Lsoft1b and other signal regions in the off-diagonal region considering the option of an upper cut on the leading lepton p_{T}.

with an upper cut on the leading lepton p_{T}. The sensitivity is degraded if this upper cut is removed as shown in Figure 5.8.

Motivated by the $\tilde{t}$ production with $\tilde{t}_1 \rightarrow \tilde{\chi}_2^0 W$ model in Section 5.2, the signature of three leptons with the same electric charge (3LSS) is explored for the first time. As shown in Figure 5.9, after and inclusive 3LSS selection, the background is dominated by dibosons and Z+jets (with only one real lepton, and the two other leptons with either an electron with charge mis-identified or a fake lepton) both dominantly without b-jets. Once a b-jet requirement is applied, the background is dominated by $t\bar{t}V$, with a clear peak at $m_{\ell\ell} \approx m_Z$ showing that a large fraction of these events are originated from charge mis-identification from events containing $Z \rightarrow ee$. After applying a $81 < m_{e^{\pm}e^{\pm}} < 101$ GeV veto, the background is reduced to only 1.7 events for 36.5 fb^{-1}, almost removing the Z+jets and diboson backgrounds completely. The final background is dominated by $t\bar{t}+H, Z, W$, with ≈60% originating from charge flips and ≈40% from fakes and non-prompt leptons. With these very generic selections (Rpc3LSS1b in Table 5.6), a significance of 3.7σ can be obtained for $m_{\tilde{t}} = 550$ GeV. Figure 5.10 shows some lepton distributions, including the number of electrons, where most of the charge flip background populates the bins with 2 or 3 electrons, although cutting away those bins would also have a large impact on the signal.

Finally, since the SRs defined for the $\tilde{g}\tilde{g}$ production with $\tilde{g} \rightarrow q\bar{q}\ell\bar{\ell}\tilde{\chi}_1^0$ feature a b-jet veto (Rpc3L0bS and Rpc3L0bH), and to avoid leaving uncovered the 3 lepton plus b-jets signature, SRs with the same kinematic cuts as Rpc3L0bS and Rpc3L0bH but with a ≥1 b-jet requirement are also proposed in Table 5.6 as

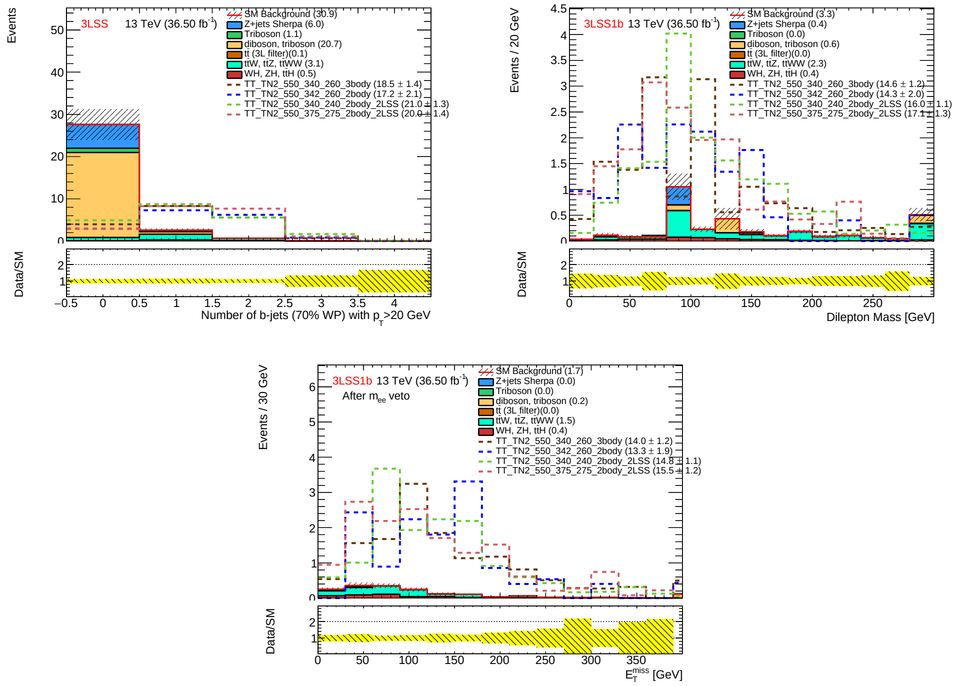

Figure 5.9: b-jet multiplicity after a 3LSS selection (top left), dilepton invariant mass distributions after a 3LSS plus $\geq$1 b-jet selection (top right), and $E_{\mathrm{T}}^{\mathrm{miss}}$ distribution after a 3LSS, $\geq$1 b-jet and $81 < m_{e^{\pm}e^{\pm}} < 101$ GeV veto selection (bottom), all corresponding to 36.5 fb^{-1}. The background distributions are stacked, while the lines show the predictions for four signal points at $\tilde{t}$ mass of 550 GeV.

Rpc3L1bS and Rpc3L1bH.

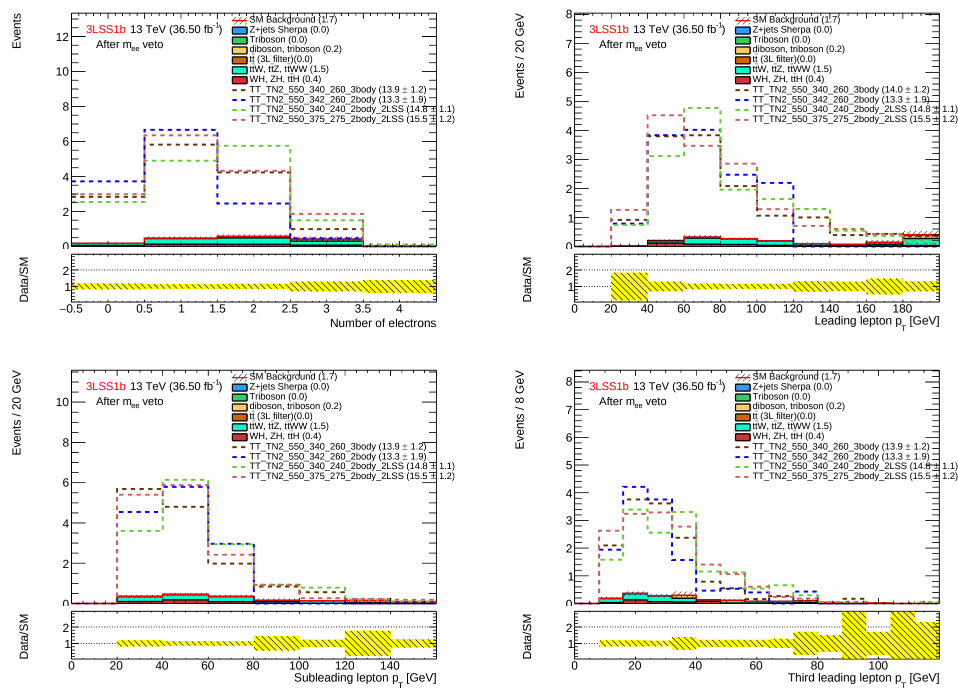

Figure 5.10: Number of electron (top left), and p_{T} of the leading (top right), subleading (bottom left) and third leading lepton (bottom right) after a 3LSS, $\geq$1 b-jet and $81 < m_{e^{\pm}e^{\pm}} < 101$ GeV veto selection (bottom), all corresponding to 36.5 fb^{-1}. The background distributions are stacked, while the lines show the predictions for four signal points at $\tilde{t}$ mass of 550 GeV.

Chapter 6

Data-driven Background Estimation Techniques

6.1 The problem of fakes

The reconstructed objects (leptons, photons, b-jets, etc.) in a collision event are used to perform a wide range of SM measurements or searches for evidence of BSM physics. The assumption is that these objects are 'real' representing the desired particles in the final state used in the analysis. In practice, the reconstructed objects might not be always 'real'. In fact, they may be something completely different that was mistakenly reconstructed as the desired object, called 'fake'. For the purpose of the analysis presented in this thesis, the focus is on 'fake' leptons. To illustrate the problem, a hadronic jet may deposit more energy in the electromagnetic calorimeter than the hadronic calorimeter, or that it leaves a narrow deposit of energy leading the reconstruction alogorithms to mistake this jet for an electron. From the analysis point of view, the 'fake' electron will pass all the selection criteria and will be indistinguishable from a 'real' electron. It is important for the analysis that requires a reconstructed electron to model the fake electron background to get a sound result. This example was given with electrons, but can be generalized to muons as well. In short, any analysis that uses leptons in the final state must account for the 'fake' lepton background. This background can be more or less important depending on the detector, the analysis selection, and the number of leptons required. To estimate this background it is important to first understand what type of processes lead to fake leptons.

6.2 Common processes for faking leptons

The reconstruction of ‘fake‘ leptons can be an instrumental effect related to the inability to identify the object based on its measured properties by the detector. In this case, the reconstructed lepton is not a real lepton and the production process will be different for electrons and muons.

The reconstruction of electrons relies on the observation of well aligned particle hits in the layers of the ID that are consistent with an energy deposition in the EM calorimeter. Photons can mimick this signature since they deposit energy in the EM calorimeter that happens to be alligned with a charged track. A jet for example containing charged and neutral pions can lead to such scenarios. It is possible for the jet to have one charged pion leaving a track similar to that of an electron. The decay of π^0 mesons to photons in this jet can deposit energy in the EM calorimeter leading to the required signature. Another mechanism that can lead to fake electrons is the emission of photons via Brehmstrahlung from high energy muons. The muon track can be mistaken for that of an electron and the photons interact with the EM calorimeter leading to a signature similar to that of electrons. An additional process is that of photon conversions into a e^+e^-.

The reconstruction of muons relies on the observation of tracks from the ID matched to tracks from the muon spectrometer. It is possible for charged hadrons with long lifetime to traverse the calorimeter layers and leave hits in the muon spectrometer. These hits may coincide with other hits from the ID due to the random activity in the event. As a result, a muon can get reconstructed. Another instance may occur when pions or kaons decay in-flight to muons in the muon spectrometer and happen to align with the primary vertex.

The leptons that are used in the physics analyses must be coming from the hard scatter, generally referred to as prompt leptons. There is another case where the reconstructed lepton is a real lepton but is not a lepton coming from the hard interaction, referred to as non-prompt leptons. Non-prompt leptons can be produced from heavy flavor meson decays with a low energy activity around the lepton which allows it to pass isolation requirements. A good example of this type of process is the semi-leptonic decay of top quark pair which contribute to final states with two leptons.

For the rest of the thesis, the fake leptons will be referred to as fake/non-prompt (FNP) leptons. There are several methods used to perform the estimation of FNP lepton backgrounds. A method that the author developed will be described next along with a standard method for estimating this type of backgrounds. The benefit of having two methods for estimating the FNP lepton background is to have enough confidence in the final estimate. The two methods use different assumptions which naturally leads to a more robust estimation of this difficult background. Moreover, the final estimate of the FNP lepton background is taken as a statistical combination of the estimates from the two methods leading to a reduction of the systematic uncertainties on the estimate.

6.3 The Monte Carlo Template Method

6.3.1 Motivation

The processes leading to FNP leptons depend on the selection applied in the analysis. For instance, a selection with same-sign leptons will have contributions from top quark pair production ($t\bar{t}$) or the associated production of a vector boson and jets (W+jets or Z+jets).These processes cannot give two leptons of the same electric charge unless there is a charge mis-measurement (mainly affecting electrons) or that a FNP lepton was produced. It is possible to generate the processes that can contribute to a FNP lepton, such as $t\bar{t}$ or V+jets, with Monte Carlo event generators processed through Geant4 detector simulation of the ATLAS detector. This approach will yield an estimate however it might not be reliable. For instance, the detector simulation itself might not reproduce the true behavior of the interaction of the physics objects with the detector, particularly when looking at rare processes such as the production of FNP leptons. The second limitation is in the generation of enough MC events to probe the region of the phase space targetted by the analysis which affects the statistical uncertainties in the estimates. The latter concern is addressed by ensuring that the simulations for the major backgrounds ($t\bar{t}$ and V+jets) have much higher event count than the corresponding number of events observed in the data sample. In fact, these backgrounds have a large number of simulated events because they are important for many analyses (including SM measurements and BSM searches). The rest of the section will concentrate on addressing the former limitation.

6.3.2 Description of the method

The MC template method relies on the correct modelling of FNP leptons kinematics in MC simulation to extrapolate background predictions from control regions to the signal regions. The method assumes that the kinematic shapes for each source of FNP lepton is correctly modeled in the simulations, and the normalization for each source is extracted in a combined fit to data control regions. The number of normalization factors depend on the number of identified origins of the FNP lepton in the signal regions and the control regions are designed to constrain these factors in regions enriched with FNP leptons from the same origin.

To illustrate the approach, we describe the application of the method in SS/3L analysis later described in this thesis. The processes of interest that may lead to a FNP lepton or a charge flip are $t\bar{t}$ and V+jets. FNP leptons are classified using an algorithm that navigates the generator particle record to determine where the FNP lepton is originating from. The lepton is classified as either an electron or a muon that is prompt from decays of on-shell W and Z bosons, non-prompt from a heavy flavor b decay (HF), or fake from mis-identification of a light flavor jet or a photon (LF). In the case of an electron, we further classify the prompt electrons to prompt electrons with the correct charge or with a charge mis-measurement, commonly named charge flip. In total, five categories referred to as MC templates are construced following the classification illustarted in figure 6.1.

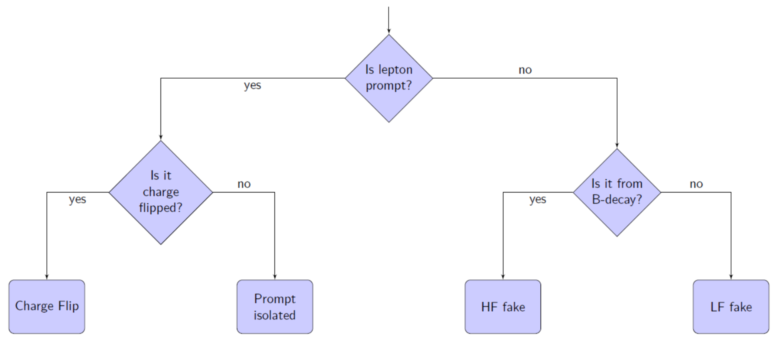

Figure 6.1: Lepton classification.

6.3.3 Correction factors

The FNP estimate relies on kinematic extrapolation using processes expected to contribute via FNP leptons from control regions with low jet multiplicity and $E_{\mathrm{T}}^{\mathrm{miss}}$, to the signal regions that require high jet multiplicity and $E_{\mathrm{T}}^{\mathrm{miss}}$. The control regions are chosen to separate FNP leptons from HF origins and FNP leptons from LF origins. For instance, a control sample characterized by the presence of a b-jet will be enriched in processes with one FNP lepton that is coming from a HF decay, while a sample characterized by the absence of a b-jet will have one FNP lepton from LF decay. The presence of one FNP lepton in the control sample allows the correction of the production rate of these FNP leptons by performing a fit to data.

For example, if a Z$\rightarrow \mu\mu$+LF jet event is reconstructed as a $\mu^+\mu^-e^+$ event, then the electron is fake. Therefore, a correction of LF jet $\rightarrow$ e (Fr(LF$\rightarrow$e)) is applied to the rate of $\mu\mu e$ events. The correction Fr(LF$\rightarrow$e) is constrained by a fit to data in control regions dominated by LF jet $\rightarrow$ e type fakes. Similarly, three other corrections are defined as LF jet $\rightarrow \mu$ (Fr(LF$\rightarrow \mu$)), HF jet $\rightarrow$ e

(Fr(HF→e)), HF jet $\rightarrow \mu$ (Fr(HF$\rightarrow \mu$)). An additional correction is applied to correct the charge flip rate predicted by simulation. For example, a Z$\rightarrow$ e^+e^- event is reconstructed as e^+e^+ or e^-e^-. The simulation takes into account the charge flip rate but it might be off. The charge flip (Cf(e)) correction derived from a data fit is expected to recover this mis-modeling. The charge flip rate only concern electrons as the muon charge flip rate is negligeable.

A likelihood fit is defined as the product of the Poisson probabilities describing the observed events in the binned distributions from the expected number of events rescaled by the five multipliers which are left free to float in the fit. These multipliers are applied to the MC predictions in the signal regions to obtain an estimation of the charge flip and FNP backgrounds.

6.3.4 Control regions

The corrections depend on the simulated sample, the reconstructed final state, and the flavor of the leptons. As a result, care must be taken when designing the control regions used to perform the fit of the FNP leptons and electron charge flip templates. For instance, each template needs to be constrained in a selection that is representative of the processes leading to FNP leptons and charge flip electrons present in the kinematic region targetted by the search for BSM physics.

In the SS/3L analysis discussed in this thesis the control regions are defined with at least two same-sign leptons, $E_{\mathrm{T}}^{\mathrm{miss}} > 40$ GeV, two or more jets. This preselection ensures that the FNP leptons are not from fakes originating from QCD like event topologies. They are further split in regions with or without

b-jets to constrain the HF and LF leptons respectively. In addition, they are also split with different flavours of the same-sign lepton pair ee, eμ, and $\mu\mu$, giving a total of six control regions. Any event entering the signal region is vetoed. The ee channel will constrain the charge flip correction factor, fake leptons from LF decays in the selection without b-jets, and non-prompt decay from HF in the selection with b-jets. The $\mu\mu$ channel will constrain the muon fake rates in the LF and HF decays for the selection without or with b-jets, respectively. The eμ channel will constrain both the electron and muon fakes for events containing both lepton flavors.

The six distributions are chosen for variables that provide the best separation between processes with prompt leptons and processes with FNP leptons and charge flip and are shown before and after the fit in Figures 6.2-6.4 and Figures 6.3-6.5, respectively.

The minimization of the negative log likelihood using the MINUIT package leads to the multipliers shown in Tables 6.1 and 6.2. The tables represent the multipliers obtained from the fit upon using two different parton showers, POWHEG-BOX and SHERPA for the processes that lead to FNP leptons and charge flips. The systematic uncertainty is obtained by varying the generator from POWHEG-BOX to SHERPA and evaluating the impact on the expected background from FNP and charge flip leptons. It is found to be the dominant contribution to the systematic uncertainty of the method (up to 80%). The uncertainties in the multipliers themselves correspond to how much the parameter needs to be varied for a one standard deviation change in the likelihood function. This uncertainty takes into

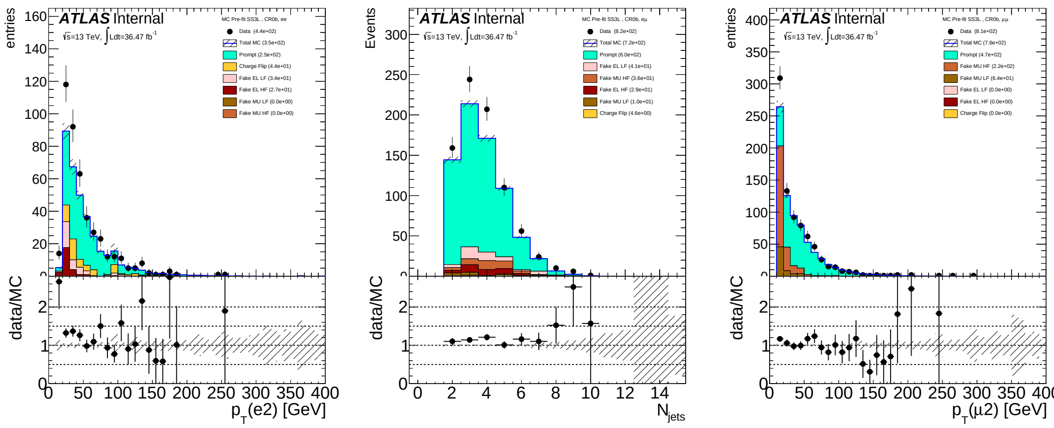

Figure 6.2: Pre-fit distributions for ee channel (left), for $e\mu$ channel (middle), and for $\mu\mu$ channel (right) from CR0b that were used in the fit to extract the FNP lepton and charge flip multipliers. The generator used in these plots is Powheg. The hashed band represents the sum of systematic uncertainties on the predictions.

account the limited number of simulated events and is included as a systematic uncertainty on the expected number of background events.

6.4 Matrix Method

The FNP leptons do not often pass one of the lepton selection criteria but have non-zero impact parameter, and are often not well-isolated. These selection requirements are key ingredients to control the FNP leptons. The number of events with at least one FNP lepton is estimated using two classes of leptons: a real-enriched class of “tight” leptons corresponding to signal leptons and a fake-enriched class of “loose” leptons corresponding to candidate leptons with

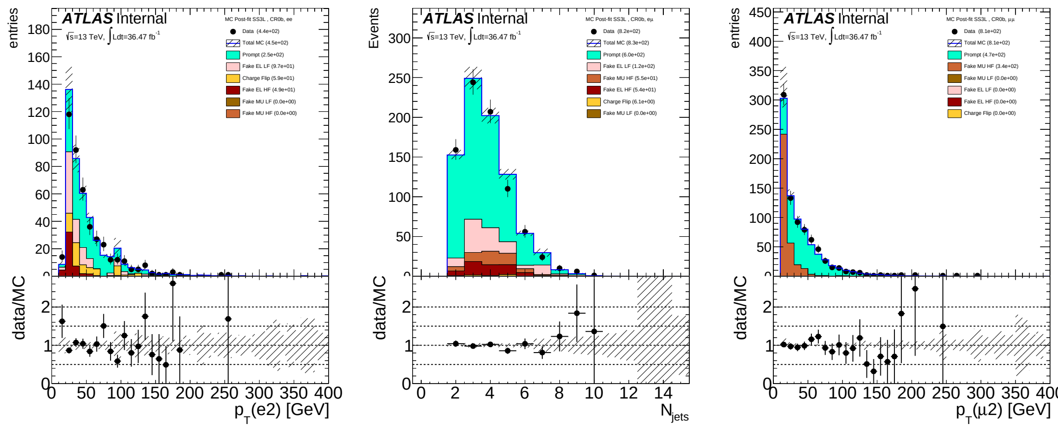

Figure 6.3: Post-fit distributions for ee channel (left), for $e\mu$ channel (middle), and for $\mu\mu$ channel (right) from CR0b that were used in the fit to extract the FNP lepton and charge flip multipliers. The generator used in these plots is Powheg. The hashed band represents the sum of systematic uncertainties on the predictions.

Table 6.1: The FNP and charge flip multipliers obtained after minimizing the likelihood function using Pythia. The uncertainty in the multipliers takes into account the limited statistics of simulated events.

Category	Multiplier	Uncertainty
chFlip	1.49	0.58
HF EL	2.80	0.98
LF EL	2.89	0.88
HF MU	1.59	0.31
LF MU	1.00	1.34

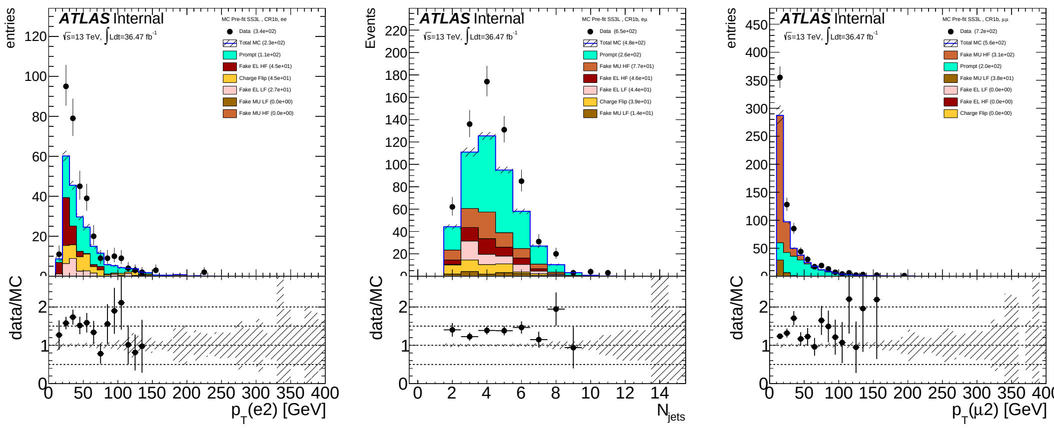

Figure 6.4: Pre-fit distributions for ee channel (left), for $e\mu$ channel (middle), and for $\mu\mu$ channel (right) from CR1b that were used in the fit to extract the FNP lepton and charge flip multipliers. The generator used in these plots is Powheg. The hashed band represents the sum of systematic uncertainties on the predictions.

Table 6.2: The FNP and charge flip multipliers obtained after minimizing the likelihood function using Sherpa. The uncertainty in the multipliers takes into account the limited statistics of simulated events.

Category	Multiplier	Uncertainty
chFlip	1.34	0.58
HF EL	2.40	0.85
LF EL	1.83	1.04
HF MU	1.17	0.16
LF MU	2.40	0.81

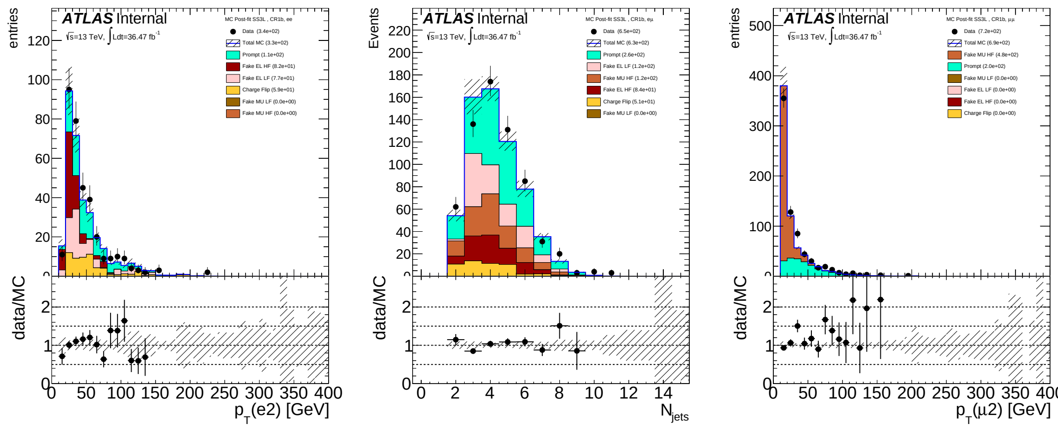

Figure 6.5: Post-fit distributions for ee channel (left), for $e\mu$ channel (middle), and for $\mu\mu$ channel (right) from CR1b that were used in the fit to extract the FNP lepton and charge flip multipliers. The generator used in these plots is Powheg. The hashed band represents the sum of systematic uncertainties on the predictions.

relaxed identification criteria[1]. In the next sections, a description of the simplest form of the matrix method will be given with events containing one object. Then a generalized treatment that can handle events with an arbitrary number of leptons in the final states will be discussed.

6.4.1 Events with one object

Given the probabilities ε/ζ for a real/FNP candidate lepton to satisfy the signal lepton criteria, one can relate the number of events with one candidate lepton passing/failing signal requirements ($n_{\text{pass}}/n_{\text{fail}}$) to the number of events with one real/FNP signal leptons ($n_{\text{real}}/n_{\text{FNP}}$):

[1]Signal leptons are leptons satisfying the signal lepton definition, while the candidate leptons are leptons satisfying some pre-selection cuts and usually passing the overlap removal requirements as discssed in the analysis Section 5.4.3.

$$\begin{pmatrix} n_{\text{pass}} \\ \\ n_{\text{fail}} \end{pmatrix} = \begin{pmatrix} \varepsilon & \zeta \\ \\ 1-\varepsilon & 1-\zeta \end{pmatrix} \begin{pmatrix} n_{\text{real}} \\ \\ n_{\text{FNP}} \end{pmatrix}; \tag{6.1}$$

allowing to determine the unknown number of events n_{FNP} from the observed n_{pass} and n_{fail} given measurements of the probabilities ε/ζ.

The predictive power of the matrix method comes from the fact that the real and FNP leptons have different composition in the two collections of tight and loose objets leading to $\varepsilon \neq \zeta$. In fact, the tight lepton collection will be dominated by real objects while the loose region will be dominated by fake objects. As a result, the inequality $\varepsilon >> \zeta$ will always hold true which guarantees that the martrix in Eq. 6.1 is invertible and gives positive estimates.

The next step is to invert the relation in Eq. 6.1 to obtain

$$\begin{pmatrix} n_{\text{real}} \\ \\ n_{\text{FNP}} \end{pmatrix} = \frac{1}{\varepsilon - \zeta} \begin{pmatrix} \bar{\zeta} & -\zeta \\ \\ -\bar{\varepsilon} & \varepsilon \end{pmatrix} \begin{pmatrix} n_{\text{pass}} \\ \\ n_{\text{fail}} \end{pmatrix}; \tag{6.2}$$

where $\bar{\varepsilon} = 1 - \varepsilon$ and $\bar{\zeta} = 1 - \zeta$. The FNP lepton component is:

$$n_{\text{FNP}} = \frac{1}{\varepsilon - \zeta} \left((\varepsilon - 1)\, n_{\text{pass}} + n_{\text{fail}} \right). \tag{6.3}$$

However, the quantity of interest is the expected FNP lepton background that passes the tight selection criteria: $n_{\text{pass} \,\cap\, \text{FNP}} = \zeta n_{\text{FNP}}$. To obtain this quantity, the identity from Eq. 6.1 is used to get:

$$n_{\text{FNP}} = \frac{\zeta}{\varepsilon - \zeta} \left((\varepsilon - 1)\, n_{\text{pass}} + n_{\text{fail}} \right). \tag{6.4}$$

The linearity of Eq. 6.4 with respect to n_{pass} and n_{fail} allows the method to be applied on an event-by-event, effectively resulting into a weight being assigned to each event. By defining

$$n_{\text{pass}} = \sum_{\text{all events}} \mathbb{1}_{\text{pass}},\ n_{\text{fail}} = \sum_{\text{all events}} \mathbb{1}_{\text{fail}},\ \mathbb{1}_{\text{fail}} = 1 - \mathbb{1}_{\text{pass}},$$

where $\mathbb{1}_{\text{pass(fail)}} = 1$ if the object pass (fail) the tight selection requirement and $\mathbb{1}_{\text{pass(fail)}} = 0$ otherwise. Eq. 6.4 can be written as

$$n_{\text{FNP}} = \sum_{\text{all events}} \{\frac{\zeta}{\varepsilon - \zeta}(\varepsilon - \mathbb{1}_{\text{pass}})\} = \sum_{\text{all events}} \omega$$

where

$$\omega = \frac{\zeta}{\varepsilon - \zeta}(\varepsilon - \mathbb{1}_{\text{pass}}) \tag{6.5}$$

is the weight to be assigned to each event in the case of one FNP lepton in the event. The generalization of this formalism to higher dimensions with multiple objects will be covered next.

6.4.2 Dynamic matrix method

The one lepton case readily generalizes to events with more than one lepton in a formalism that can handle an arbitrary number of leptons in the event. The method should be applied event-by-event, effectively resulting into a weight being assigned to each event. The predicted yield of events with FNP leptons is simply the sum of weights. A general formula will be derived starting from the two objects case then specific examples will be given to illustrate the application of the method.

If two objects are present in the event, the probabilites ε/ζ will depend on the kinematic properties of these objects. Typically the probabilies will vary as a function of p_{T} and $|\eta|$. For this reason, the probabilities will be different and will have an index to identify the object under study: ε_i/ζ_i where $i = 1, 2....$ An identity similar to Eq. 6.1 can be formed for two objects with a change in notation for simplicity:

$$\begin{pmatrix} N_{TT} \\ N_{TL} \\ N_{LT} \\ N_{LL} \end{pmatrix} = \Lambda \times \begin{pmatrix} N_{RR} \\ N_{RF} \\ N_{FR} \\ N_{FF} \end{pmatrix}, \tag{6.6}$$

where $(N_{RR}, N_{RF}, N_{FR}, N_{FF})$ are the number of events with respectively two real, one real plus one FNP (two terms), and two FNP leptons before applying tight cuts, respectively, and $(N_{TT}, N_{TL}, N_{LT}, N_{LL})$ are the observed number of events for which respectively both lepton pass the tight cut, only one of them (two terms), or both fail the tight cut, respectively.

Λ is given by:

$$\Lambda = \begin{pmatrix} \varepsilon_1\varepsilon_2 & \varepsilon_1\zeta_2 & \zeta_1\varepsilon_2 & \zeta_1\zeta_2 \\ \varepsilon_1(1-\varepsilon_2) & \varepsilon_1(1-\zeta_2) & \zeta_1(1-\varepsilon_2) & \zeta_1(1-\zeta_2) \\ (1-\varepsilon_1)\varepsilon_2 & (1-\varepsilon_1)\zeta_2 & (1-\zeta_1)\varepsilon_2 & (1-\zeta_1)\zeta_2 \\ (1-\varepsilon_1)(1-\varepsilon_2) & (1-\varepsilon_1)(1-\zeta_2) & (1-\zeta_1)(1-\varepsilon_2) & (1-\zeta_1)(1-\zeta_2) \end{pmatrix}$$

which can also be written in terms of a Kronecker product in Eq. 6.6 to obtain:

$$\begin{pmatrix} N_{TT} \\ N_{TL} \\ N_{LT} \\ N_{LL} \end{pmatrix} = \begin{pmatrix} \varepsilon_1 & \zeta_1 \\ \bar{\varepsilon}_1 & \bar{\zeta}_1 \end{pmatrix} \bigotimes \begin{pmatrix} \varepsilon_2 & \zeta_2 \\ \bar{\varepsilon}_2 & \bar{\zeta}_2 \end{pmatrix} \begin{pmatrix} N_{RR} \\ N_{RF} \\ N_{FR} \\ N_{FF} \end{pmatrix} \tag{6.7}$$

To make the notation more compact, the set of 4 numbers $(N_{TT}, N_{TL}, N_{LT}, N_{LL})$ can be represented by a rank 2 tensor $\mathcal{T}_{\alpha_1\alpha_2}$ where α_i corresponds to one object that is either tight (T) or loose (L). Similarly the numbers $(N_{RR}, N_{RF}, N_{FR}, N_{FF})$ can be represented by $\mathcal{R}_{\alpha_1\alpha_2}$ where α_i corresponds to one object that is either real (R) or FNP (F). With this convention, the Kronecker product of Eq. 6.7 can be obtained by contracting each index α_i of the tensors $\mathcal{T}$ or $\mathcal{R}$ by the 2×2 matrix ${\phi_i}_{\beta_i}{}^{\alpha_i}$:

$$\mathcal{T}_{\beta_1\beta_2} = {\phi_1}_{\beta_1}{}^{\alpha_1} {\phi_2}_{\beta_2}{}^{\alpha_2} \mathcal{R}_{\alpha_1\alpha_2}, \;\; \phi_i = \begin{pmatrix} \varepsilon_i & \zeta_i \\ \bar{\varepsilon}_i & \bar{\zeta}_i \end{pmatrix} \tag{6.8}$$

Following the same procedure as in the one object case, the matrix inversion of the 4×4 λ matrix is simplified to a matrix inversion of the 2×2 ϕ matrices. The quantity of interest is the FNP lepton background that passes the tight selection criteria as in Eq. 6.4 which can be compactly written in the two objects case as:

$$\mathcal{T}^{\mathrm{FNP}}_{\nu_1\nu_2} = \phi_{\nu_1}{}^{\mu_1} \phi_{\nu_2}{}^{\mu_2} \xi^{\beta_1\beta_2}_{\mu_1\mu_2} {\phi^{-1}}_{\beta_1}{}^{\alpha_1} {\phi^{-1}}_{\beta_2}{}^{\alpha_2} \mathcal{T}_{\alpha_1\alpha_2}. \tag{6.9}$$

The tensor ξ encodes the component of tight and FNP lepton background. In the two objects case, ξ needs to select the total background with at least one fake lepton $N_F = N_{RF} + N_{FR} + N_{FF}$ that are also passing the tight selection criteria corresponding to the region with signal leptons. As a result, ξ takes the form:

$$\xi = \begin{pmatrix} 0 & 0 & 0 & 0 \\ 0 & 1 & 0 & 0 \\ 0 & 0 & 1 & 0 \\ 0 & 0 & 0 & 1 \end{pmatrix}$$

To further illustrate, Eq. 6.9 can be written explicitely in the notation of Eq. 6.6 as:

$$N^{\text{signal}}_{\text{FNP}} = \begin{pmatrix} 0 & \varepsilon_1\zeta_2 & \zeta_1\varepsilon_2 & \zeta_1\zeta_2 \end{pmatrix} \Lambda^{-1} \begin{pmatrix} N_{TT} \\ N_{TL} \\ N_{LT} \\ N_{LL} \end{pmatrix}$$

The generalization of Eq. 6.9 from the two objects case to m number of objects in the final state is straightforward:

$$\mathcal{T}^{\text{FNP}}_{\nu_1\cdots\nu_m} = \phi_{\nu_1}{}^{\mu_1}\cdots\phi_{\nu_m}{}^{\mu_m}\xi^{\beta_1\cdots\beta_m}_{\mu_1\cdots\mu_m}\phi^{-1}{}_{\beta_1}{}^{\alpha_1}\cdots\phi^{-1}{}_{\beta_m}{}^{\alpha_m}\mathcal{T}_{\alpha_1\cdots\alpha_m}. \tag{6.10}$$

The tensor ξ is of the general form

$$\xi^{\beta_1\cdots\beta_m}_{\mu_1\cdots\mu_m} = \delta^{\beta_1}_{\mu_1}\cdots\delta^{\beta_m}_{\mu_m} h\left(\beta_1, \cdots, \beta_m, \nu_1, \cdots, \nu_m\right)$$

where the function h can take values 0 or 1 based on the tight or loose configuration being computed which is encoded in the dependence on the indices ν_i.

The application of the matrix method to multilepton final states comes with two specificities. Firstly, contributions of events with charge-flip electrons would bias a straightforward matrix method estimate (in particular for a final state formed by two leptons with same electric charge). This happens because the candidate-to-signal efficiency for such electrons is typically lower than for real electrons having a correctly-assigned charge. One therefore needs to subtract from n_{pass} and n_{fail} the estimated contributions from charge-flip. This can be performed by including as well events with pairs of opposite-sign candidate leptons in the matrix method estimate, but assigning them an extra weight corresponding to the charge-flip weight. Thanks (again) to the linearity of the matrix method with respect to n_{pass} and n_{fail}, this weight-based procedure is completely equivalent (but more practical) to the aforementioned subtraction.

Secondly, the analytic expression of the matrix method event weight depends on the lepton multiplicity of the final state. This concerns events with three or more candidate leptons: one such event takes part both in the evaluation of the FNP lepton background for a selection with two signal leptons or a selection with three signal leptons, but with different weights[2]. Therefore, for a given event used as input to the matrix method, one should consider all possible leptons combinations, each with its own weight and its own set of kinematic variables. For example, a $e^+e^-\mu^+$ event is comptabilized in the background estimate both as an $e^+\mu^+$ event (with a weight w1) and as an $e^+e^-\mu^+$ event (with a weight $w_2 \neq w1$).

[2]This can appear for inclusive selections: for example an event with two signal leptons may or not contain additional candidate leptons, in a transparent way

6.4.3 Propagation of uncertainties

The two parameters (ε and ζ respectively) can be measured in data, and depend on the flavor and kinematics of the involved leptons. Systematic uncertainties resulting from the measurement of these two parameters, and their extrapolation to the signal regions, can be propagated to uncertainties on the event weight through standard first-order approximations. The different sources of uncertainties should be tracked separately so that correlations of uncertainties across different events can be accounted for correctly. The resulting set of uncertainties on the cumulated event weights can be then added in quadrature to form the systematic uncertainty on the predicted FNP lepton background yield. The corresponding statistical uncertainty can be taken as the RMS of the event weights.

Chapter 7

Background Estimation

7.1 Overview

In this analysis, two types of backgrounds can be distinguished. The first category is the irreducible background from events with two same-sign prompt leptons or at least three prompt leptons and is estimated using the MC simulation samples (Section 7.2). Since diboson and $t\bar{t}V$ events are the main backgrounds in the signal regions, dedicated validation regions with an enhanced contribution from these processes, and small signal contamination, are defined to verify the background predictions from the simulation (Section 7.3). The second category is the reducible background, which includes events containing electrons with mismeasured charge, mainly from the production of top quark pairs, and events containing at least one fake or non-prompt (FNP) lepton. The application of the data-driven methods of Chapter 6 is presented in Section 7.2).

7.2 Irreducible Backgrounds

7.2.1 Validation regions

Dedicated validation regions are defined to verify the estimate of the $W^{\pm}W^{\pm}jj$, the $WZjjjj(j)$, the $t\bar{t}W$ and $t\bar{t}Z$ processes in the signal regions. For a better validation of WZ processes in association with a large jet multiplicity, two VRs are proposed : WZ4j and WZ5j, with 4 and respectively 5 reconstructed jets in

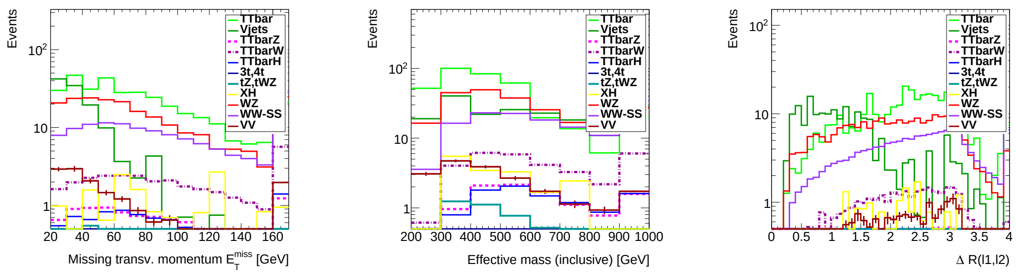

Figure 7.1: $E_{\mathrm{T}}^{\mathrm{miss}}$ (left), m_{eff} (middle) and $\min \Delta R(\ell_1, \ell_2)$ (right) after lepton and jet selection of the $W^{\pm}W^{\pm}$-VR (and no additional requirements). Signal regions are vetoed. All MC samples are normalized to a luminosity of 36.1 fb^{-1}. Last bin includes overflow.

the event. The corresponding selections are summarized in Table 7.1.

$W^{\pm}W^{\pm}$+jets validation region

The $W^{\pm}W^{\pm}$ + jets processes contribute mainly in the signal regions with no b-tagged jet requirement and two same-sign leptons. This validation region, $W^{\pm}W^{\pm}$-VR, has exactly one SS pair (and no additional baseline leptons), zero b-jets and at least two jets with p_{T} above 50 GeV. Additional requirements on $E_{\mathrm{T}}^{\mathrm{miss}}$ and m_{eff} help to decrease the amount of detector background as shown in Figure 7.1 (left and middle). To further improve the purity, the sub-leading lepton p_{T} is increased to 30 GeV, and cuts on minimum angular separation between the leptons and jets, and between the two leptons (Figure 7.1, right) are placed as detailed in Table 7.1. The purity is around 34% with this definition of the validation region. Signal contamination (highly reduced by applying a veto of all SRs) it is found to be at most 5% when looking at $\tilde{g} \to q\bar{q}(\tilde{\ell}\ell/\tilde{\nu}\nu)$ scenarios.

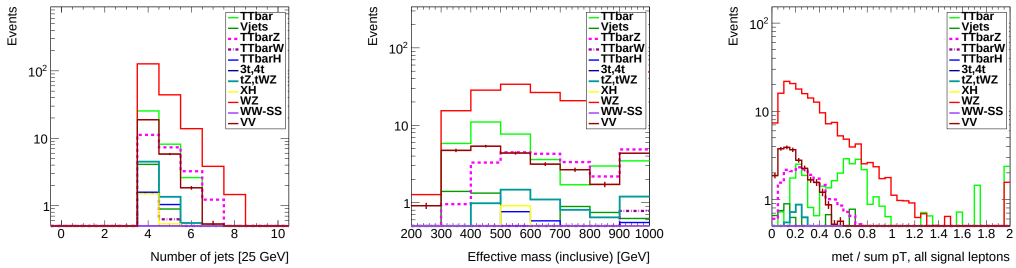

Figure 7.2: Number of jets with $p_{\mathrm{T}} > 25$ GeV(left), m_{eff} (middle) and ratio between the $E_{\mathrm{T}}^{\mathrm{miss}}$ in the event and the sum of all lepton p_{T} (right) after lepton and four jet selection of the WZ-VR (and no additional requirements). Signal regions are vetoed as detailed in Table 7.1. All MC samples are normalized to a luminosity of 36.1 fb^{-1}. Last bin includes overflow.

WZ + jets validation region

Contribution from WZ+jets processes can be significant in regions vetoing the presence of b-jets and requiring three leptons. Given the large data sample collected, it is possible to design validation regions that require at least four and even at least five jets with p_{T} >25 GeV in the event. Thus, two validation regions, WZ4j-VR and WZ5j-VR, are proposed to better probe the modelling of the jet multiplicity in WZ processes. Both regions are defined with exactly three signal leptons and no fourth baseline lepton, to reduce the ZZ background contamination. The m_{eff}, and the upper cut on the ratio between the $E_{\mathrm{T}}^{\mathrm{miss}}$ in the event and the sum of all lepton p_{T} are great discriminants against the reducible backgrounds. Some kinematic distributions after lepton and four jet selection are shown in Figure 7.2.

Purity in WZ4j-VR (WZ5j-VR) is around 67% (64%). When looking at

$\tilde{g} \to q\bar{q}(\tilde{\ell}\ell/\tilde{\nu}\nu)$ scenarios, the signal contamination is below 5% in most of the non-excluded phase space, except for small $\Delta M(\tilde{g}, \tilde{\chi}_1^0)$ where it can go up to 30% (15%). Signal contamination is found to be much lower for $\tilde{g} \to q\bar{q}WZ\tilde{\chi}_1^0$ scenarios.

$t\bar{t} + W$ background validation

A $t\bar{t} + W$ validation region ($t\bar{t}W$-VR) is defined with exactly one SS lepton pair and at least one b-jet. At least four jets are required in the ee and $e\mu$ channels, while in the $\mu\mu$ channel the selection is relaxed to at least three jets (less reducible background); also the jet p_{T} thresholds are different between these two cases (same motivation). As shown in Figure 7.3, the amount of $t\bar{t}$ background after this pre-selection is still very large and additional requirements on $E_{\mathrm{T}}^{\mathrm{miss}}$, m_{eff} and on the ratio between the sum of p_{T} of all b-jets and the sum of p_{T} of all jets are placed as mentioned in Table 7.1. With this definition the achieved purity in $t\bar{t}W$-VR is 33%. Signal contamination is around 20% when looking at $\tilde{b}\tilde{b}$ SUSY models.

$t\bar{t} + Z$ background validation

A $t\bar{t} + Z$ enriched validation region (ttZ-VR) is defined with at least one SFOS lepton pair and at least one b-jet. At least three jets are required in the event regardless of the lepton channel. Some kinematic distributions after this pre-selection are shown in Figure 7.4 (left and middle). To increase the purity, the invariant mass of the SFOS lepton pair is selected to be inside the [81, 101] GeVinterval and the m_{eff} in the event should be greater than 450 GeV. With this selection, the purity is 58%. One can increase it even further (by ~10%) if at

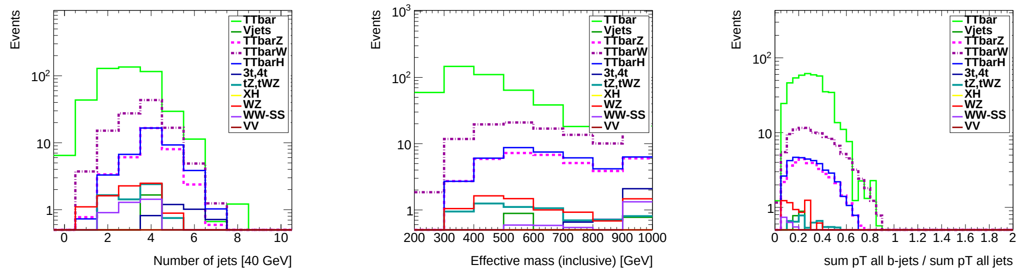

Figure 7.3: Number of jets with $p_{\mathrm{T}} > 40$ GeV(left), m_{eff} (middle) and ratio between the sum of all b-jets p_{T} and the sum of all jets p_{T} (right) after lepton and jet selection of the $t\bar{t}W$-VR (and no additional requirements). Signal regions are vetoed as detailed in Table 7.1. All MC samples are normalized to a luminosity of 36.1 fb^{-1}. Last bin includes overflow.

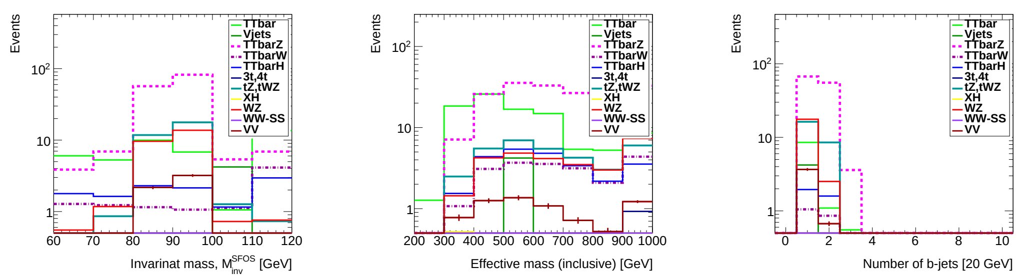

Figure 7.4: Invariant mass of the SFOS lepton pair (left) and m_{eff} (middle) after lepton and jet selection of the $t\bar{t}Z$-VR (and no additional requirements). Number of b-jets with $p_{\mathrm{T}} > 20$ GeVafter the $t\bar{t}Z$-VR selection. Signal regions are vetoed as detailed in Table 7.1. All MC samples are normalized to a luminosity of 36.1 fb^{-1}. Last bin includes overflow.

least two b-jets are required in the event. However, with such a cut the statistics will be highly reduced (up to a factor 2 lower as illustrated in Figure 7.4, right), so it is not pursued. The signal contamination is found to be around 5% for $\tilde{b}_1\tilde{b}_1^*$ pair production.

7.2.2 Validation of irreducible background estimates

The observed yields, compared with the background predictions and uncertainties, can be seen in Table 7.2. There is good agreement between data and the estimated background in all the validation regions.

7.3 Reducible Backgrounds

The reducible backgrounds consist of the charge-flip background and the FNP lepton background. The charge flip background is obtained by re-weighting opposite-sign lepton pairs data with measured charge-flip probability and cross checked with the estimate obtained with the MC template method. Two data-driven methods are used to estimate the FNP lepton background, the matrix method and the MC template method, which are combined to obtain the final estimate. These methods were discussed in detail in Chapter 6. This section describes the application of these methods in the context of the SS/3L analysis and the validation of the reducible background estimates.

7.3.1 Charge-flip Background

The lepton charge mis-measurement commonly referred to as "charge flip", is an experimental background strongly associated to analyses relying on same-sign leptons final states. In those events, the electric charge of one of the two leptons forming an opposite-sign (OS) pair, coming from an abundant SM process ($pp \to Z$, $t\bar{t}$, $W^+W^-\dots$), is mis-identified leading to a much rarer same-sign (SS) pair event. In most cases, the source of such a misidentification is the creation of additional close-by tracks $e^{\pm} \to e^{\pm}\gamma \to e^{\pm}e^{\pm}e^{\mp}$ via bremmstrahlung of the original electron when interacting with the material of the inner tracker. If one of the secondary electron tracks is subsequently preferred to the original track in the reconstruction of the electron candidate, the charge assigned to the electron might be incorrect, leading to a charge-flip event. Errors on the track charge assignment itself may occur as well, but they are much rarer. In the case of muons, charge-flip is essentially negligible due to the much smaller interaction cross-section with matter, and the requirement of identical charges to be measured for the inner tracker and muon spectrometer tracks.

A purely data-driven method is used to estimate event yields for the electron charge-flip background. Assuming that the electron charge flip rates $\xi(\eta, p_{\mathrm{T}})$ are known, a simple way to predict these yields is to select events with pairs of opposite-sign leptons in data and assign them a weight:

$$w_{\text{flip}} = \xi_1(1-\xi_2) + (1-\xi_1)\xi_2 \tag{7.1}$$

where $\xi_{(i)} = 0$ for muons.

The advantages of this method are a good statistical precision since the charge flip rate is quite small, and the absence of dependency to the simulation and related uncertainties. Obviously, it requires a precise measurement of the rates, which is described in this section. An inconvenience of this approach is that the reconstructed momentum for charge-flipped electrons tends to be negatively biased (too low by a few GeV), since such important bremmstrahlung topologies represent only a very small fraction of the cases used to tune electron energy calibration. Simply re-weighting electrons from opposite-sign lepton pairs therefore does not predict correctly the charge-flip background shape for variables very sensitive to the electron momentum, for example the m_{ee} lineshape. However, the kinematic range and variables used in the analysis are not senstitive to this effect and can safely be neglected.

For the nominal (tight) estimate of the charge-flip background contributions, only events with exactly two OS signal electrons are considered. Corrections in the fake lepton estimate however require estimating as well charge-flip contributions for selections involving baseline electrons failing signal requirements; for that reason, the charge-flip (loose) rate is measured for these two categories of electrons.

Methodology

Charge-flip rates are measured in data relying on a clean $Z \to ee$ sample ($75 < m_{ee} < 100$ GeV), in which the rates can be determined from the relative proportions of OS and SS electron pairs. Figure 7.5 illustrates this event selection. The rates are measured as function of η and p_{T}, to follow their dependency to the distribution of material in the detector, the bremmstrahlung emission rate, and the track curvature. Because of this binned measurements, and that the two electrons in a given pair generally have different kinematic properties, it has been found that the most efficient and less biased use of the available statistics is obtained by simultaneously extracting the rates in all bins via the maximization

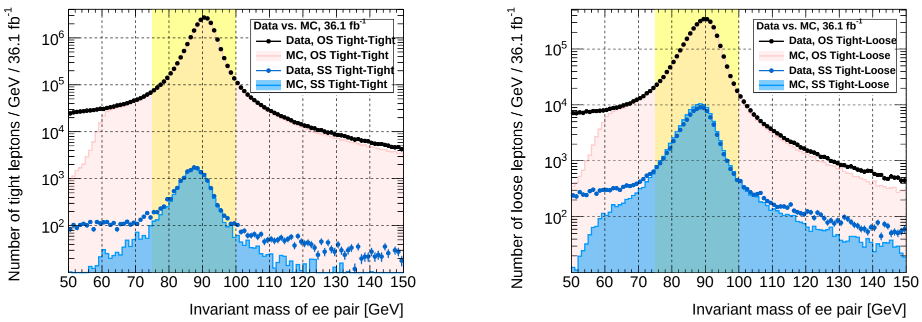

Figure 7.5: Invariant mass of opposite- and same-sign electron pairs, when both electrons satisfy signal requirements (left) or one of them fails them (right). Drell-Yan MC samples are not included, thus the drop in the MC distributions (light magenta filled area).

of the likelihood function describing the Poisson-expected yields of SS pairs:

$$
\begin{aligned}
&L(\{N_{\varpi}^{\mathrm{SS,obs}}\}|\{\xi(\eta, p_{\mathrm{T}})\}) = \\
&\prod_{\varpi} \mathcal{P}\left(N_{\varpi}^{\mathrm{SS,obs}} | w_{\mathrm{flip}}(\xi(\eta_1, p_{\mathrm{T},1}), \xi(\eta_2, p_{\mathrm{T},2})) \times N_{\varpi}^{\mathrm{OS+SS,obs}}\right)
\end{aligned}
\tag{7.2}
$$

with $\varpi = (\eta_1, p_{\mathrm{T},1}, \eta_2, p_{\mathrm{T},2})$ indexing bins, where (arbitrarily) $p_{\mathrm{T},1} > p_{\mathrm{T},2}$; the expression of w_{flip} is given by (7.1). Statistical uncertainties on the extracted charge-flip rates are obtained (in a standard way) from the likelihood's numerically-computed Hessian matrix.

In the nominal charge-flip measurement, the two electrons are required to satisfy signal requirements. To measure charge-flip rates for baseline electrons failing signal (noted $\bar{\xi}$ below), pairs with only one signal electron are used; this provides larger statistics than applying (7.2) to electrons pairs where both fail the signal cuts. However, the expression of the likelihood has to be adapted due to the induced asymmetry between the two electrons forming the pair:

$$\begin{aligned} &L(\{N_{\varpi}^{\mathrm{SS,obs}}\}|\{\xi(\eta_1, p_{\mathrm{T},1})\}, \{\bar{\xi}(\eta_2, p_{\mathrm{T},2})\}) = \\ &\prod_{\varpi} \mathcal{P}\left(N_{\varpi}^{\mathrm{SS,obs}} | w_{\mathrm{flip}}(\xi(\eta_1, p_{\mathrm{T},1}), \bar{\xi}(\eta_2, p_{\mathrm{T},2})) \times N_{\varpi}^{\mathrm{OS+SS,obs}}\right) \end{aligned} \tag{7.3}$$

where this time $(\eta_1, p_{\mathrm{T},1})$ corresponds to the signal electron. Using the same η and p_{T} binnings for both measurements, the number of free variables in the maximization of (7.3) – as well as the number of terms in the product forming L – is twice larger than for the nominal case (7.2). In fact, a by-product of the maximization of (7.3) is another determination of the charge-flip rates for signal electrons, although with a more limited precision than obtained in the nominal measurement (7.2).

Background subtraction is performed through a simple linear extrapolation of the invariant mass distribution sidebands; it matters mostly for low p_{T} in the nominal measurement, and for the additional measurement with baseline electrons failing signal requirements, where the level of background is larger.

Measured rates

The charge-flip rates measured in data and MC are shown on Figure 7.6. In data, the nominal rates (Fig. 7.6a) go up to $\sim$0.1% in the barrel region ($|\eta| < 1.37$), while it increases up to $\sim$0.2% in the end-cap region ($|\eta > 1.37|$). For baseline electrons failing signal requirements (Fig. 7.6c), the rates are in general greater than the nominal ones in every bin, as expected. The charge-flip rates for these electrons go up to $\sim$0.5% in the barrel region and up 1% in the end-cap region. Compared to the rates used in the previous version of the analysis [51], the

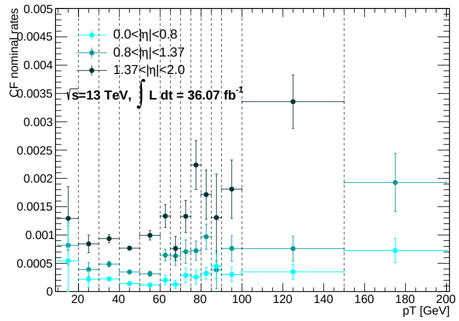

(a) Data, signal electrons

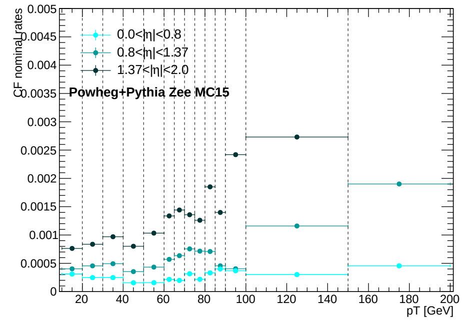

(b) MC, signal electrons

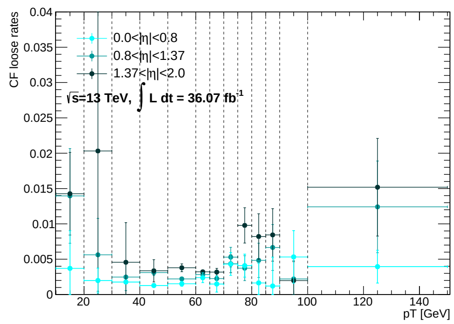

(c) Data, baseline-failing-signal

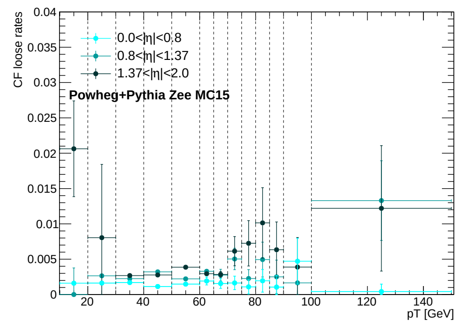

(d) MC, baseline-failing-signal

Figure 7.6: Charge-flip rate as measured in data (left) and MC (right). Only the statistical uncertainty is displayed. The last p_{T} bin is inclusive.

central values are much lower now. After suppressing the charge flip events with the charge-flip electron BDT classifer described in Section 5.4.3, the charge flip rates are strongly reduced for both signal and baseline-failing-signal electrons (up to a factor 20 in some bins). Figure 7.7 illustrates the charge flip background reduction in a loose selection. Below 30 GeV the statistics is very low for the loose measurement; however, these results are used only to measure the electron fake rate and, as illustrated in Figure 7.13, in this p_{T} interval the charge flip background is negligible.

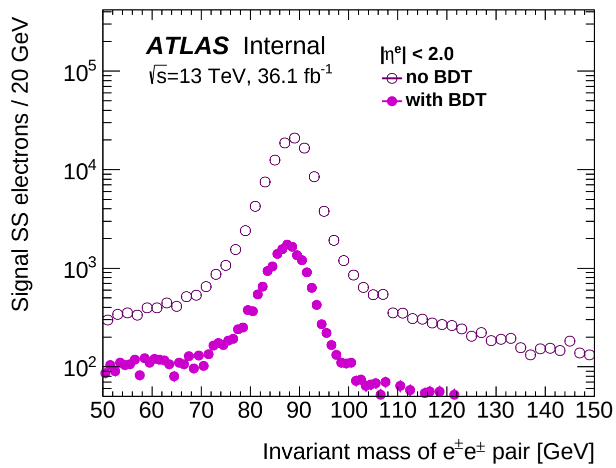

Figure 7.7: Invariant mass of the signal $e^{\pm}e^{\pm}$ pair distribution with (full markers) and without (open markers) charge-flip electron BDT selection applied.

The charge-flip rates in MC (Figs. 7.6b, 7.6d) are obtained by applying the same methodology as in data. Generally, the rates are not very far from data, validating the use of MC to predict charge-flip background in several of the optimization studies presented in this document. In addition, a closure test is performed on $t\bar{t}$ MC, checking that weighted OS events can reproduce the distribution of SS charge-flip events (identified by truth-matching). A good overall agreement is found, largely within the assigned uncertainties as shown in Figure 7.8.

Systematic uncertainties

The main uncertainties on the measured charge-flip rates come from the presence of background and the way it is estimated. To assess them, variations of the selection and background estimation are considered:

1) $75 < m_{ee} < 100$ GeV, no background subtraction;

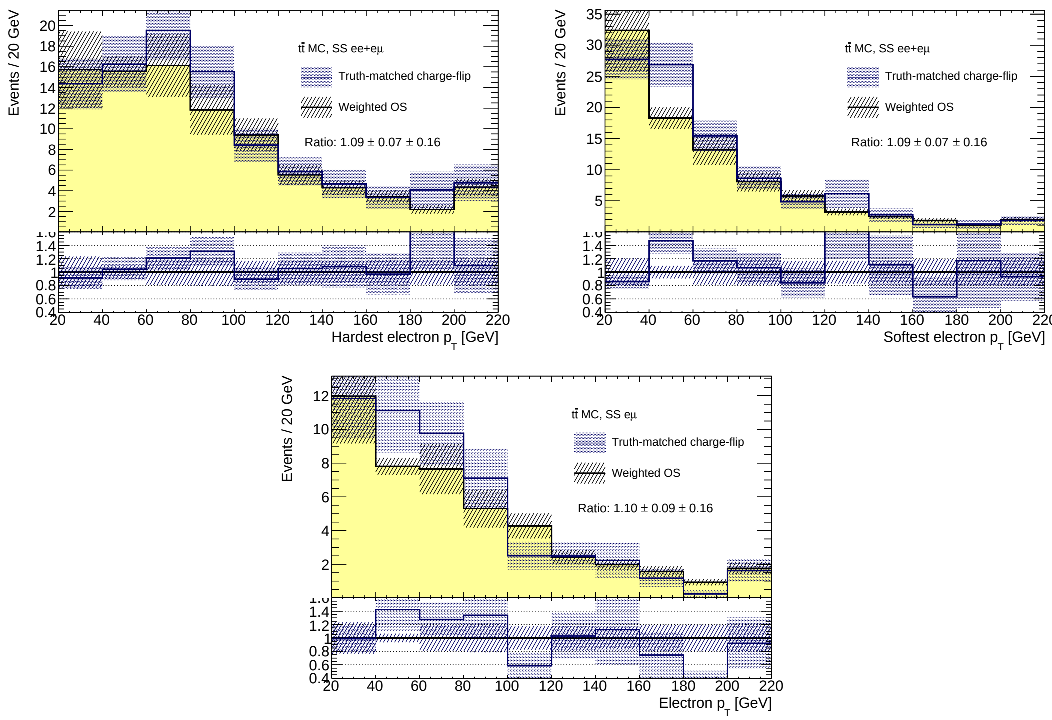

Figure 7.8: Closure test for the charge-flip background prediction, for simulated $t\bar{t}$ events using charge-flip rates measured in $Z \to ee$ MC (with the systematic uncertainties from the data measurements, though). Events are selected in the $e\mu$ and ee channels, using signal leptons only, and charge-flipped electrons are identified by truth-matching.

2) $75 < m_{ee} < 100$ GeV, sidebands of 20 GeV;

3) $75 < m_{ee} < 100$ GeV, sidebands of 25 GeV(nominal measurement);

4) $75 < m_{ee} < 100$ GeV, sidebands of 30 GeV;

5) $80 < m_{ee} < 100$ GeV, sidebands of 20 GeV.

The effect of applying the background subtraction itself is evaluated by comparing configurations 1 and 3. The impact of the width of the m_{ee} chosen for the

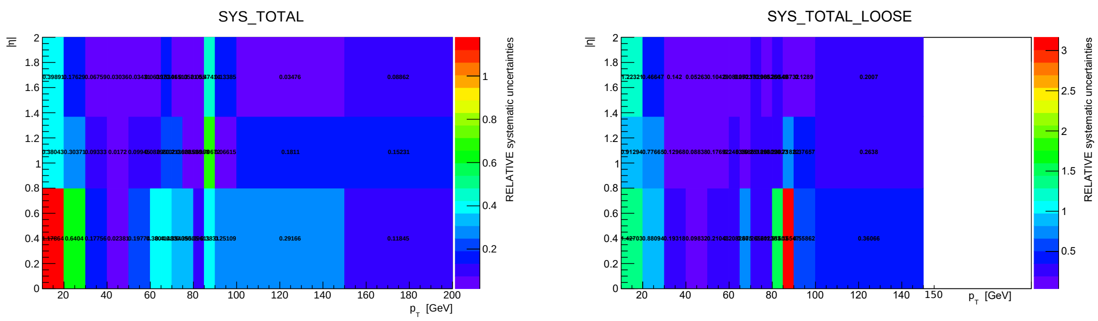

(a) (b)

Figure 7.9: Total systematic uncertainties on the charge-flip rates for electrons satisfying the signal requirements (7.9a), and for baseline electrons failing the signal requirements (7.9b).

measurement is by comparing configurations 3 and 5, while the sideband width effects are evaluated by comparing configuration 3 and 2, or 3 and 4. The largest deviation in each bin is taken as the systematic uncertainty on the charge-flip rate.

The resulting systematic uncertainties on the charge-flip rates are presented in Fig. 7.9.

For the signal electrons charge-flip rates the systematic uncertainties vary in general between 2% and 20% (increasing up to > 50% in the region with $p_{\mathrm{T}} < 10$ GeV), whereas for baseline-failing-signal electrons they vary between 3% and 30% (increasing up to > 50% in the region with $p_{\mathrm{T}} < 10$ GeV). Part of these large values, at low p_{T} and in the [80,90] GeV p_{T} interval, can be explained by large statistical fluctuations between the different configurations.

7.3.2 Matrix Method

The matrix method relates the number of events containing prompt or FNP leptons to the number of observed events with tight or loose-not-tight leptons using the probability for loose prompt or FNP leptons to satisfy the tight criteria. The formalism for this mehtod has been discussed in Section 6.4. The next sections will concentrate on the measurement of the two input variables needed for the matrix method: the probability for loose FNP leptons to satisfy the tight selection criteria (ζ) and the probability for loose prompt leptons to satisfy the tight selection criteria (ε).

Baseline-to-signal efficiency for fake muons

Baseline-to-signal efficiency for fake leptons (further called "fake rate", (ζ)) is measured in a sample enriched in fake leptons from $t\bar{t}$ processes. The MC simulations indicate that this background has the largest contribution to FNP lepton background in the signal regions, even those with b-jet vetoes, due to the requirements on jet multiplicity and $E_{\mathrm{T}}^{\mathrm{miss}}$. The events used for the measurements require exactly two same-sign muons (and no extra baseline lepton), at least one b-jet, and at least 3 jets that were acquired by di-muon triggers. One of the muons in the event (referred to as "tag") is required to satisfy signal requirements, verify $p_{\mathrm{T}} > 25$ GeV, and trigger the event recording. The measurement may then be performed on the other lepton ("probe"), likely to be the fake lepton of the pair.

Figure 7.10a shows the number of signal muon probes available after this

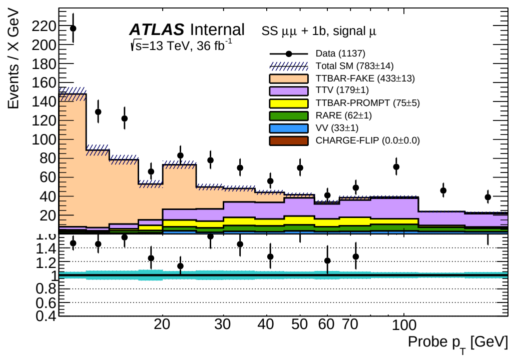

(a)

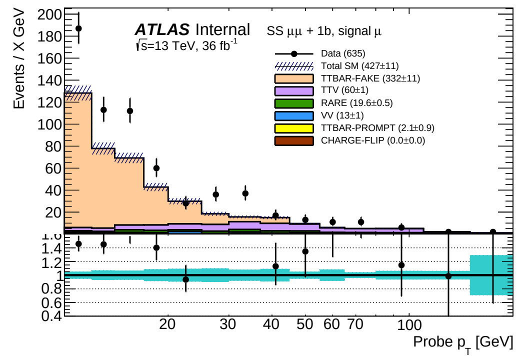

(b)

Figure 7.10: Signal probe muon p_{T} distribution in data and MC, after preselection (left) or further tightening of the tag muon requirements (right). The yellow area indicates $t\bar{t}$ events in which the tag muon is fake and the probe real, leading to a measurement bias.

preselection. It is clear that at this stage, measurements above 25 GeV would be very affected by the important fraction of events in which the tag muon is fake and the probe muon is real. To overcome this issue, two alternatives are considered:

- tighten the p_{T} and isolation requirements of the tag muon beyond the "signal" requirements, to reduce its probability of being a fake muon
- use an identical selection for tag and probe muons, and require them to be in the same (p_{T},η) bin for the measurement; after subtraction of estimated contributions from processes with two prompt muons, all events have one real and one fake muon, and the symmetry in the muon selection can be

taken advantage of to obtain an unbiased measurement of the fake rate:

$$\zeta = \frac{\varepsilon n_2}{\varepsilon n_1 + (2\varepsilon - 1)n_2}$$

with n_1, n_2 the number of events with 1 or 2 signal muons, and ε the efficiency for prompt muons.

This method is limited to measurements in inclusive or wide bins. It also can't be used at too low p_{T}, due to contributions from processes with two fake muons (e.g. from $B\bar{B}$ meson production).

Comparisons made with $t\bar{t}$ MC indicated that when using a very tight isolation requirement on the tag muon ($\max(E_{\mathrm{T}}^{\text{topo, cone 40}}, p_{\mathrm{T}}^{\text{cone 40}}) < 0.02 \times p_{\mathrm{T}}$), the level of bias is always largely inferior to the statistical uncertainty in the measurement, which itself is smaller than for the other two methods.

Figure 7.10b shows the number of signal muon probes when applying those reinforced isolation criteria to the tag muon, as well as requiring $p_{\mathrm{T}}^{\text{tag}} > \max(40, p_{\mathrm{T}}^{\text{probe}} + 10)$ GeV. As expected, the number of pairs with a fake tag muons is down to a minor level, at least according to the simulation.

Muon fake rates as predicted by the simulation ($t\bar{t}$, inclusive selection of leptons via truth-matching) are shown on Fig. 7.11 as function of p_{T} and $|\eta|$. One can expect a moderate dependency of the fake rates to the transverse momentum, with the strongest evolution at low p_{T} and a slight increase toward higher p_{T}. The fake rates are also essentially independent of the pseudorapidity, except at the edge ($|\eta| > 2.3$) where there is a strongly pronounced increase of the rates. This motivates measurements in data as function of p_{T} in two $|\eta|$ bins.

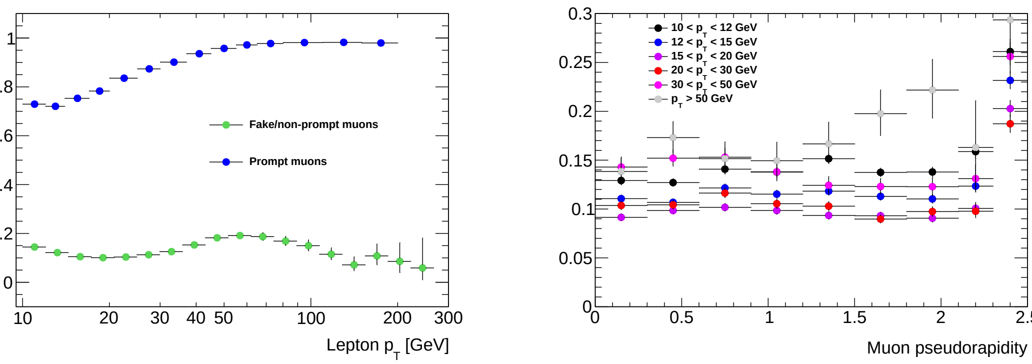

(a) (b)

Figure 7.11: Muon fake rates in $t\bar{t}$ MC with an inclusive selection, as function of p_{T} (left, green markers) or $|\eta|$ in different momentum ranges (right).

Observations in data seem to indicate that the rejection of fake tag muons by the reinforced isolation criteria is quite less important than in the simulation, or that the amount of fake muons at high p_{T} is larger than in the simulation, or both. This leads to an unknown level of bias in measurements performed with the straightforward tag-and-probe selection at high p_{T}. For that reason, the final rates measured in data are provided by the tag-and-probe method below 25 GeV, and by the symmetric selection for $p_{\mathrm{T}} > 25$ GeV. The former are obtained with

$$\zeta = \frac{n^{\mathrm{data}}_{\mathrm{signal}} - n^{\mathrm{MC}}_{\mathrm{signal}}}{n^{\mathrm{data}}_{\mathrm{baseline}} - n^{\mathrm{MC}}_{\mathrm{baseline}}} \tag{7.4}$$

$$\text{with } \Delta\zeta_{\mathrm{stat}} = \frac{\sqrt{(1-2\zeta)n^{\mathrm{data}}_{\mathrm{signal}} + \zeta^2 n^{\mathrm{data}}_{\mathrm{baseline}}}}{n^{\mathrm{data}}_{\mathrm{baseline}} - n^{\mathrm{MC}}_{\mathrm{baseline}}}$$

while the latter are obtained with:

$$\zeta = \frac{\varepsilon(n^{\text{data}}_{\text{both signal}} - n^{\text{MC}}_{\text{both signal}})}{\varepsilon(n^{\text{data}}_{\text{only 1 signal}} - n^{\text{MC}}_{\text{only 1 signal}}) + (2\varepsilon - 1)(n^{\text{data}}_{\text{both signal}} - n^{\text{MC}}_{\text{both signal}})} \tag{7.5}$$

$$\text{with } \Delta\zeta_{\text{stat}} = \frac{\zeta}{n^{\text{data}}_{\text{both signal}} - n^{\text{MC}}_{\text{both signal}}}\sqrt{\zeta^2 n_{\text{only 1 signal}} + \left(1 - \frac{2\varepsilon - 1}{\varepsilon}\zeta\right)^2 n_{\text{both signal}}}$$

the efficiency for prompt muons ε is assigned values compatible with section 7.3.2.

The measured rates are presented in Table 7.3. The central values are shown together with the associated statistical uncertainty, as well as the propagation of the uncertainty on the subtracted backgrounds normalization, which is taken as a global $\Delta B/B = 20\%$. The rates are of the order of 10% up to 30 GeV, beyond which they increase. Overall these values are not very different from those predicted by the simulation.

Some of the validation and signal regions require events with 2 or more b-tagged jets, which reduces the fraction of non-prompt muons coming from B meson decays. Figure 7.12 illustrates how this impacts on the fake rates. Given the good agreement between data and simulation for the measured values, A correction is applied to the measured rates for events with ≥ 2 b-jets, taken directly from simulated $t\bar{t}$ events. This correction factor varies between 1 and 2 with p_{T}, and the whole size of the correction is assigned as an additional systematic uncertainty (see Table 7.4).

Systematic uncertainties

To cover potential differences in the fake rates between the measurement regions and the signal regions, that could be due to different origins or kinematic properties of the fake leptons, uncertainties are set based on the extent of those differences

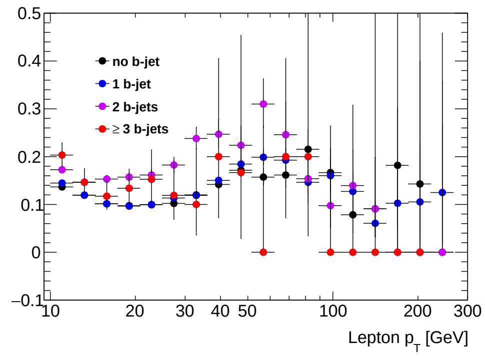

Figure 7.12: Muon fake rates in $t\bar{t}$ MC with an inclusive selection, as function of p_{T} and split according to the number of b-tagged jets in the event.

predicted by the simulation. The largest effect is the decrease of the fake rates with H_{T} (especially for high-p_{T} muons), which likely correlates to a harder jet at the origin of the non-prompt muon, hence a reduced likelihood to satisfy isolation requirements. Table 7.4 summarizes the additional systematic uncertainties applied to the muon fake rates. They vary from 30% at low p_{T}, to up to 85% for $p_{\mathrm{T}} > 40$ GeV; in that range, the uncertainties are made H_{T}-dependent.

As already shown, Fig. 7.12 shows the variation of the fake rate in $t\bar{t}$ MC as function of the number of b-tagged jets in the event. Unsurprisingly, the rates are very similar for $0b$ and $\geq 1b$ final states, justifying the use of the fake rates measured in this section (i.e. in a $\geq 1b$ region) to predict fake muon background in all signal regions.

Baseline-to-signal efficiency for fake electrons

Electron fake rates are measured with a similar methodology, but the $e^{\pm}e^{\pm}$ channel is unusable due to the presence of a large charge-flip background. This is overcome

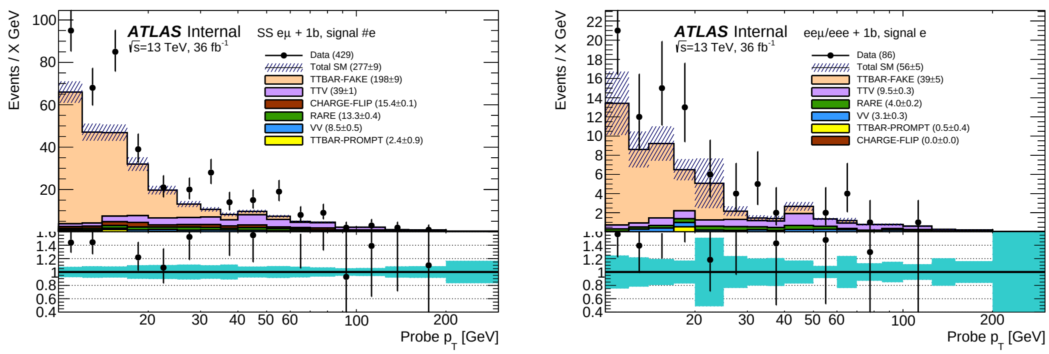

Figure 7.13: Signal probe electron p_{T} distribution in data and MC, for $e^{\pm}\mu^{\pm}$ pairs (left, with probe electrons satisfying CFT cut and a reinforced tag muon selection) or $\ell^{\pm}e^{\mp}e^{\mp}$ pairs (right, with reinforced tag electron selection), as described in section 7.3.2. The yellow area indicates $t\bar{t}$ events in which the tag lepton is fake and the probe electron real, leading to a measurement bias.

by working with $e^{\pm}\mu^{\pm}$ pairs instead (with a tag muon), but mixing leptons of different flavours brings additional complications (for example, the unbiased measurement cannot be employed to measure muon fake rates at higher p_{T}, as there is no symmetry between the leptons). To improve confidence, measurements are performed in four different ways, which complement each other:

- straightforward tag-and-probe with $e\mu$ pairs, with the same tag muon selection as in the previous section.

- same selection, but subtracting from the numerator the number of pairs with one fake tag muon and one prompt probe electron, itself estimated from the number of observed $e\mu$ events with a muon failing signal requirements, scaled by an efficiency correction factor $e\mu/\mu\mu$ taken from $t\bar{t}$ MC (only for pairs with one fake muon). This only works if the two muons satisfy the same kinematic requirements, therefore can be used only for measurements in wide or inclusive bins.

- selecting $\ell^{\mp}e^{\pm}e^{\pm}+\geq 1b$ events, with a Z veto on SFOS pairs. This selection entirely suppresses contributions from charge-flip, or events with fake muons. One of the electron, with standard signal requirements, is required to satisfy the same reinforced p_{T} and isolation requirements as for the muon measurement, and the measurement can be performed on the other electron.

- same selection, using the symmetry between the two same-sign electrons to measure the rates in an unbiased way, similarly to the muon case.

Events are acquired with the combination of single-muon (as in previous section) and $e\mu$ triggers.

Figure 7.13 shows the number of signal probe electrons selected in the $e\mu$ and ℓee channels. There are quite less events selected in the trilepton channel. Figure 7.14 shows the electron fake rate as a function of p_{T} or η in $t\bar{t}$ MC. The variations of the rates as function of the pseudorapidity are not very large, therefore measurements are only performed as a function of p_{T}. The low p_{T} range is dominated by non-prompt electrons from heavy flavour decays, while beyond 30 GeV, electron fakes mostly come from conversions of photons produced inside jets, such as $\pi^0 \to \gamma\gamma$ decays.

Based on the estimated levels of bias, and achievable statistical precision, of the different methods, the electron fake rate is measured with the tag-and-probe

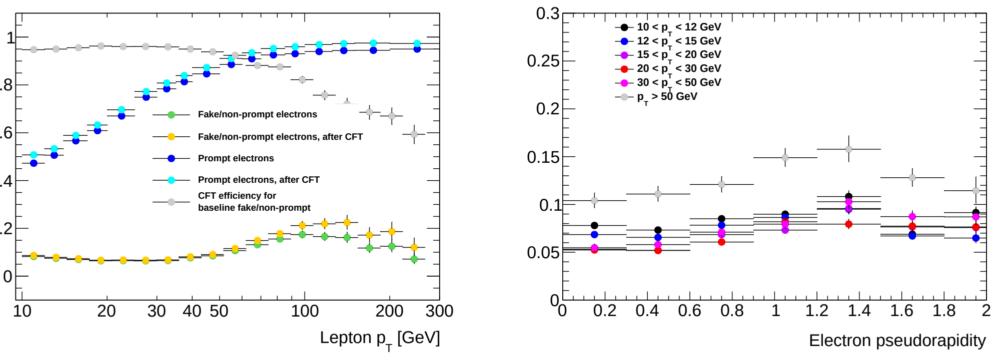

Figure 7.14: Electron fake rates in $t\bar{t}$ MC with an inclusive selection, as function of p_{T} (left, yellow/green markers = with/without CFT cut applied) or $|\eta|$ in different momentum ranges (right).

$e\mu$ selection up to 30 GeV, and by combining "unbiased" evaluations in both $e\mu$ and ℓee channels beyond. The measured rates are presented in Table 7.5, together with the associated statistical and background-subtraction uncertainties. The rates are of the order of 10% up to 30 GeV, beyond which they increase to up to 25%.

Unlike muons, MC-based correction factors are not applidd for final states with ≥ 2 b-tagged jets. This is because there is less good agreement between the measured rates and the simulation; in particular the former take larger values in the medium-p_{T} range.

Systematic uncertainties

Similarly to the muon case, systematic uncertainties are assigned to cover for difference in the rates in the measurement regions and in the signal regions that would be due to different sources of fake leptons, or different kinematic properties of these sources. Unlike muons, there is much less of a dependency to H_{T}. The dominant source of potential differences is therefore the origin of the fake electron (see Fig. 7.15); for $p_{\mathrm{T}} < 20$ GeV, non-prompt electrons from heavy–flavor hadron decays dominate, which is confirmed by the good agreement between MC fake rates and those measured in data. In that range, an uncertainty of 30% is assigned to the fake rates (inflated to 50% for final states with $\geq 2b$-tagged jets). The rates measured in data are larger than those predicted by the simulation, and would for example be consistent with a larger amount of electrons from photon conversions than predicted. In that range, an uncertainty of 50% is assigned to cover any arbitrary variation of the relative contributions of each source.

Finally, Figure 7.16 shows the variation of the fake rate in $t\bar{t}$ MC as function of the number of b-tagged jets in the event. As expected, the rates are very similar for $0b$ and $\geq 1b$ final states, justifying the use of the fake rates measured in this section (i.e. in a $\geq 1b$ region) to predict fake electron background in all signal regions.

Baseline-to-signal efficiency for real leptons

Baseline-to-signal efficiency for real leptons is measured in a high purity data sample of opposite-sign same-flavor leptons with the standard Z tag-and-probe method. Events are selected by a single lepton trigger. The tag lepton, required to have triggered the event recording, also satisfies signal requirements and verifies $p_{\mathrm{T}} > 25$ GeV. The probe lepton used for the efficiency measurement satisfies baseline requirements. All possible tag-and-probe combinations are considered

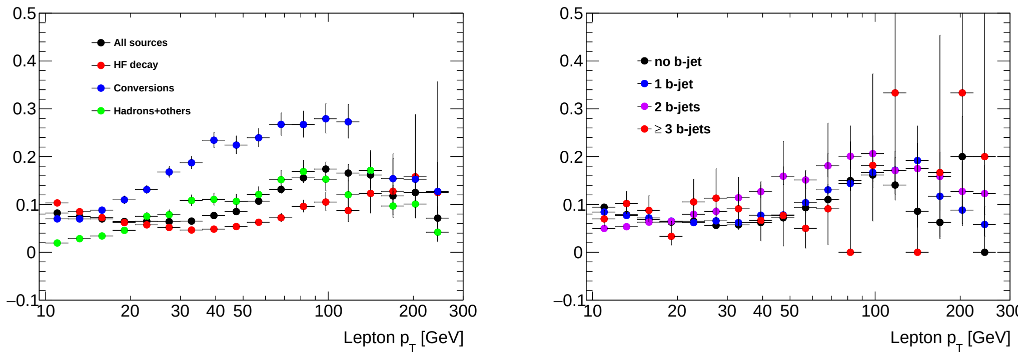

Figure 7.15: Electron fake rates in $t\bar{t}$ MC with an inclusive selection, as function of p_{T} and split according to the source of the fake electron (left). The relative contributions of each source (for signal electrons) are indicated on the right-hand-side.

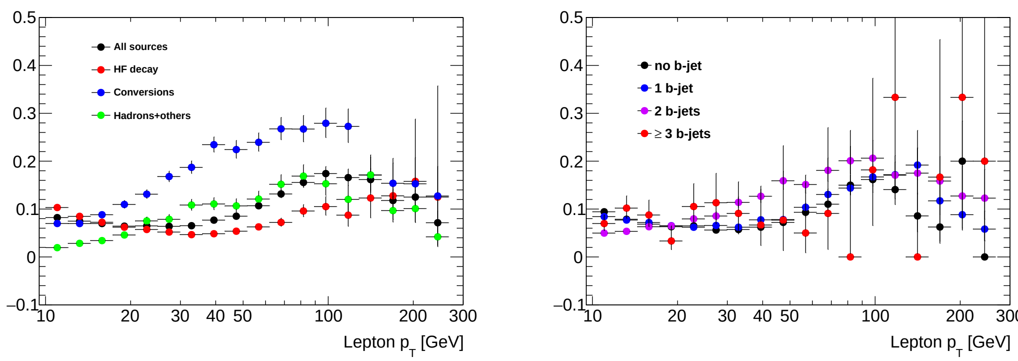

Figure 7.16: Electron fake rates in $t\bar{t}$ MC with an inclusive selection, as function of p_{T} and split according to the number of b-tagged jets in the event.

in an event (including permutation of the tag and probe leptons), as long as the invariant mass of the pair is comprised between 80 and 100 GeV. Figure 7.17 illustrates this event selection.

A non-negligible background contamination in the electron channel affects measurements below $p_{\mathrm{T}} = 20$ GeV. This contamination is taken into account in the

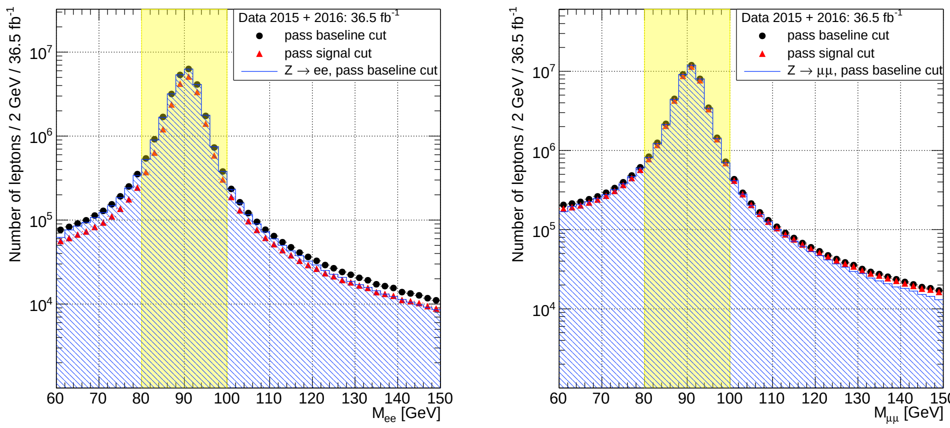

Figure 7.17: Invariant mass of opposite-sign same-flavor electrons (left) and muons (right), after the tag selection, where the probe satisfies the baseline requirements or the signal requirements.

measurement using a background template method inspired by the method used to measure reconstruction, identification, and isolation efficiencies documented in [52]. This template is built from the tag-and-probe invariant mass distribution for baseline-level probe electrons that fail both tight identification and isolation requirements, smoothed by assuming an exponential shape whose parameters are determined by a fit in the interval $60 < m_{ee} < 120$ GeV excluding the $80 < m_{ee} < 100$ GeV region. The background template is then normalized to the main tag-and-probe distribution in the background-dominated tail $120 < m_{ee} < 150$ GeV. The estimated level of background goes up to 4%, reached for probe electrons with $p_{\mathrm{T}} < 15$ GeV and $|\eta| < 0.8$.

The efficiency is measured as a function of p_{T} and η, and the results are presented in Fig 7.18 for electrons and muons. The background subtraction is

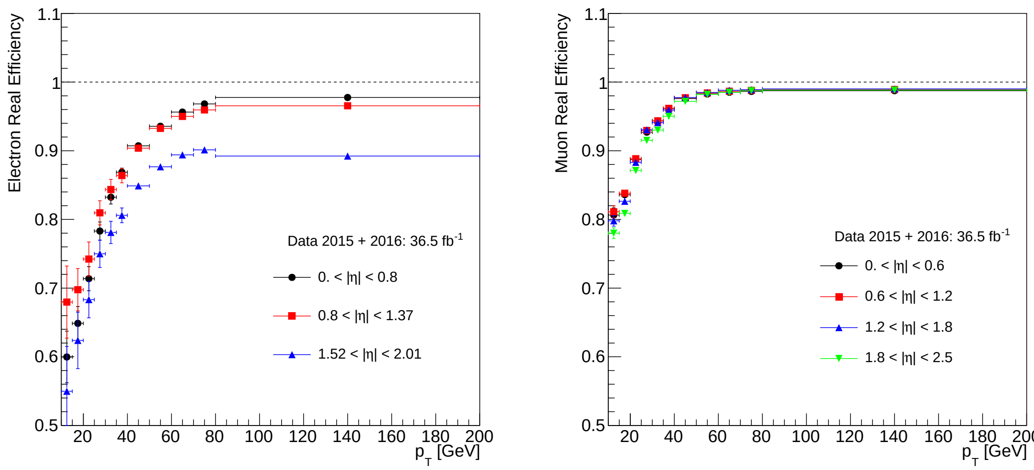

(a) Electrons (b) Muons

Figure 7.18: Baseline-to-signal efficiencies as a function of p_{T} and $|\eta|$ for real electrons (left) and muons (right), measured in 2015+2016 data. The $|\eta|$ binning used in the electron case corresponds to the geometry of the electromagnetic calorimeter. For muons a homogeneous $|\eta|$ binning is considered. The error bars corresponds to the quadratic sum of the statistical and tag-and-probe measurement systematic uncertainties.

applied on the electron channel only. The following systematic uncertainties are assigned to the measured efficiencies:

- Background contamination: 27 variations of the tag-and-probe method are considered to assess the electron measurement systematics. Three m_{ee} windows and 9 variations of the background subtraction methods are considered. The largest contribution to the systematics arises from the m_{ee} window variation. This is expected as the proportion of electrons affected by bremsstrahlung depends on m_{ee}. The resulting relative systematics vary from 6% $\sim$ 12% in the $10 < p_{\mathrm{T}} < 15$ GeV region, 3% to 6% in the $15 < p_{\mathrm{T}} < 20$ GeV region, 1% to 3% in the $20 < p_{\mathrm{T}} < 40$ GeV region, and less than 1% for $p_{\mathrm{T}} > 40$ GeV. The systematic uncertainties associated to the muon efficiencies measurement vary from 1% to 1.3% in the $10 < p_{\mathrm{T}} < 15$ GeV region and less then 1% for $p_{\mathrm{T}} > 15$ GeV.

- Trigger: a systematic uncertainty accounting for a potential bias at trigger level is considered and it varies between 0 and 4%, depending on the p_{T} range.

- Extrapolation to busy environments: efficiencies are typically lower in such environments due to the proximity of jets and leptons; an uncertainty is assigned by comparing efficiencies in simulated $Z \to \ell\ell$ and $\tilde{g} \to t\bar{t}\tilde{\chi}_1^0$ events, for $\Delta m(\tilde{g}, \tilde{\chi}_1^0) > 1$ TeV which represents an extreme case of final states with highly boosted top quarks. The uncertainty, taken as the difference in efficiencies, is parametrized as a function of p_{T} and ΔR (the angular distance between the lepton and the closest jet).

The resulting systematic uncertainties are summarized in Table 7.6 and Table 7.7.

7.3.3 MC Template Method

As discussed in Section 6.3.1, the MC template method is a simulation-based method that provides an alternative estimate of the reducible backgrounds affecting the analysis. It relies on the correct modelling of FNP leptons and charge-flipped electron kinematics in $t\bar{t}$ and V+jets. FNP leptons are classified in four categories, namely electrons and muons coming from b and light-quark jets. Normalisation factors for each of the five sources (including phton conversions) are computed to match the observed data in dedicated control regions. The fifth category is events with prompt electrons that have a charge mis-measurement (charge flip, EL HF, MU HF, EL LF, MU LF). Six non-overlapping control regions are defined by the presence of b-jets and by the flavors of the same sign lepton pair in the event:

- CR0b: events without b-jets in ee, $e\mu$, and $\mu\mu$ channels.
- CR1b: events with at least one b-jet in ee, $e\mu$, and $\mu\mu$ channels.

All the selected events contain two or more same-sign signal leptons and $E_{\mathrm{T}}^{\mathrm{miss}} > 40$ GeV and 2 or more jets. Events satisfying the signal regions requirements are excluded from the control regions. The purpose of the $E_{\mathrm{T}}^{\mathrm{miss}}$ requirement is to remove multi-jet events that have two or more FNP leptons and tend to have low $E_{\mathrm{T}}^{\mathrm{miss}}$. The six distributions are chosen for variables that provide the best separation between processes with prompt leptons and processes with fake leptons and charge flip and are shown before and after the fit in Figures 6.2-6.4 and Figures 6.3-6.5, respectively. The multipliers obtained after the minimization of the negative log likelihood were given in Tables 6.1 and 6.2. The tables represent the correction factors obtained from the fit upon using two different parton showers, Pythia and Sherpa for the processes that lead to non-prompt leptons and charge flips. The goal of varying the parton shower is to access the dependence of the fake and charge flip estimates on the choice of the parton shower.

The MC template method is validated by looking at the agreement between observed data and prediction as shown in Figure 7.22 and Figure 7.22. In the MC template method, the systematic uncertainty is obtained by changing the generator from POWHEG-BOX to SHERPA and propagating uncertainties from the control region fit to the global normalization scale factors applied to the MC samples. The uncertainties in these scale factors are in the range 75–80%, depending on the SRs. In practice, only $t\bar{t}$ contributes to the SRs and the final yields with systamtic uncertainties from fit uncertainty, theory uncertainties on ttbar, comparison of different showers (Pythia 6 and Sherpa) is shown in Table 7.8. This table also shows a global correction factor derived by taking the ratio of the weighted $t\bar{t}$ to raw MC $t\bar{t}$ with a global uncertainty that includes all systematic uncertainties used to obtain the final estimate.

7.3.4 Reducible Background Validation

The reducible backgrounds estimated with the methods described in the previous sections are validated by comparing observed data to predicted background after various kinematic requirements. The next sections will validate the MC template method used to estimate the charge flip and the FNP lepton background, and the matrix method used to estimate the FNP lepton background.

Data/MC comparisons

The overall level of agreement obtained by the matrix method can be seen in different channels in Fig 7.19. The distributions of several variables are shown on Fig 7.20 for an inclusive same-sign leptons selection after various requirements on the number of jets and b-jets. These distributions illustrate that the data are described by the prediction within uncertainties. The apparent disagreement for m_{eff} above 1 TeV in Figure 7.20d is covered by the large theory uncertainty for the diboson background, which is not shown but amounts to about 30% for m_{eff} above 1 TeV. Similar distributions for the other main variables can be found in Appendix B. To avoid the presence of signal in the tails of these distributions, events belonging to any of the signal regions are vetoed both in data and for the predicted backgrounds.

Figure 7.21 shows a comparison between the estimates of the MC template method and the matrix method in a loose selection. Other $E_{\mathrm{T}}^{\mathrm{miss}}$ distributions with events satisfying the signal region requirements except the $E_{\mathrm{T}}^{\mathrm{miss}}$ cut are shown in Figure 7.22 comparing the two methods.

Reducible background estimates

The expected yield for processes with FNP leptons and charge-flip electrons, estimated with the matrix method, likelihood method (charge-flip), and the MC template method are presented in Table 7.9 and Table 7.10for the signal regions and Table 7.11 for the validation regions. Since the predictions from the MC

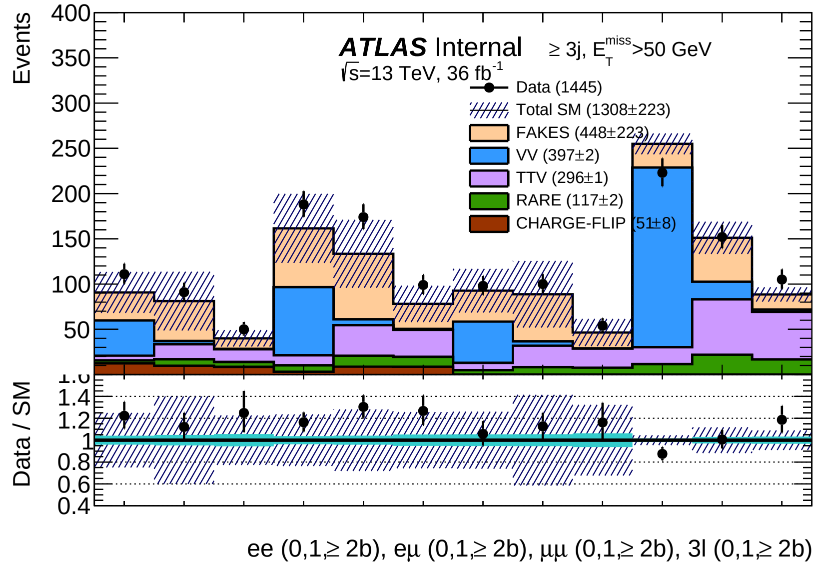

Figure 7.19: Summarized level of agreement between observed data (2015+2016, 36.5 fb^{-1}) and expected SM+detector backgrounds for events with ≥ 2 same-sign leptons ($p_{\mathrm{T}} > 20\mathrm{GeV}$), $E_{\mathrm{T}}^{\mathrm{miss}} > 50\mathrm{GeV}$ and ≥ 3 jets ($p_{\mathrm{T}} > 40\mathrm{GeV}$), split as function of the lepton flavours and the number of b-tagged jets. Uncertainties include statistical sources, as well as systematic uncertainties for the data-driven backgrounds; for illustration, statistical uncertainties alone are shown in the light-coloured error bands in the ratio plots. Events belonging to any of the signal regions are rejected, both in data and MC.

template and matrix methods in the signal and validation regions are consistent with each other, the final numbers retained for the FNP lepton background estimate (also shown in the tables) are taken as the weighted-average of the predictions from the matrix method and the MC template; the weights are based on the statistical component, and the systematic uncertainties are propagated assuming conservatively a full correlation between the two methods (although they are in fact largely independent!). The central value and statistical/systematic uncertainties are therefore:

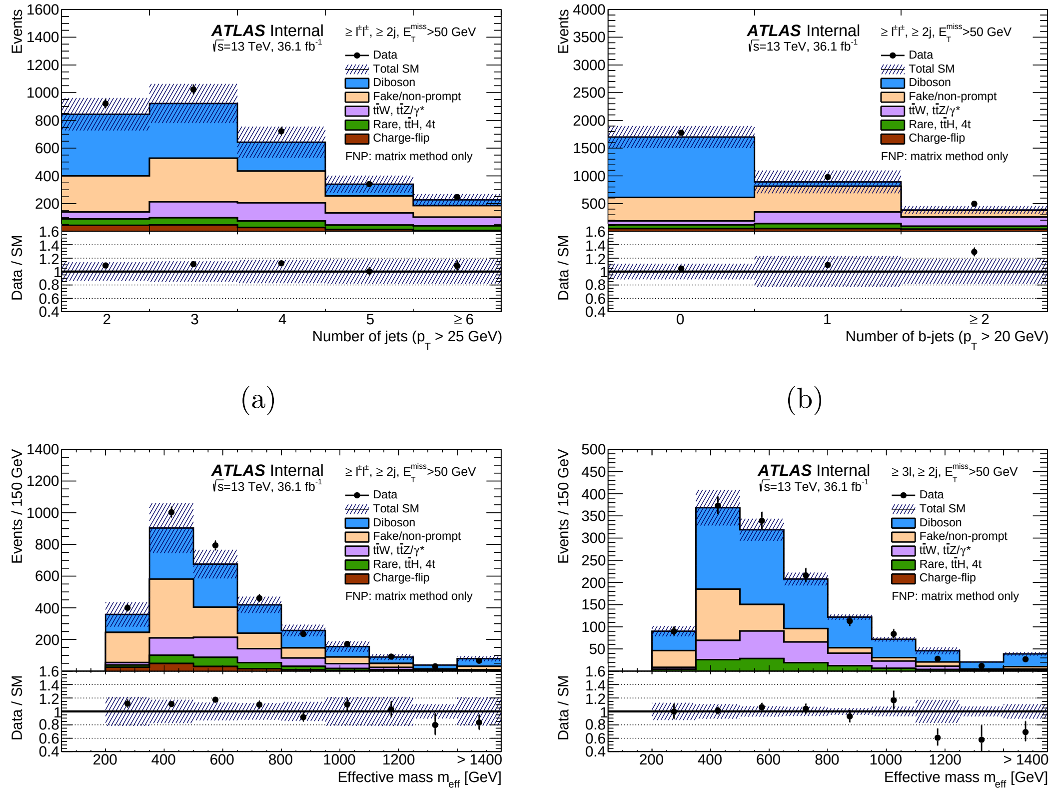

(a) (b)

(c) (d)

Figure 7.20: Distributions of (a) the number of jets, (b) the number of b-tagged jets and (c), (d) the effective mass. The distributions are made after requiring at least two jets ($p_{\mathrm{T}} > 40$GeV) and $E_{\mathrm{T}}^{\mathrm{miss}} > 50$GeV, as well as at least two same-sign leptons ((a), (b), (c)) or three leptons (d). The uncertainty bands include the statistical uncertainties for the background prediction as well as the systematic uncertainties for fake- or non-prompt-lepton backgrounds (using the matrix method) and charge-flip electrons. Not included are theoretical uncertainties in the irreducible background contributions. The rare category is defined in the text.

$$\begin{aligned}(w\zeta_1 + (1-w)\zeta_2) \pm \sqrt{w^2\left(\Delta\zeta_1^{(\mathrm{stat})}\right)^2 + (1-w)^2\left(\Delta\zeta_2^{(\mathrm{stat})}\right)^2} \\ \pm\left(w\Delta\zeta_1^{(\mathrm{syst})} + (1-w)\Delta\zeta_2^{(\mathrm{syst})}\right)\end{aligned} \tag{7.6}$$

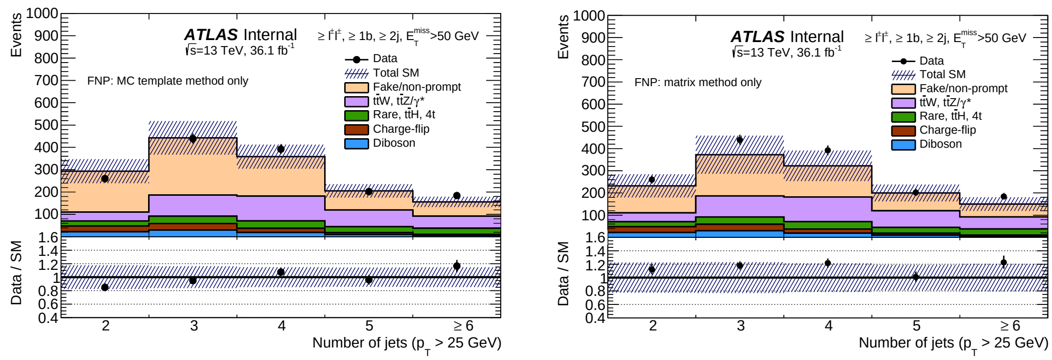

(a) (b)

Figure 7.21: Distributions of the number of jets after requiring at least two jets ($p_{\mathrm{T}} > 40$GeV) and $E_{\mathrm{T}}^{\mathrm{miss}} > 50$GeV, as well as at least two same-sign leptons. The fake or non-prompt leptons backgrounds are estimated alternatively with the MC template method (7.21b) or the matrix method (7.21a). The uncertainty band includes the statistical uncertainties for the background prediction as well as the full systematic uncertainties for fake or non-prompt leptons backgrounds or charge-flip electrons. The rare category is defined in the text. In both figures, the last bin contains the overflow.

$$\text{with } w = \frac{\left(\Delta\zeta_2^{(\text{stat})}\right)^2}{\left(\Delta\zeta_1^{(\text{stat})}\right)^2 + \left(\Delta\zeta_2^{(\text{stat})}\right)^2}$$

When the estimated value is too small(below 0.15), the expected yield is set to 0.15 ± 0.15, to cover for possibilities of an under-fluctuation of the number of baseline-not-signal leptons when applying the matrix method, as well as lack of statistics in the MC samples for the other method.

The charge flip background is not combined between the MC template method and the likelihood method due to the very large uncertainty in the MC template estimate. The OS data has a much larger number of events which makes a precise prediction of this background. The MC template result is used as a cross check.

Validation Region	$N_{\text{leptons}}^{\text{signal}}$	$N_{b\text{-jets}}$	N_{jets}	$p_{\text{T}}^{\text{jet}}$ [GeV]	$E_{\text{T}}^{\text{miss}}$ [GeV]	m_{eff} [GeV]	Other
$t\bar{t}W$	$= 2SS$	≥ 1	≥ 4 ($e^{\pm}e^{\pm}$, $e^{\pm}\mu^{\pm}$) ≥ 3 ($\mu^{\pm}\mu^{\pm}$)	> 40 > 25	> 45	> 550	$p_{\text{T}}^{\ell_2} > 40$ GeV $\sum p_{\text{T}}^{b\text{-jet}} / \sum p_{\text{T}}^{\text{jet}} > 0.25$
$t\bar{t}Z$	≥ 3 ≥ 1 SFOS pair	≥ 1	≥ 3	> 35	–	> 450	$81 < m_{\text{SFOS}} < 101$ GeV
WZ4j	$= 3$	$= 0$	≥ 4	> 25	–	> 450	$E_{\text{T}}^{\text{miss}} / \sum p_{\text{T}}^{\ell} < 0.7$
WZ5j	$= 3$	$= 0$	≥ 5	> 25	–	> 450	$E_{\text{T}}^{\text{miss}} / \sum p_{\text{T}}^{\ell} < 0.7$
$W^{\pm}W^{\pm}jj$	$= 2SS$	$= 0$	≥ 2	> 50	> 55	> 650	veto $81 < m_{e^{\pm}e^{\pm}} < 101$ GeV $p_{\text{T}}^{\ell_2} > 30$ GeV $\Delta R_{\eta}(\ell_{1,2}, j) > 0.7$ $\Delta R_{\eta}(\ell_1, \ell_2) > 1.3$
All VRs	Veto events belonging to any SR						

Table 7.1: Summary of the event selection in the validation regions (VRs). Requirements are placed on the number of signal leptons ($N_{\text{leptons}}^{\text{signal}}$), the number of b-jets with $p_{\text{T}} > 20$GeV ($N_{b\text{-jets}}$) or the number of jets (N_{jets}) above a certain p_{T} threshold ($p_{\text{T}}^{\text{jet}}$). The two leading-$p_{\text{T}}$ leptons are referred to as $\ell_{1,2}$ with decreasing p_{T}. Additional requirements are set on $E_{\text{T}}^{\text{miss}}$, m_{eff}, the invariant mass of the two leading electrons $m_{e^{\pm}e^{\pm}}$, the presence of SS leptons or a pair of same-flavour opposite-sign leptons (SFOS) and its invariant mass m_{SFOS}. A minimum angular separation between the leptons and the jets ($\Delta R_{\eta}(\ell_{1,2}, j)$) and between the two leptons ($\Delta R_{\eta}(\ell_1, \ell_2)$) is imposed in the $W^{\pm}W^{\pm}jj$ VR. For the two WZ VRs the selection also relies on the ratio of the $E_{\text{T}}^{\text{miss}}$ in the event to the sum of p_{T} of all signal leptons p_{T} ($E_{\text{T}}^{\text{miss}}/\sum p_{\text{T}}^{\ell}$). The ratio of the scalar sum of the p_{T} of all b-jets to that of all jets in the event ($\sum p_{\text{T}}^{b\text{-jet}} / \sum p_{\text{T}}^{\text{jet}}$) is used in the $t\bar{t}W$ VR selection.

Validation Region	$t\bar{t}W$	$t\bar{t}Z$	WZ4j	WZ5j	$W^{\pm}W^{\pm}jj$
$t\bar{t}Z/\gamma^*$	6.2 ± 0.9	123 ± 17	17.8 ± 3.5	10.1 ± 2.3	1.06 ± 0.22
$t\bar{t}W$	19.0 ± 2.9	1.71 ± 0.27	1.30 ± 0.32	0.45 ± 0.14	4.1 ± 0.8
$t\bar{t}H$	5.8 ± 1.2	3.6 ± 1.8	1.8 ± 0.6	0.96 ± 0.34	0.69 ± 0.14
$4t$	1.02 ± 0.22	0.27 ± 0.14	0.04 ± 0.02	0.03 ± 0.02	0.03 ± 0.02
$W^{\pm}W^{\pm}$	0.5 ± 0.4	–	–	–	26 ± 14
WZ	1.4 ± 0.8	29 ± 17	200 ± 110	70 ± 40	27 ± 14
ZZ	0.04 ± 0.03	5.5 ± 3.1	22 ± 12	9 ± 5	0.53 ± 0.30
Rare	2.2 ± 0.5	26 ± 13	7.3 ± 2.1	3.0 ± 1.0	1.8 ± 0.5
Fake/non-prompt leptons	18 ± 16	22 ± 14	49 ± 31	17 ± 12	13 ± 10
Charge-flip	3.4 ± 0.5	–	–	–	1.74 ± 0.22
Total SM background	57 ± 16	212 ± 35	300 ± 130	110 ± 50	77 ± 31
Observed	71	209	257	106	99

Table 7.2: The numbers of observed data and expected background events in the validation regions. The rare category is defined in the text. Background categories with yields shown as "–" do not contribute to a given region (e.g. charge flips in three-lepton regions) or their estimates are below 0.01 events. The displayed yields include all statistical and systematic uncertainties.

Table 7.3: Muon fake rate measured in data and the associated statistical uncertainty. The systematic uncertainty originating from the subtraction of "backgrounds" with only prompt leptons is also displayed.

$10 < p_{\mathrm{T}} < 12$ GeV		$12 < p_{\mathrm{T}} < 14$	
$\lvert\eta\rvert < 2.3$	$\lvert\eta\rvert > 2.3$	$\lvert\eta\rvert < 2.3$	$\lvert\eta\rvert > 2.3$
$0.14 \pm 0.01 \pm 0.00$	$0.22 \pm 0.05 \pm 0.00$	$0.11 \pm 0.01 \pm 0.00$	$0.24 \pm 0.06 \pm 0.00$
$14 < p_{\mathrm{T}} < 17$		$17 < p_{\mathrm{T}} < 20$ GeV	
$\lvert\eta\rvert < 2.3$	$\lvert\eta\rvert > 2.3$	$\lvert\eta\rvert < 2.3$	$\lvert\eta\rvert > 2.3$
$0.12 \pm 0.01 \pm 0.00$	$0.09 \pm 0.05 \pm 0.00$	$0.09 \pm 0.01 \pm 0.00$	$0.21 \pm 0.07 \pm 0.00$
$20 < p_{\mathrm{T}} < 30$	$30 < p_{\mathrm{T}} < 40$	$40 < p_{\mathrm{T}} < 60$	$p_{\mathrm{T}} > 60$
$0.07 \pm 0.02 \pm 0.00$	$0.12 \pm 0.05 \pm 0.01$	$0.16 \pm 0.09 \pm 0.04$	$0.49 \pm 0.10 \pm 0.07$

Table 7.4: Additional systematic uncertainty on the muon fake rates, to address variations of the latter in different environments. The table also shows the correction factors and uncertainties applied to final states with ≥ 2 b-tagged jets.

p_{T}	< 14	$14 - 20$	$20 - 30$	$30 - 40$	$40 - 60$	> 60
$\Delta\zeta^{(\mathrm{syst})}$	30%	30%	30%	50%	50% for $H_{\mathrm{T}} < 600$ 70% for $600 < H_{\mathrm{T}} < 1200$ 85% for $H_{\mathrm{T}} > 1200$	
$\frac{\zeta_{\geq 2b}}{\zeta}$	1.2 ± 0.2	1.5 ± 0.5	1.7 ± 0.7	2.0 ± 1.0	1.5 ± 0.5	–

Table 7.5: Electron fake rate measured in data and the associated statistical uncertainty. The systematic uncertainty originating from the subtraction of "backgrounds" with only prompt leptons is also displayed.

$10 < p_{\mathrm{T}} < 12$	$12 < p_{\mathrm{T}} < 14$	$14 < p_{\mathrm{T}} < 17$	$17 < p_{\mathrm{T}} < 20$
$0.10 \pm 0.01 \pm 0.00$	$0.10 \pm 0.01 \pm 0.01$	$0.12 \pm 0.01 \pm 0.01$	$0.08 \pm 0.02 \pm 0.00$
$20 < p_{\mathrm{T}} < 25$	$25 < p_{\mathrm{T}} < 30$	$30 < p_{\mathrm{T}} < 40$	$40 > p_{\mathrm{T}}$
$0.07 \pm 0.02 \pm 0.01$	$0.11 \pm 0.03 \pm 0.01$	$0.20 \pm 0.07 \pm 0.03$	$0.25 \pm 0.10 \pm 0.05$

	Electrons			Muons			
	$0 < \|\eta\| < 0.8$	$0.8 < \|\eta\| < 1.37$	$1.52 < \|\eta\| < 2.01$	$0 < \|\eta\| < 0.6$	$0.6 < \|\eta\| < 1.2$	$1.2 < \|\eta\| < 1.8$	$1.8 < \|\eta\| < 2.5$
10 GeV$< p_{\mathrm{T}} <$ 15 GeV	0.047	0.063	0.089	0.014	0.010	0.008	0.011
15 GeV$< p_{\mathrm{T}} <$ 20 GeV	0.027	0.042	0.062	0.005	0.006	0.008	0.011
20 GeV$< p_{\mathrm{T}} <$ 25 GeV	0.018	0.031	0.041	0.003	0.006	0.010	0.010
25 GeV$< p_{\mathrm{T}} <$ 30 GeV	0.029	0.024	0.027	0.011	0.015	0.022	0.019
30 GeV$< p_{\mathrm{T}} <$ 35 GeV	0.023	0.021	0.023	0.007	0.009	0.014	0.011
35 GeV$< p_{\mathrm{T}} <$ 40 GeV	0.014	0.018	0.018	0.004	0.004	0.006	0.006
40 GeV$< p_{\mathrm{T}} <$ 50 GeV	0.007	0.010	0.010	0.002	0.001	0.002	0.001
50 GeV$< p_{\mathrm{T}} <$ 60 GeV	0.008	0.010	0.010	0.001	0.001	0.001	0.001
60 GeV$< p_{\mathrm{T}} <$ 70 GeV	0.007	0.010	0.010	0.001	0.001	0.001	0.002
70 GeV$< p_{\mathrm{T}} <$ 80 GeV	0.008	0.011	0.012	0.002	0.001	0.001	0.002
80 GeV$< p_{\mathrm{T}} <$ 120 GeV	0.010	0.010	0.011	0.004	0.002	0.002	0.002
120 GeV$< p_{\mathrm{T}} <$ 150 GeV	0.005	0.005	0.011	0.006	0.005	0.005	0.005
150 GeV$< p_{\mathrm{T}} <$ 200 GeV	0.005	0.002	0.019	0.005	0.005	0.005	0.006

Table 7.6: Systematic uncertainties on the measured real lepton efficiency, separating sources affecting the measurement itself (background subtraction, trigger bias, and different methods).

electrons (busy environments)								
$\Delta R(e, jet)$	[0, 0.1]	[0.1, 0.15]	[0.15, 0.2]	[0.2, 0.3]	[0.3, 0.35]	[0.35, 0.4]	[0.4, 0.6]	[0.6, 4]
10 GeV< p_{T} < 20 GeV	-	-	-	-	-	-	25.31%	6.5%
20 GeV< p_{T} < 30 GeV	-	-	-	-	-	73.37%	10.21%	0.37%
30 GeV< p_{T} < 40 GeV	-	-	-	97.71%	48.22%	15.54%	7.29%	0.58%
40 GeV< p_{T} < 50 GeV	-	-	-	52.81%	22.80%	16.73%	7.68%	1.10%
50 GeV< p_{T} < 60 GeV	-	-	-	29.96%	21.49%	20.23%	6.99%	2.78%
60 GeV< p_{T} < 80 GeV	-	-	55.89%	24.31%	17.40%	24.77%	6.20%	2.87%
80 GeV< p_{T} < 150 GeV	-	57.52%	30.24%	16.45%	12.73%	20.92%	4.44%	2.73%
150 GeV< p_{T} < 200 GeV	88.54%	40.16%	19.34%	8.45%	14.66%	16.57%	2.57%	1.90%
muons (busy environments)								
$\Delta R(\mu, jet)$	[0, 0.1]	[0.1, 0.15]	[0.15, 0.2]	[0.2, 0.3]	[0.3, 0.35]	[0.35, 0.4]	[0.4, 0.6]	[0.6, 4]
10 GeV< p_{T} < 20 GeV	-	-	-	-	-	-	33.59%	5.18%
20 GeV< p_{T} < 30 GeV	-	-	-	-	-	82.34%	22.27%	3.39%
30 GeV< p_{T} < 40 GeV	-	-	-	98.54%	56.36%	31.89%	14.22%	2.24%
40 GeV< p_{T} < 50 GeV	-	-	-	53.10%	21.33%	13.90%	6.81%	1.45%
50 GeV< p_{T} < 60 GeV	-	-	-	24.98%	13.72%	9.62%	3.83%	0.79%
60 GeV< p_{T} < 80 GeV	-	-	44.41%	13.75%	6.14%	4.76%	2.04%	0.15%
80 GeV< p_{T} < 150 GeV	-	29.94%	7.14%	3.16%	1.30%	1.04%	0.07%	0.57%
150 GeV< p_{T} < 200 GeV	82.26%	4.14%	1.02%	0.17%	0.29%	0.62%	1.02%	1.13%

Table 7.7: Systematic uncertainties on the measured real lepton efficiency, due to the extrapolation to busy environments using $\tilde{g} \to t\bar{t}\tilde{\chi}_1^0$ events.

Table 7.8: Expected yields for background processes with fake leptons, in the signal regions with a global correction factor that represents the ratio of weighted $t\bar{t}$ to raw MC $t\bar{t}$ with a global uncertainty that includes: fit uncertainty, theory uncertainties on ttbar, comparison of different showers. The fraction of the systematic uncertainty from the comparison between two showers (Pythia and Sherpa) is also shown.

Region	MC Template method	Global correction	Shower systematic
Rpc2L0bH	$1.00 \pm 0.96 \pm 0.81$	2.80 ± 2.10	74%
Rpc2L0bS	$1.68 \pm 1.02 \pm 1.26$	2.89 ± 1.97	65%
Rpc2L1bH	$2.07 \pm 0.63 \pm 1.56$	1.22 ± 1.14	34%
Rpc2L1bS	$2.33 \pm 1.17 \pm 2.10$	1.83 ± 1.42	81%
Rpc2L2bH	< 0.5	0 ± 0	0%
Rpc2L2bS	$0.41 \pm 0.33 \pm 0.45$	1.47 ± 1.12	73%
Rpc2Lsoft1b	$2.48 \pm 1.32 \pm 1.86$	1.59 ± 1.31	68%
Rpc2Lsoft2b	$1.66 \pm 0.66 \pm 1.28$	1.72 ± 1.29	54%
Rpc3L0bH	< 0.5	0 ± 0	0%
Rpc3L0bS	$0.21 \pm 0.15 \pm 0.16$	2.90 ± 2.20	71%
Rpc3L1bH	$0.42 \pm 0.29 \pm 0.32$	1.59 ± 1.25	59%
Rpc3L1bS	$3.55 \pm 1.80 \pm 2.76$	1.76 ± 1.32	67%
Rpc3LSS1b	$0.90 \pm 0.14 \pm 0.69$	2.34 ± 1.44	56%

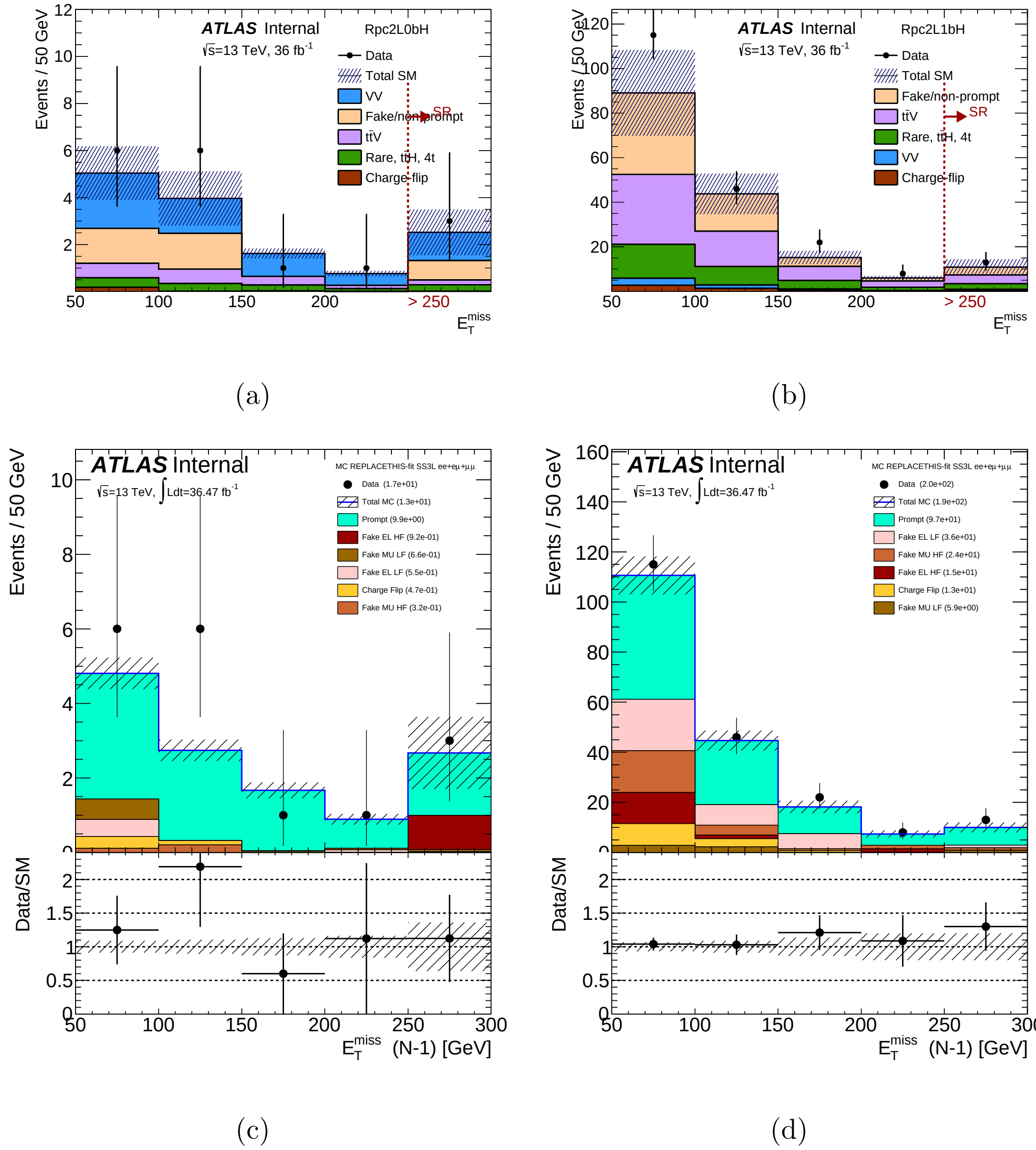

(a) (b) (c) (d)

Figure 7.22: Missing transverse momentum distributions after (7.22a–7.22c) Rpc2L0bH and (7.22b–7.22d) Rpc2L1bH selection, except the $E_{\mathrm{T}}^{\mathrm{miss}}$ requirement. Estimates with the matrix method are in the upper plots (7.22a–7.22a) while estimates with the MC tempalte method are in the lower plots (7.22c–7.22c). The results in the signal regions are shown in the last (inclusive) bin of each plot. The statistical uncertainties in the background prediction are included in the uncertainty band, as well as the full systematic uncertainties for backgrounds with fake or non-prompt leptons, or charge-flip.

Table 7.9: Expected yields for background processes with fake leptons, in the signal regions shown for 36 fb^{-1}. Estiamtes from the matrix method and the MC template method are shown along with the retained estimates. Uncertainties include all statistical and systematic sources for the nominal estimate.

Region	Matrix method	Template method	Retained estimate
Rpc2L0bH	$0.83 \pm 0.56 \pm 0.74$	$1.00 \pm 0.96 \pm 0.81$	$0.87 \pm 0.48 \pm 0.76$
Rpc2L0bS	$1.51 \pm 0.60 \pm 0.66$	$1.68 \pm 1.02 \pm 1.26$	$1.55 \pm 0.52 \pm 0.81$
Rpc2L1bH	$3.54 \pm 1.62 \pm 3.12$	$2.07 \pm 0.63 \pm 1.56$	$2.26 \pm 0.59 \pm 1.76$
Rpc2L1bS	$2.65 \pm 1.21 \pm 1.89$	$02.33 \pm 01.17 \pm 02.10$	$2.48 \pm 0.84 \pm 2.00$
Rpc2L2bH	$-0.11 \pm 0.11 \pm 0.18$	< 0.5	$0.15 \pm 0.15 \pm 0.00$
Rpc2L2bS	$1.31 \pm 1.07 \pm 1.65$	$0.41 \pm 0.33 \pm 0.45$	$0.49 \pm 0.32 \pm 0.55$
Rpc2Lsoft1b	$4.75 \pm 1.42 \pm 2.64$	$2.48 \pm 1.32 \pm 1.86$	$3.53 \pm 0.97 \pm 2.22$
Rpc2Lsoft2b	$1.91 \pm 1.18 \pm 1.63$	$1.66 \pm 0.66 \pm 1.28$	$1.72 \pm 0.58 \pm 1.36$
Rpc3L0bH	$-0.01 \pm 0.11 \pm 0.10$	< 0.5	$0.15 \pm 0.15 \pm 0.00$
Rpc3L0bS	$2.31 \pm 1.50 \pm 2.63$	$0.21 \pm 0.15 \pm 0.16$	$0.23 \pm 0.15 \pm 0.18$
Rpc3L1bH	$0.57 \pm 0.43 \pm 0.50$	$0.42 \pm 0.29 \pm 0.32$	$0.47 \pm 0.24 \pm 0.38$
Rpc3L1bS	$4.94 \pm 1.83 \pm 2.96$	$3.55 \pm 1.80 \pm 2.76$	$4.23 \pm 1.28 \pm 2.86$
Rpc3LSS1b	$-0.18 \pm 1.24 \pm 2.85$	$0.90 \pm 0.14 \pm 0.69$	$0.89 \pm 0.14 \pm 0.72$

Table 7.10: Expected yields for background processes with charge-flipped electrons, in the signal regions shown for 36 fb^{-1}. Estiamtes from the likelihood method and the MC template method are shown. Uncertainties include all statistical and systematic sources. Charge-flip processes do not contribute to signal regions which require ≥ 3 leptons.

Region	Weighted OS data	Template method
Rpc2L0bH	$0.01 \pm 0.00 \pm 0.00$	< 0.4
Rpc2L0bS	$0.05 \pm 0.01 \pm 0.01$	$00.02 \pm 00.02 \pm 00.00$
Rpc2L1bH	$0.25 \pm 0.03 \pm 0.04$	$00.21 \pm 00.32 \pm 00.16$
Rpc2L1bS	$0.25 \pm 0.02 \pm 0.04$	$00.35 \pm 00.37 \pm 00.26$
Rpc2L2bH	$0.02 \pm 0.01 \pm 0.00$	< 0.4
Rpc2L2bS	$0.10 \pm 0.01 \pm 0.02$	< 0.4
Rpc2Lsoft1b	$0.08 \pm 0.01 \pm 0.02$	< 0.4
Rpc2Lsoft2b	$0.08 \pm 0.01 \pm 0.02$	< 0.4
Rpc3LSS1b	$0.39 \pm 0.03 \pm 0.07$	$00.81 \pm 00.53 \pm 00.34$

Table 7.11: Comparison of expected yields for background processes with fake leptons, in the validation regions, shown for 36 fb^{-1} between the data driven (DD) estimates and the MC template method (MC) estimates.

	VR-$t\bar{t}W$	VR-$t\bar{t}Z$	VR-WZ4j	VR-WZ5j	VR-$W^{\pm}W^{\pm}$
Fakes DD	$23 \pm 5 \pm 24$	$30 \pm 4 \pm 14$	$53 \pm 6 \pm 27$	$21 \pm 4 \pm 10$	$14 \pm 3 \pm 10$
Fakes MC	$14 \pm 4 \pm 10$	$18 \pm 3 \pm 13$	$46 \pm 5 \pm 34$	$16 \pm 2 \pm 12$	$13 \pm 2 \pm 10$
Combined	$18 \pm 3 \pm 15$	$22 \pm 2 \pm 13$	$49 \pm 4 \pm 30$	$17 \pm 2 \pm 12$	$13 \pm 2 \pm 10$
Charge-flip DD	$3.4 \pm 0.1 \pm 0.5$	–	–	–	$1.7 \pm 0.1 \pm 0.2$
Charge-flip MC	$3.8 \pm 1.0 \pm 1.9$	–	–	–	$1.0 \pm 0.3 \pm 0.2$

Chapter 8

Systematic uncertainties

The systematic uncertainties related to the estimated background from same-sign prompt leptons arise from the experimental uncertainties as well as theoretical modelling and theoretical cross-section uncertainties. The statistical uncertainty of the simulated event samples is also taken into account.

8.1 Theretical Uncertainties

The cross-sections used to normalize the MC samples are varied according to the uncertainty in the cross-section calculation, which is 13% for $t\bar{t}W$, 12% for $t\bar{t}Z$ production [15], 6% for diboson production [17], 8% for $t\bar{t}H$ [15] and 30% for $4t$ [11]. Additional uncertainties are assigned to some of these backgrounds to account for the theoretical modelling of the kinematic distributions in the MC simulation.

Associate $t\bar{t} + W/Z$ production

The theoretical uncertainties on the ttW and $ttZ^{(*)}$ processes are evaluated by several variations added in quadrature:

- Normalization and factorization scales varied independently up and down by a factor of two from the central scale $\mu_0 = H_{\mathrm{T}}/2$ as detailed in Ref. [27]. The largest deviation with respect to the nominal is used as the symmetric uncertainty.

- Variation of the PDF used. The standard deviation of the yields obtained using different PDF sets was used as the absolute uncertainty due to PDF. The relative uncertainty is then computed by dividing the standard deviation by the mean yield.

- Comparison of the nominal aMC@NLO MC samples to alternative Sherpa (v2.2) samples produced at leading-order with one extra parton in the matrix element for ttW and 2 extra partons for ttZ [27]. The yield comparison for all SRs is shown in Table 8.1, with negligible differences in some SRs and up to 28% in the worst case.

As a result of these studies, the total theory uncertainty for these processes is at the level of 15-35% in the signal and validation regions used in the analysis.

Diboson $WZ, ZZ, W^{\pm}W^{\pm}$ production

The theoretical uncertainties on the WZ and ZZ processes are evaluated by several variations added in quadrature:

- Normalization and factorization scales varied independently up and down by a factor of two from the central scale choice. The largest deviation with respect to the nominal is used as the symmetric uncertainty.

- The standard deviation of the yields obtained using different PDF sets was used as the absolute uncertainty due to PDF. The relative uncertainty is then computed by dividing the standard deviation by the mean yield.

Table 8.1: Comparison of the event yields for the $t\bar{t}V$ backgrund processes between aMC@NLO (default generator) and Sherpa in the SRs, as well as their relative difference.

SR	Sherpa	aMCATNLO	Relative diff.
Rpc2L0bH	0.25 ± 0.03	0.20 ± 0.05	25%
Rpc2L0bS	0.60 ± 0.06	0.82 ± 0.10	-26%
Rpc2L1bH	3.84 ± 0.14	3.86 ± 0.20	<1%
Rpc2L1bS	3.55 ± 0.13	3.94 ± 0.20	-9%
Rpc2L2bH	0.35 ± 0.04	0.41 ± 0.05	-14%
Rpc2L2bS	1.57 ± 0.08	1.57 ± 0.12	<1%
Rpc2Lsoft1b	1.01 ± 0.07	1.24 ± 0.11	-18%
Rpc2Lsoft2b	1.13 ± 0.07	1.15 ± 0.10	-1%
Rpc3L0bH	0.23 ± 0.02	0.18 ± 0.04	27%
Rpc3L0bS	0.90 ± 0.05	0.99 ± 0.09	-9%
Rpc3L1bH	1.54 ± 0.08	1.52 ± 0.11	1%
Rpc3L1bS	6.95 ± 0.16	7.02 ± 0.23	<1%
Rpc3LSS1b	0.00 ± 0.00	0.00 ± 0.00	-

- Resummation scale varied up and down by a factor of two from the nominal value.
- The scale for calculating the overlap between jets from the matrix element and the parton shower is varied from the nominal value of 20 GeV down to 15 GeV and up to 30 GeV. The largest deviation with respect to the nominal is used as the symmetric uncertainty due to matrix element matching.

- An alternative recoil scheme is considered to estimate the uncertainty associated with mismodeling of jet multiplicities larger than three.

Based on these studies and the cross-section uncertainties, the total theory uncertainty for these processes is at the level of 25-40% in the signal and validation regions used in the analysis.

No theoretical uncertainties have been evaluated specifically for the $W^{\pm}W^{\pm}jj$ process, to which we assign the same uncertainties as for WZ, by lack of a better choice. But it should be noted that contributions from this process are minor in the SRs and typically smaller than those from WZ and ZZ.

Other rare processes

A conservative 50% uncertainty is assigned on the summed contributions of all these processes ($t\bar{t}H$, tZ, tWZ, $t\bar{t}t\bar{t}$, $t\bar{t}WW$, $t\bar{t}WZ$, WH, ZH, VVV), which is generally quite larger than the uncertainties on their inclusive production cross-sections, and assumes a similar level of mismodelling as for diboson or $t\bar{t}V$ processes.

8.2 Experimental Uncertainties

Uncertainties associated with the measurement and reconstruction of the physics objects used in the analysis (leptons, jets, etc.) must be accounted for when interpretting the results. The systematic uncertainties from the data-driven method have already been discussed in Section 7.3. In fact, these data-driven backgrounds are affected by the same systematic uncertainty as in data to which they are being compared to. As a result, only systematic uncertainties on backgrounds estimated with MC simulation and detector simulation needs to be considered. The uncertainties considered for the analysis and recommended by the ATLAS SUSY group are:

Jet energy scale (JES)

In order to account for ineffciencies in the calorimeter cells and the varying response to charged and neutral particles passing through them, the energies of the jets used in this analysis were corrected. The calibaration procedure uses a combination of simulation and test beam and in situ data [??] with an uncertainty correlated between all events. As a result, all distributions used in the final result are produced with the nominal calibration as well as an up and down variation of the the jet energy scale (in a fully correlated way) by the $\pm 1\sigma$ uncertainty of each nuisance parameter. A combined version of several independent sources contributing to the calibration was used in the analysis to reduce the number of nuisance variables in the fitting procedure.

Jet energy resolution (JER)

An extra p_{T} smearing is added to the jets based on their p_{T} and η to account for a possible underestimate of the jet energy resolution in the MC simulation. A systematic uncertainty is considered to account for this defect on the final result. The JER in data has previously been estimated by ATLAS in dijet events [??].

Jet vertex tagger The uncertainties account for the residual contamination from pile-up jets after pile-up suppression and the MC generator choice.

Flavor tagging The MC simulation does not reproduce correctly the b-tagging

, charm identification, and light jet reject effeciencies of the detector. A $t\bar{t}$ MC simulation and di–jet measurements are used to derive correction factors to be applied to MC simulation [??]. These correction factors are then varied within their uncertainties to produce up and down variations.

Lepton energy scale, resolution, and Identification efficiencies Similar to the case of jets, electrons and muons have also corresponding energy scale and resolution systematic uncertainties. Corrections are also applied to take into account any variations in the identification efficiency in the detector and its simulation [??].

$\boldsymbol{E_{\mathrm{T}}^{\mathrm{miss}}}$ **soft term uncertainties** The main effect come from the hard object uncertainties (most notably JES and JER) that are propagated to the $E_{\mathrm{T}}^{\mathrm{miss}}$.

Pileup reweighting This uncertainty is obtained by re-scaling the μ value in data by 1.00 and 1/1.18, covering the full difference between applying and not-applying the nominal μ correction of 1/1.09, as well as effects resulting from uncertainties on the luminosity measurements, which are expected to dominate.

Luminosity The integrated luminosities in data corresponds to 3.2 $\mathrm{fb}^{-1}$and 32.9 $\mathrm{fb}^{-1}$for 2015 and 2016 respectively. The combined luminosity error for 2015 and 2016 is 3.2%, assuming partially correlated uncertainties in 2015 and 2016.

Trigger To account for any differences between the trigger efficiency in simulation and data, corrections factors are derived to correct for them. Uncertainties on the correction factors as well as inefficiencies related to the plateau of the trigger are propagated to the final result.

The uncertainty on the beam energy is neglected. All the experimental uncertainties are applied also on the signal samples when computing exclusion limits on SUSY scenarios.

All of these uncertainties are fed into the fitting and limit setting machinery by treating them as uncorrelated uncertainties, and thus treated independently.

Chapter 9

Statistical Treatment

The goal of the analysis is to maximize the information that can be extracted from comparing the observed data to the background prediction in the signal regions designed to search for new physics topologies. Statistical tools are essential to tell in the most powerful way and to the best of our knowledge if there is a new physics signal beyond what is already known in the observed data. At the same time, it is important to properly treat the systematic uncertainties associated with the complexity of the experimental apparatus (ATLAS detector) and the background predictions when presenting an interpretation of the results. This chapter describes the statistical methodology employed to test the compatibility between data and prediction while taking into account the systematic uncertainties. The analysis' possible outcomes are represented by a likelihood function that combines observations, predictions, and associated uncertainties (Section??). At which point the hypothesis testing is performed with the corresponding one-sided profile likelihood ratio [53], and upper limits are provided as one-sided 95% confidence level intervals in the $\mathrm{CL_s}$ formalism [54] (Section??). The statistical tool used to perform the quantification of the significance of hypothetical excesses seen in data or upper limits setting on new physics contributions is the `HistFitter` framework [55] which was developed by ATLAS.

9.1 Likelihood Function

The likelihood for a set of parameters $(\mu, \boldsymbol{\theta})$ given all the data that might have been observed $\boldsymbol{X}$ is the probability of observing the data given the parameters

$$\mathcal{L}(\mu, \boldsymbol{\theta}|\boldsymbol{X}) = \Pr(\boldsymbol{X}|\mu, \boldsymbol{\theta}) \, . \tag{9.1}$$

The data $\boldsymbol{X}$ includes observation in the signal regions as well as other auxilary experiments such as control regions used to constain backgrounds. In this analysis, hypothesis tests are performed on one signal region at the time, single-binned, and without control regions. As a result, the observed data $\boldsymbol{X}$ has one-dimensional component with value X representing the count of events in the signal region. The first parameter of interest represents the 'strength' of the signal process $\mu > 0$ that will increase the number of expected events in the signal region given that the signal of the new physics model tested is present. In practice, the signal strength μ is used to scale the nominal expected cross section for the signal process, or the number of expected signal events s. Thus, the predicted background will be of the form $\mu s + \sum_i b_i$ where b_i represents the standard model background processes expected to contribute to the signal region. The parameter $\boldsymbol{\theta}$ refers to the nuisance parameters used to parametrize the systematic uncertainties (luminosity, JES, JER, etc.) [1]. Thus, the likelihood is built as the product of a Poisson probability density function describing the observed number of events in the signal region and Gaussian distributions for each of the sources of systematic uncertainties. The

[1] The parameters represented by $\boldsymbol{\theta}$ are called nuisance parameters since the aim is not to set a limit on them.

likelihood takes the simple form

$$\Pr\left(X, \boldsymbol{\theta^0} | \mu, \boldsymbol{\theta}\right) = \mathcal{P}\left(X \mid \mu s\left(\boldsymbol{\theta}\right) + \sum_i b_i\left(\boldsymbol{\theta}\right)\right) \times \prod_j \mathcal{G}\left(\theta^0 | \theta_j\right) \tag{9.2}$$

where $\mathcal{P}\left(X \mid \nu\right) = e^{-\nu}\nu^X / X!$ and $\mathcal{G}\left(\theta\right) = \frac{1}{\sqrt{2\pi\sigma_\theta^2}} e^{-\frac{\left(\theta-\theta^0\right)^2}{2\sigma_\theta^2}}$ are the Poisson and Gaussian probablity density functions. Both signal and backgrounds depend on the nuisance parameter $\boldsymbol{\theta}$ which controls all independent sources of uncertainty and will be *profiled* (or constrained) in the CL_s procedure described next. Correlations of a given nuisance parameter between the different sources of backgrounds and the signal are taken into account when relevant. To give an example, the luminosity uncertainty will have a mean as the luminosity central value $\theta^{(0)}_{\mathrm{lumi}}$ and the width as an experimentally determined uncertainty $\sigma_{\theta_{\mathrm{lumi}}}$. When evaluating the effect of the luminosity uncertainty on the likelihood function, all terms involving the nuisance parameter θ_{lumi} will be scaled in the same way since luminosity is correlated across all backgrounds and signal.

The likelihood function described in this section is used in a fit to data by the maximum likelihood method that aims at finding the value of the signal strenght μ that makes the likelihood a maximum. The procedure relies on an iterative minimization algorithm implemented in Minuit ??] and accessed by *RooFit* ??]. The final uncertainties on the nuisance parameters in $\boldsymbol{\theta}$, constrained by the fit, are obtained from the covariance matrix of these parameters.

9.2 Limit Setting Procedure

The procedure for setting exclusion limits using the likelihood function (Eq. ??) relies on a profile-likelihood-ratio test [53]. The null hypothesis considered is that of background only with $\mu = 0$ and the alternate hypothesis is the presence of a signal with strength $\mu > 0$. According to the Neyman-Pearson Lemma CITE??, the most powerful test when performing a hypothesis test between two simple hypotheses, $\mu = 0$ and $\mu > 0$, is the profile-likelihood-ratio test, which rejects $\mu = 0$ in favor of $\mu > 0$. The profile-likelihood-ratio test q_μ is defined to be

$$q_\mu\left(\boldsymbol{X}\right) = \begin{cases} -2\ln\left(\frac{\mathcal{L}\left(\mu,\hat{\hat{\boldsymbol{\theta}}}(\mu)|\boldsymbol{X}\right)}{\mathcal{L}\left(\hat{\mu},\hat{\boldsymbol{\theta}}|\boldsymbol{X}\right)}\right), & \text{if } \mu > \hat{\mu} \\ 0, & \text{otherwise} \end{cases} \tag{9.3}$$

For a given observation $\boldsymbol{X}$, the parameters $\hat{\mu}$ and $\boldsymbol{\theta}$ are obtained from maximizing the likelihood. If the value of μ is also fixed, the set of values $\hat{\hat{\boldsymbol{\theta}}}$ corresponds to the set of values that maximize the likelihood for that particular value of μ. The variable q_μ is always positive ($q_\mu \geq 0$). Qualitatively, small values of q_μ correspond to a better compatibility between the observed data and the tested hypothesis with a signal strenght μ, while large values indicate a very improbable signal hypothesis. The condition on the sign of $\mu - \hat{\mu}$ is necessary in order not to interpret an upward fluctuation of data ($X > \mu s + b$) as incompatibe with the tested hypothesis. The form of q_μ is motivated by Wald and Wilk's CITE?? approximation formulas in the large sample limit where the distributions of q_μ also become independent of nuisance parameters as it will be discussed next. The test statistic for discovery will try to reject the background only hypothesis ($\mu = 0$).

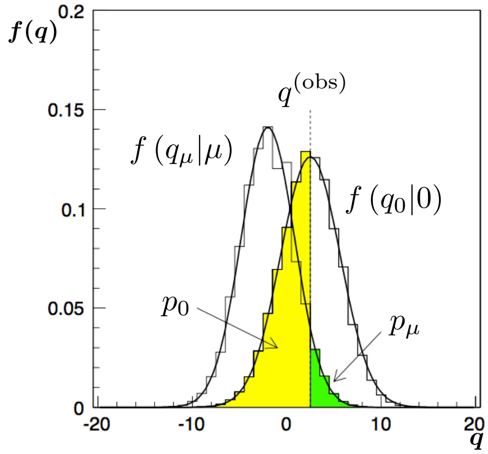

(a)

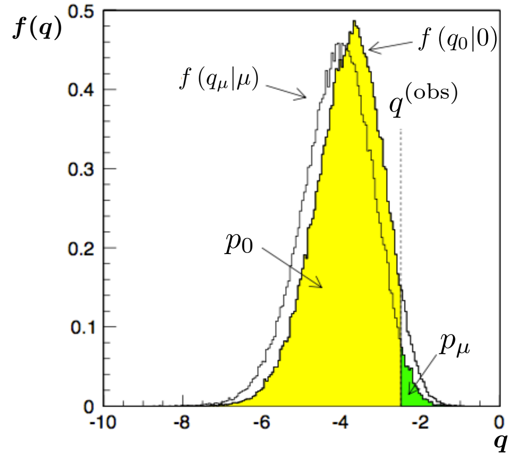

(b)

Figure 9.1: Distributions of the test variable q_μ under the $\mu > 0$ and $\mu = 0$ hypotheses: (a) typical case, (b) case where there is very little sensitivity to the signal model

Thus Eq.9.3 becomes

$$q_0(\boldsymbol{X}) = \begin{cases} -2\ln\left(\frac{\mathcal{L}\left(0,\hat{\hat{\boldsymbol{\theta}}}(0)|\boldsymbol{X}\right)}{\mathcal{L}\left(\hat{\mu},\hat{\boldsymbol{\theta}}|\boldsymbol{X}\right)}\right), & \text{if } \hat{\mu} < 0 \\ 0, & \text{otherwise} \end{cases} \tag{9.4}$$

At this stage, a test statistic q_μ has been constructed to distinguish between the hypothesis that the data contains signal and background $\mu > 0$ and that of background only $\mu = 0$. To illustrate the limit setting procedure, we consider distributions of the test statistic under each hypothesis: $f(q_\mu|\mu)$ for $\mu > 0$ and $f(q_0|0)$ for $\mu = 0$. These distributions are shown in Figure 9.1a and details on how to obtain their functional forms will be discussed later.

Given that the actual observed data leads to a test variable $q_\mu^{(\mathrm{obs})}$, it is possible to quantify the level of discrepancy between the observed data and the tested hypothesis ($\mu > 0$ or $\mu = 0$) using a p-value. The p-value of the signal hypothesis

($\mu > 0$) is then defined as the probability, under assumption of the signal hypothesis, to find a value of q_μ with equal or lesser compatibility with the signal model considered relative to what is found with $q_\mu^{(\mathrm{obs})}$. In other words, higher values of q_μ indicate an increasing disagreement between data and the signal model. The mathematical expression of the p-value with $\mu > 0$ is taken as the probablity to find q_μ greater than or equal $q_\mu^{(\mathrm{obs})}$, under the signal hypothesis[2] is given by

$$p_\mu = \Pr\left(q_\mu \geq q_\mu^{(\mathrm{obs})}|\mu\right) = \int_{q_\mu^{(\mathrm{obs})}}^{\infty} f\left(q_\mu|\mu\right) \mathrm{d}q_\mu \tag{9.5}$$

where $q_\mu^{(\mathrm{obs})}$ is the value of the statistic test observed in data and the function f denotes the probability distribution function of q_μ under the signal hypothesis. Similarly, the p-value of the background-only hypothesis with $\mu = 0$ takes the form of

$$p_0 = \Pr\left(q_0 \geq q_0^{(\mathrm{obs})}|0\right) = \int_{-\infty}^{q_0^{(\mathrm{obs})}} f\left(q_0|0\right) \mathrm{d}q_0 \tag{9.6}$$

and can be interpretted as the probability of the observation to be consistent with the background only hypothesis: the smaller the p_0 value is, the less compatible data is with the background only hypothesis.

The next step is to define a confidence interval (CI) that includes the parameter μ at a specified confidence level (CL). In other words, instead of estimating the parameter μ by a single value, an interval CI likely to include the parameter is given. The CL provides a quantitative statement on how likely the interval CI is to contain the parameter μ. If given the measurement of a parameter μ_{meas}, we deduce that there is a 95% CI $[\mu_1, \mu_2]$ means that in an ensemble of experiments

[2]Note that the background-only distribution $f\left(q_0|0\right)$ in the example given in Figure 9.1a is shifted to the right.

95% of the obtained CIs will contain the true value of μ. The upper limit is simply the case where the 95% CI is $[0, \mu_{up}]$: In an ensemble of experiments 95% of the obtained CIs will contain the true value of μ, including $\mu = 0$. The conclusion is that $\mu < \mu_{up}$ at the 95% CL or that μ_{up} is an upper limit.

Applying this concept to the problem at hand where we want to place an upper limit on the expected number of signal events S ($S = \mu s$, s being the expected number of signal events for $\mu = 1$) in one or more signal regions. The CL is obtained from a standard statistical test of the signal model ($\mu > 0$) which can establish the exclusion of the signal model at confidence level $1 - \alpha = 95\%$ if

$$CL_{\mathrm{s+b}} = p_{\mu} < \alpha \tag{9.7}$$

where $\alpha = 0.05$. Since the result section will present CL values in terms of the expected number of signal events from beyond the standard model processes, we continue this discussion of estimating an upper limit on S rather than μ. Thus, a CI at confidence level $CL = 1 - \alpha$ for the expected number of signal events S can be constructed from those values of S (or μ) that are not excluded, and the upper limit $S_{up}^{1-\alpha}$ is the largest value of S not excluded. By construction, the interval $[0, S_{up}^{95}]$ will cover the expected number of signal events S with a probability of at least 95%, regardless of the value of S.

An anomaly arises with the $CL_{\mathrm{s+b}}$ prescription when the number of expected signal events is much less than that of the background and the data observation had a downward fluctuation below the expected background. The procedure will lead to excluding, with probability close to α, hypotheses to which the experiment has no sensitivity. For $\alpha = 5\%$, it means that one out of twenty tests for different signal models where one has no sensitivity will result in exclusion. In fact, the desired behavior of the exclusion probability in this case is to approach zero rather than α. This scenario is illustrated in Figure 9.1b where the distribution of q_μ under both the signal and background-only hypotheses are almost similar. To remedy this problem, a different procedure is used where a model is regarded as excluded if

$$CL_{\mathrm{s}} = \frac{p_\mu}{1 - p_0} < \alpha. \tag{9.8}$$

In this form, the p-value is penalized by dividing by $1 - p_0$. If the distribution of q_μ under signal or background-only hypotheses are widely seperated, then the quantity $1 - p_0$ is close to unity which recovers the $CL_{\mathrm{s+b}}$ value. However, if the distributions of both hypotheses are similar, due to the lack of sensitivity, $1 - p_0$ becomes smaller and the $CL_{\mathrm{s+b}}$ value is increased more leading to a weaker upper limit. Similar to the case of $CL_{\mathrm{s+b}}$, the upper limit on S^{95}_{up} is taken as the largest value of the parameter S not excluded.

9.3 Model Exclusion

The remaining task is to determine the distributions $f\left(q_\mu|\mu\right)$ for $\mu > 0$ and $f\left(q_0|0\right)$ for $\mu = 0$ needed to compute the p-values.

$$q_\mu = \begin{cases} \frac{(\mu-\hat{\mu})^2}{\sigma^2} + \mathcal{O}\left(\frac{1}{\sqrt{N}}\right), & \text{if } \mu > \hat{\mu} \\ 0, & \text{otherwise} \end{cases} \tag{9.9}$$

Chapter 10

Results and Interpretation

Chapter 11

Conclusions

Appendix A

Auxiliary material

Appendix B

Validation of background estimates

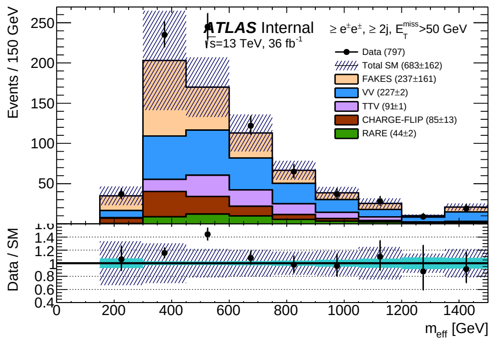

(a) Effective mass m_{eff}

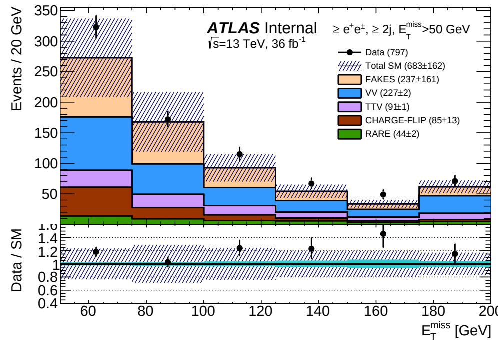

(b) Missing transverse momentum $E_{\mathrm{T}}^{\mathrm{miss}}$

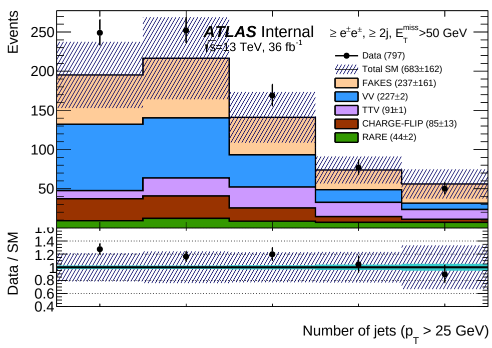

(c) Number of jets ($p_{\mathrm{T}} > 25$ GeV)

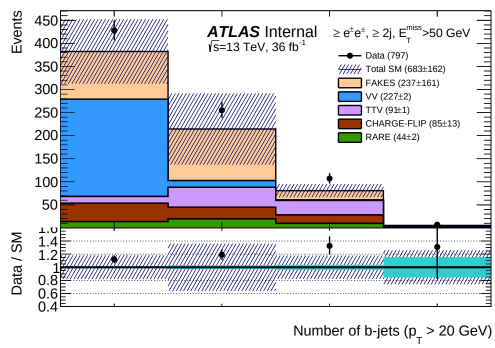

(d) Number of b-tagged jets ($p_{\mathrm{T}} > 20$ GeV)

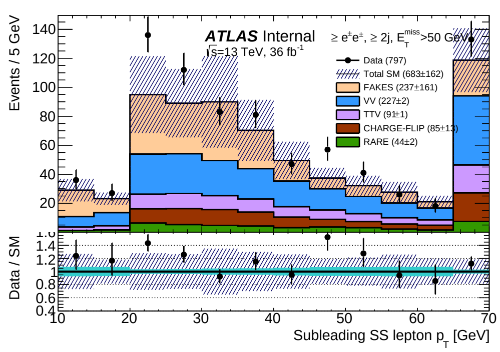

(e) Subleading SS lepton p_{T}

Figure B.1: Dielectron channel: comparisons between observed data (2015+2016, 36 fb^{-1}) and expected SM+detector backgrounds for events with ≥ 2 same-sign leptons ($p_{\mathrm{T}} > 20$ GeV), $E_{\mathrm{T}}^{\mathrm{miss}} > 50$ GeV and ≥ 2 jets ($p_{\mathrm{T}} > 40$ GeV). Uncertainties include statistical sources, as well as systematic uncertainties for the data-driven backgrounds; for illustration, statistical uncertainties alone are shown in the light-coloured error bands in the ratio plots. Events belonging to any of the signal regions are rejected, both in data and MC.

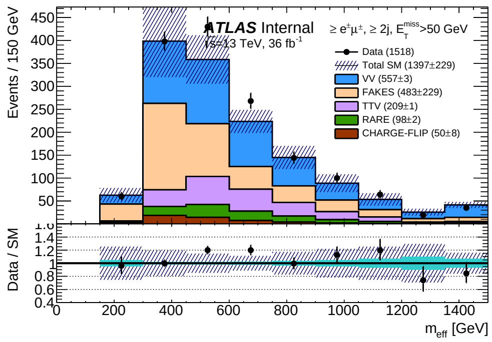

(a) Effective mass m_{eff}

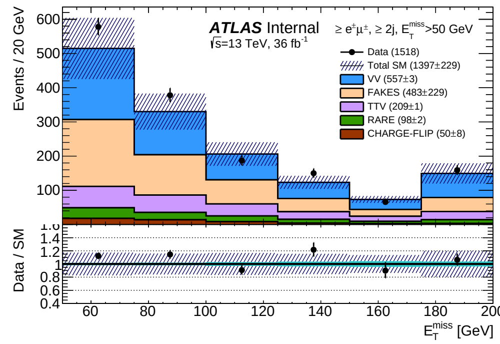

(b) Missing transverse momentum $E_{\mathrm{T}}^{\mathrm{miss}}$

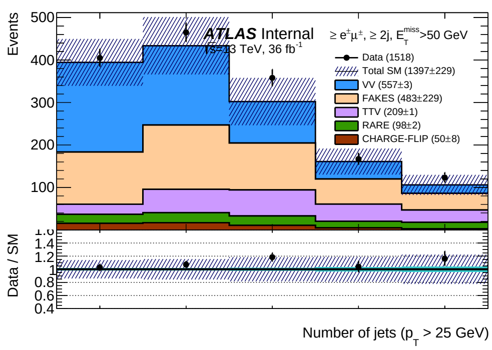

(c) Number of jets ($p_{\mathrm{T}} > 25$ GeV)

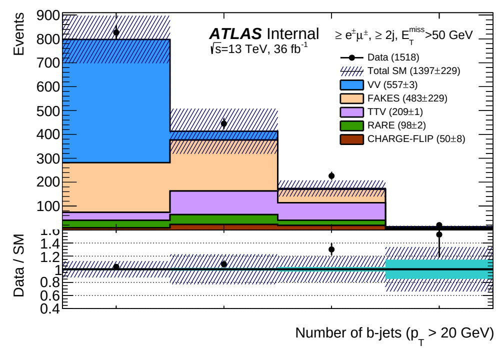

(d) Number of b-tagged jets ($p_{\mathrm{T}} > 20$ GeV)

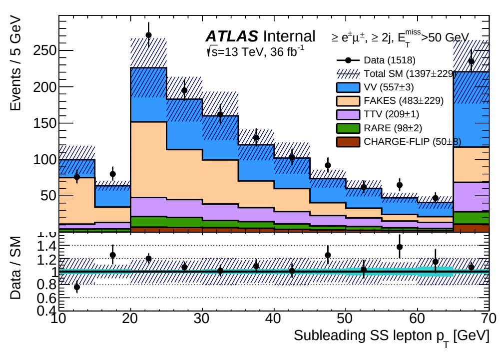

(e) Subleading SS lepton p_{T}

Figure B.2: Electron-muon channel: comparisons between observed data (2015+2016, 36 fb^{-1}) and expected SM+detector backgrounds for events with ≥ 2 same-sign leptons ($p_{\mathrm{T}} > 20$ GeV), $E_{\mathrm{T}}^{\mathrm{miss}} > 50$ GeV and ≥ 2 jets ($p_{\mathrm{T}} > 40$ GeV). Uncertainties include statistical sources, as well as systematic uncertainties for the data-driven backgrounds; for illustration, statistical uncertainties alone are shown in the light-coloured error bands in the ratio plots. Events belonging to any of the signal regions are rejected, both in data and MC.

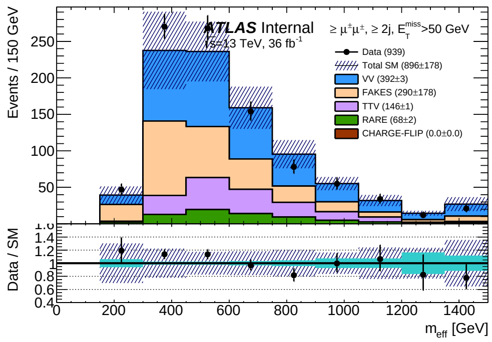

(a) Effective mass m_{eff}

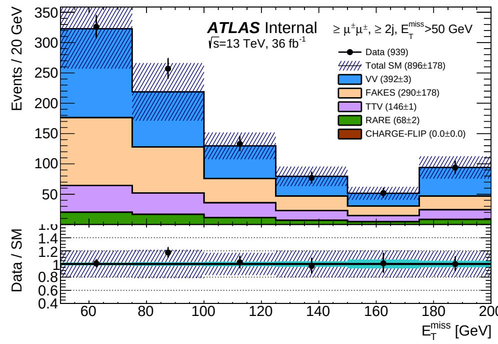

(b) Missing transverse momentum $E_{\mathrm{T}}^{\mathrm{miss}}$

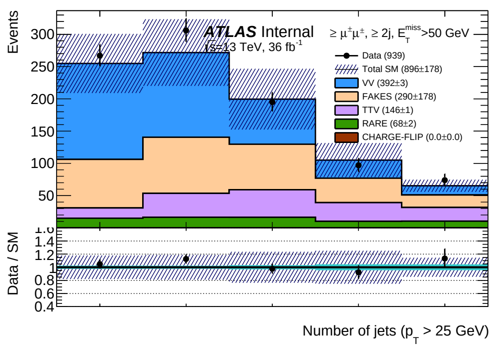

(c) Number of jets ($p_{\mathrm{T}} > 25$ GeV)

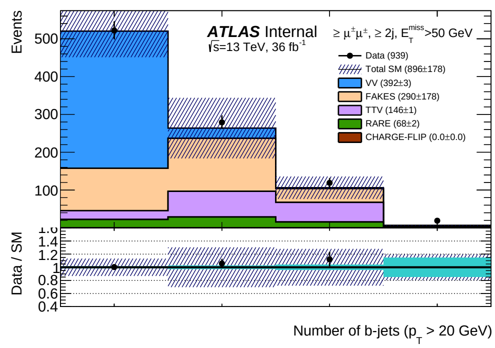

(d) Number of b-tagged jets ($p_{\mathrm{T}} > 20$ GeV)

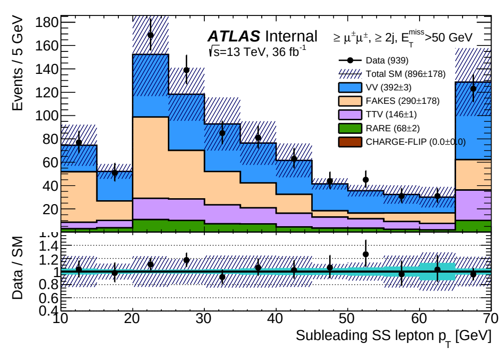

(e) Subleading SS lepton p_{T}

Figure B.3: Dimuon channel: comparisons between observed data (2015+2016, 36 fb^{-1}) and expected SM+detector backgrounds for events with ≥ 2 same-sign leptons ($p_{\mathrm{T}} > 20$ GeV), $E_{\mathrm{T}}^{\mathrm{miss}} > 50$ GeV and ≥ 2 jets ($p_{\mathrm{T}} > 40$ GeV). Uncertainties include statistical sources, as well as systematic uncertainties for the data-driven backgrounds; for illustration, statistical uncertainties alone are shown in the light-coloured error bands in the ratio plots. Events belonging to any of the signal regions are rejected, both in data and MC.

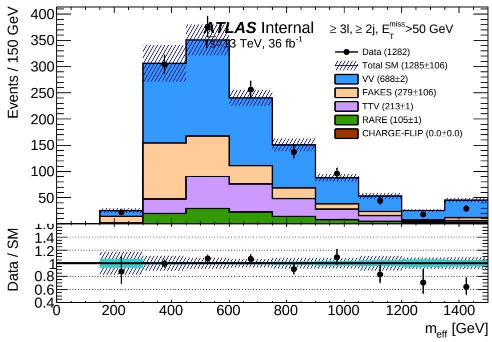

(a) Effective mass $m_{\rm eff}$

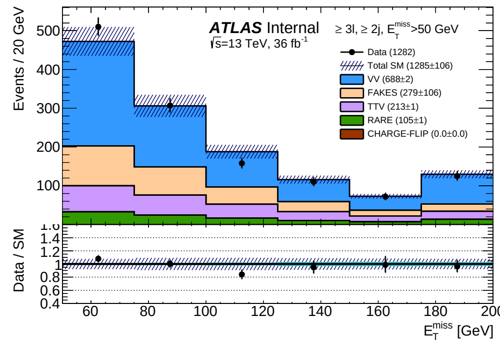

(b) Missing transverse momentum $E_{\rm T}^{\rm miss}$

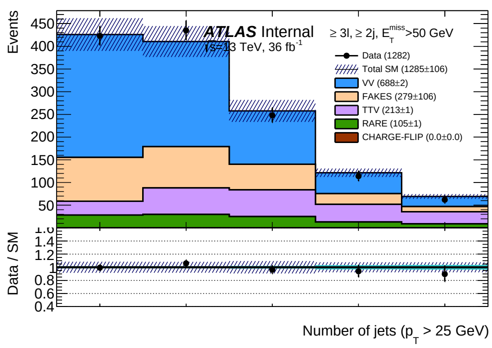

(c) Number of jets ($p_{\rm T} > 25$ GeV)

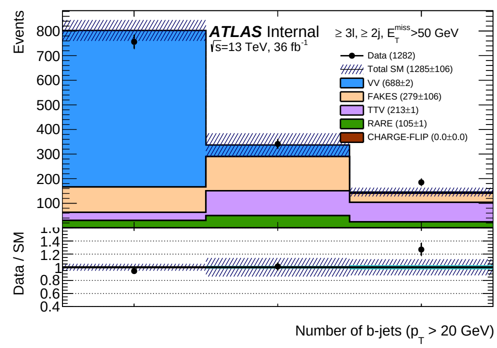

(d) Number of b-tagged jets ($p_{\rm T} > 20$ GeV)

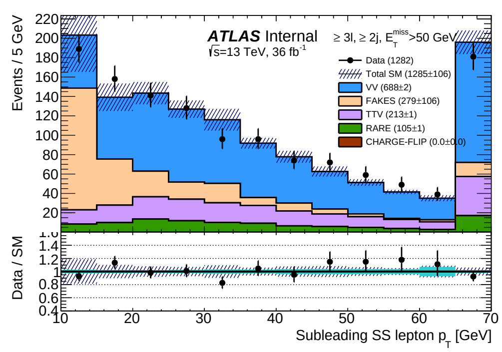

(e) Subleading SS lepton $p_{\rm T}$

Figure B.4: Trilepton channel: comparisons between observed data (2015+2016, 36 fb^{-1}) and expected SM+detector backgrounds for events with ≥ 3 leptons ($p_{\rm T} > 20$ GeV for the two leading leptons, $p_{\rm T} > 10$ GeV for the third lepton), $E_{\rm T}^{\rm miss} > 50$ GeV and ≥ 2 jets ($p_{\rm T} > 40$ GeV). Uncertainties include statistical sources, as well as systematic uncertainties for the data-driven backgrounds; for illustration, statistical uncertainties alone are shown in the light-coloured error bands in the ratio plots. Events belonging to any of the signal regions are rejected, both in data and MC.

References

[1] ATLAS Collaboration, JHEP **10** (2015) 054, arXiv:1507.05525 [hep-ex].

[2] ATLAS Collaboration, Eur. Phys. J. C **75** (2015) 510, arXiv:1506.08616 [hep-ex].

[3] ATLAS Collaboration, Atlas-conf-2015-066, https://cds.cern.ch/record/2114833.

[4] P. Huang, A. Ismail, I. Low, and C. E. M. Wagner, Phys. Rev. D **92** (2015) 075035, arXiv:1507.01601 [hep-ph].

[5] ATLAS Collaboration, Phys. Rev. **D88** (2013).

[6] H. Baer, V. Barger, P. Huang, D. Mickelson, A. Mustafayev, W. Sreethawong, and X. Tata, JHEP **12** (2013) 013, arXiv:1310.4858 [hep-ph], [Erratum: JHEP06,053(2015)].

[7] H. Baer, V. Barger, P. Huang, D. Mickelson, A. Mustafayev, W. Sreethawong, and X. Tata, Phys. Rev. Lett. **110** (2013) 151801, arXiv:1302.5816 [hep-ph].

[8] H. Baer, V. Barger, M. Savoy, and X. Tata, Phys. Rev. **D94** (2016) 035025, arXiv:1604.07438 [hep-ph].

[9] ATLAS Collaboration, ATLAS Collaboration, Eur. Phys. J. C **76** (2016) 653, arXiv:1608.03953 [hep-ex].

[10] D. J. Lange, Nucl. Instrum. Meth. A **462** (2001) 152.

[11] J. Alwall, R. Frederix, S. Frixione, V. Hirschi, F. Maltoni, O. Mattelaer, H. S. Shao, T. Stelzer, P. Torrielli, and M. Zaro, JHEP **07** (2014) 079, arXiv:1405.0301 [hep-ph].

[12] T. Sjöstrand, S. Mrenna, and P. Skands, Comput. Phys. Commun. **178** (2008) 852–867, arXiv:0710.3820 [hep-ph].

[13] R. D. Ball et al., Nucl. Phys. B **867** (2013) 244–289, arXiv:1207.1303 [hep-ph].

[14] ATLAS Collaboration, Atl-phys-pub-2014-021, https://cds.cern.ch/record/1966419.

[15] LHC Higgs Cross Section Working Group Collaboration, D. de Florian et al., arXiv:1610.07922 [hep-ph].

[16] T. Gleisberg et al., JHEP **02** (2009) 007, arXiv:0811.4622 [hep-ph].

[17] ATLAS Collaboration, Atl-phys-pub-2016-002, http://cds.cern.ch/record/2119986.

[18] H.-L. Lai et al., Phys. Rev. D **82** (2010) 074024, arXiv:1007.2241 [hep-ph].

[19] LHC Higgs Cross Section Working Group Collaboration, LHC Higgs Cross Section Working Group, arXiv:1201.3084 [hep-ph].

[20] ATLAS Collaboration, JHEP **2014** (2014) 55, arXiv:1406.3660 [hep-ex].

[21] M. Czakon and A. Mitov, Comput. Phys. Commun. **185** (2014) 2930, arXiv:1112.5675 [hep-ph].

[22] P. Skands, Phys. Rev. D **82** (2010) 074018, arXiv:1005.3457 [hep-ph].

[23] ATLAS Collaboration, G. Aad et al., Eur.Phys.J. **C70** (2010) 823–874, arXiv:1005.4568 [physics.ins-det].

[24] GEANT4 Collaboration, S. Agostinelli et al., Nucl. Instrum. Meth. A **506** (2003) 250–303.

[25] ATLAS Collaboration, ATL-PHYS-PUB-2010-013, http://cds.cern.ch/record/1300517.

[26] A. Sherstnev and R. Thorne, Eur. Phys. J. C **55** (2008) 553–575, arXiv:0711.2473 [hep-ph].

[27] ATLAS Collaboration, Atl-phys-pub-2016-005, http://cds.cern.ch/record/2120826.

[28] G. Corcella et al., JHEP **01** (2001) 010, arXiv:hep-ph/0011363.

[29] J. Pumplin et al., JHEP **07** (2002) 012, arXiv:hep-ph/0201195.

[30] J. Alwall, M. Herquet, F. Maltoni, O. Mattelaer, and T. Stelzer, JHEP **06** (2011) 128, arXiv:1106.0522 [hep-ph].

[31] LHC SUSY Cross Section Working Group, 2015, https://twiki.cern.ch/twiki/bin/view/LHCPhysics/SUSYCrossSections.

[32] S. Carrazza, S. Forte, and J. Rojo, *Parton distributions and event generators*, pp. , 89–96. 2013. arXiv:1311.5887 [hep-ph].

[33] L. Lönnblad and S. Prestel, JHEP **03** (2012) 019, arXiv:1109.4829 [hep-ph].

[34] C. Borschensky et al., Eur. Phys. J. C **74** (2014) 3174, arXiv:1407.5066 [hep-ph].

[35] ATLAS Collaboration, ATL-PHYS-PUB-2015-026, 2015, https://cds.cern.ch/record/2037717.

[36] M. Cacciari, G. P. Salam, and G. Soyez, JHEP **0804** (2008) 063, arXiv:0802.1189 [hep-ph].

[37] ATLAS Collaboration, arXiv:1603.02934 [hep-ex].

[38] M. Cacciari and G. P. Salam, Phys. Lett. B **659** (2008) 119–126, arXiv:0707.1378 [hep-ph].

[39] ATLAS Collaboration, ATLAS Collaboration, arXiv:1703.09665 [hep-ex].

[40] ATLAS Collaboration, Atlas-conf-2014-018, https://cds.cern.ch/record/1700870.

[41] ATLAS Collaboration, ATLAS Collaboration, JINST **11** (2016) P04008, arXiv:1512.01094 [hep-ex].

[42] ATLAS Collaboration, ATL-PHYS-PUB-2015-022, 2015, https://cds.cern.ch/record/2037697.

[43] ATLAS Collaboration, ATL-PHYS-PUB-2016-012, 2016, https://cds.cern.ch/record/2160731.

[44] ATLAS Collaboration, ATLAS-CONF-2016-024, 2016, https://cds.cern.ch/record/2157687.

[45] ATLAS Collaboration, ATLAS Collaboration, Eur. Phys. J. C **76** (2016) 292, arXiv:1603.05598 [hep-ex].

[46] ATLAS Collaboration, Eur. Phys. J. C **76** (2016) 666, arXiv:1606.01813 [hep-ex].

[47] ATLAS Collaboration, ATL-PHYS-PUB-2015-027, 2015, https://cds.cern.ch/record/2037904.

[48] ATLAS Collaboration, ATL-PHYS-PUB-2015-023, 2015, https://cds.cern.ch/record/2037700.

[49] R. D. Cousins, K. E. Hymes, and J. Tucker, Nucl.Instrum.Meth.Phys.Res. **A612** (2010) 388–398, arXiv:0905.3831 [physics.data-an].

[50] ATLAS Collaboration, ATLAS-CONF-2017-021, 2017, https://cds.cern.ch/record/2258143.

[51] ATLAS Collaboration, Atlas-conf-2016-037, http://cds.cern.ch/record/2205745.

[52] ATLAS Collaboration, Atlas-conf-2014-032, https://cds.cern.ch/record/1706245.

[53] G. Cowan, K. Cranmer, E. Gross, and O. Vitells, Eur. Phys. J. C **71** (2011) 1554, `arXiv:1007.1727 [physics.data-an]`, [Erratum: Eur. Phys. J. C **73** (2013) 2501].

[54] A. L. Read, Journal of Physics G: Nuclear and Particle Physics **28** (2002) 2693, `http://stacks.iop.org/0954-3899/28/i=10/a=313`.

[55] M. Baak et al., Eur. Phys. J. C **75** (2015) 153, `arXiv:1410.1280 [hep-ex]`.